Finite Element Based Circuit Models of Electrical Machines in Multi-Body-Dynamics

Zur Erlangung des akademischen Grades eines
Doktors der technischen Wissenschaften
ausgeführte Dissertation

eingereicht an der
Fakultät für Elektrotechnik
der Technischen Universität Graz

von

Martin Mohr

Begutachter: Univ.-Prof. Dr.-techn. Oszkár Bíró
Univ.-Prof. Dr.-Ing. habil. Dr. h. c. Kay Hameyer

Graz, 11. Dezember 2016

Abstract

This work deals with the application of models of electrical machines in a multi-body simulation environment. The coverage of harmonic effects caused by slotting or saturation, as well as a low calculation cost are the most important requirements for this application case.

Therefore, this work starts with a short summary of the most common machine model approaches. Further, a comparison of these models with respect to their application in multi-body dynamics simulations has been carried out. The finite element (FE-) based model approach has been identified as best suited for this field of application. This model approach uses characteristic curves created by FE simulations. Thus, this approach combines the model depth of FE models with a very low calculation effort.

For that reason, the FE-based model approach and several implementation issues are discussed in more detail. Further, the characteristic curve generation process using FE simulations has been investigated. This leads to an algorithm that decreases the simulation time of the preprocessing step by the way the simulation input data is permutated. In addition, the used interpolation method has been analyzed. From this study an effective algorithm for determining the interpolation parameters has been developed and implemented.

Next in this work, the FE-based model approach has been applied to several machine types. The resulting models and their implementation have been validated by comparisons with corresponding FE simulations.

Finally, the extension potential of the FE-based model approach is demonstrated. This is done by two extended models. The first model takes rotor skewing into account. This has been achieved by applying the multi-slice technique to the FE-based model approach. The second model takes rotor eccentricity into account. For that purpose an extended parameter space and the multi-slice technique are used.

Zusammenfassung

Diese Arbeit beschäftigt sich mit der Bereitstellung von Modellen elektrischer Maschinen in einer Mehrkörper-Dynamik Simulationsumgebung. Als Anforderungen an die verwendeten Modelle müssen hier vor allem die Berücksichtigung von Oberwelleneffekten sowie eine geringer Berechnungsaufwand angeführt werden.

Daher beginnt diese Arbeit mit der Vorstellung der bekanntesten Modellansätze und bewertet ihre Vor- bzw. Nachteile in Bezug auf die Anwendung in einer Mehrkörperdynamik-Simulationssoftware. Aus dieser Vorstudie ging der Finite-Elemente (FE-) basierte Modellansatz als für diese Anwendung am Besten geeignet hervor. Dieser Modelansatz basiert auf Kennlinien, welche durch Finite-Elemente Simulationen erzeugt werden. Daher kombiniert dieser Ansatz die Modeltiefe von FE Modellen mit einem sehr geringen Berechnungsaufwand.

Der FE-basierte Modelansatz und die verschiedene Varianten für dessen Umsetzung werden daher im Weiteren genauer beschrieben. Hierfür wurde unter anderem die Datengenerierung mittels FE Simulationen näher untersucht. Es entstand ein effizienter Algorithmus zur Permutation der Eingangsgrößen welcher die benötigte Simulationszeit für die Kennliniengenerierung reduziert. Des Weiteren wurde die Interpolationsmethode näher untersucht und ein sehr effizienter Algorithmus zur Berechnung der Interpolationsparametern aus der abgetasteten Kennlinie implementiert.

Anschließend werden für verschiedene Maschinentypen entsprechende FE-basierte Modelle präsentiert und im Detail beschrieben. Deren korrekte Funktionsweise bzw. Implementierung wurde durch entsprechende Simulationen verifiziert.

Zuletzt wird das Erweiterungspotential des FE-basierten Modellansatzes anhand von zwei Erweiterungen demonstriert. Hierbei handelt es sich zum Einem um die Berücksichtigung von Schrägung durch einen Multi-Slice Ansatz. Zum Anderen wird durch einen erweiterten Parameterraum Rotorexzentrizität berücksichtigt.

Acknowledgements

During the last few years I have worked on my PhD thesis I got help and support from many people, without them I would probably not have been able to finalize this work. Therefore, I would like to take this opportunity to thank all those people.

First of all I would like express a special word of thanks to my PhD supervisor Univ.-Prof. Dr.-techn. Oszkár Bíró. He found always the right words to guide me but left enough space that I could make my own experiences.

Furthermore, I would like to thank the Christian Doppler Research Association (CDG) for financially supporting this research.

I would also like to thank the AVL List GmbH for co-funding this work. In special I want to thank Dr. Franz Diwoky and Dr. Günter Ofner for the theoretical knowledge they have shared with me and for their technical support.

Moreover, I would like to thank the entire institute for fundamentals and theory in electrical engineering for the good working atmosphere. Especially, I thank Dr. Andrej Stermecki, Dr. Bernhard Weilharter and DI Paul Handgruber for their support.

Furthermore, I would like to thank the electric drive and machines institute, in special Dr. Klaus Krischan and Dr. Roland Seebacher for their support.

Last but not least I would like to thank my whole family, especially my mother Gerlinde and my wife Eva for their abundance of patience with myself. I also want to thank my children Manuel and Miriam for brighten me up whenever it was necessary.

CONTENTS

1 INTRODUCTION

1.1 Motivation

Simulation tools became the most important design tools for technical systems in the past. Nowadays, many simulation tasks are performed during the design stage. The used models cover the whole system or single components. Such simulation tasks are for example component dynamics (e.g. displacement-, deformation- or material stress analysis), electromagnetic analysis (e.g. field analysis, power loss calculation), noise and vibration harshness (NVH) investigations (low frequency vibration analysis, structure born noise investigations) or elastohydrodynamics (e.g. contact analysis, lubricant pressure and distribution analysis). These state of the art simulation tasks utilize simulation techniques as for instance finite element method (FEM), multibody dynamics (MBD), finite volume method (FVM) or computational fluid dynamics (CFD).

However, increasing system complexity and the need of more accurate simulations for optimization purposes lead to a continuous further development of these simulation techniques. This trend is enforced by the constantly increasing calculation power. Especially, the coupling of different physical domains is subject of ongoing research activities. This class of simulations is characterized by high complexity, strong nonlinearity, typical weak convergence behavior and high calculation cost. Therefore, multiphysics simulations are at the edge of available calculation power and allocatable memory.

The consideration of electrical machines in MBD simulations belongs to the family of multiphysical problems. Within this work a suitable model approach has been investigated and further developed.

1.1.1 Finite element models and multibody dynamics

The finite element method (FEM) subdivides the problem domain into many small fragments so called finite elements (FE). Each FE is described by a set of equations. These equations describe an approximate solution of the boundary value problem inside the finite element by considering continuity conditions at the FE boundary as well as excitation terms. Thus, the boundary value problem of the real world becomes discretized in space, see section 2.2. The coverage of effects (a.k.a. model depth) depends on the used physical equations. This very common approach can be applied to structural mechanical problems as well as to electromagnetic problems and many others. This simulation technique is well suited for determining integral quantities as for example flux or power loss. Furthermore, it provides a deep insight into the problem domain and allows investigations of local phenomena like stress or magnetic flux distributions. A lot of literature can be found about the

finite element method, e.g. [33], [81], [38].

Multibody dynamics on the other hand divides the problem domain into several bodies. They represent the mechanical components of the system. Each body can be rigid or flexible and is defined by several nodes. For each node a set of degrees of freedom (DOF) is defined representing the translational and rotational motion data of the node. The bodies, or more precisely their nodes, are coupled by connections. These connections are commonly called links or joints. They describe additional constraints for the DOFs of the involved nodes. Thus, this simulation technique is well suited for determining global motion as well as deformation of bodies. Due to the smaller number of DOFs per body, MBD allows simulation of more complex systems than FEM is able to. For determining the properties of the bodies, analytical methods or structural mechanic FEM can be used. Using FE models require a reduction of the DOFs that is done by mathematical methods (see [40]), for example static (Guyan) or dynamic condensation. These methods require linear material properties, a prerequisite that is typically fulfilled for many mechanical designs. However, these methods cannot be applied in case of nonlinear material properties, as for example in the presence of ferromagnetic materials. There is also extensive literature available about multi body dynamics, e.g. [93],[24],[85].

1.1.2 Model requirements

The requirements for an electrical machine model within an MBD simulation environment are difficult to define because they depend on the planned simulation task. However, from the mechanical point of view each electrical machine is some kind of link within the MBD model that couples nodes of the rotor body with nodes of the stator body. The mechanical input variables of this link are the speed and position of the rotor nodes with respect to the stator. The output variables are the forces and torques acting on the rotor and stator nodes.

During the pre-design stage simple force or torque sources representing an idealized model of the whole electrical power train might be sufficient. In contrast for shaft dynamics or NVH investigations, models of the electrical power train with a better coverage of harmonics effects are required. This includes electrical models for the machine as well as for the inverter, the power supply and the controller. Especially the controller mainly influences the behavior of the electrical powertrain and must not be ignored. Therefore, the link representing the electrical machine model needs additional electrical input and output quantities and has to be connected with an electrical circuit too. Furthermore, torque ripple, saturation and slotting effects of the back electro-motive force (EMF) need to be considered by the electrical machine model. Additionally, and in conflict with a large model depth, fast model evaluation is required.

1.2 Review of literature

This work deals with the combination of different model approaches and simulation techniques to achieve a fast multiphysical system simulation. For that purpose, a comprehensive study of model approaches and simulation techniques was necessary. The fundamentals of electrical machines build the basis of this study. Many good technical books can be found on this topic. Especially, the book trilogy of Germar Müller et al. [67], [69] and [68] as well as the reference book of Andreas Binder [7] can be regarded as standard literature for the German-speaking region (reference books in english are for example [90] and [17]). The basics of the fundamental wave model approach (FWMA) as well as of the Park transformation and Clarke transformation are described in detail in [68] and [7]. A further good introduction for the FWMA can be found e.g. in [90], [78]. Many publications dealing with fundamental wave models can be found in literature, within this work [18], [95] and [6] should be explicitly mentioned. These papers deal with the parameter determination using FEM simulations as described in subsection 3.5.7. However, the FWMA considers only the fundamental wave of the magneto motive force (MMF). Saturation is also only considered by its effect to the fundamental wave. Any harmonic effects caused by slotting, cogging torque and saturation are neglected. The FWMA can be regarded as a simplified variant of the more general field harmonic approach (FHA).

The FHA considers the effects of slotting by using analytical functions for describing the electric loading and permeance of the air gap in circumferential direction. A very detailed description of this approach is given by Seinsch [84]. Here a detailed derivation of the corresponding Fourier series, the interplay of the resulting spatial waves in the air gap and the effect to the machine behavior (radial forces, losses and noise) can be found. Furthermore, the work of Oberretl [70], [71], [72], [73] and that of Lach [42] should be mentioned. In these works the effect of harmonics to power loss and noise generation are investigated. In addition, the papers of Zhu et al. [100], [97], [98] and [99] for permanent magnet synchronous machines should be mentioned because the FHA is also well suited for cogging torque minimization and magnet shape optimization in permanent magnet machines as demonstrated e.g. in [96], [101].

The winding function approach (WHA) represents a very similar approach to the FHA. The FHA describes the magnetic field in the air gap whereas the WFA describes the coupling of windings by winding functions. Fudeh [21], [22], [23] has presented this coupled-circuit approach in the early eigthies. Moreira et al. in [66] present a WFA model for saturated induction machines and Luo et al. in [46] use this approach for detecting asymmetries in squirrel cage induction machines. The WFA has been further used for instance for torque optimization [34] or for the calculation of harmonic emission [28]. Furthermore, the modified WFA allows the consideration of eccentricity effects by a modulated air gap, as shown e.g. in [2], [35] and [31].

The magnetic equivalent circuit (MEC) approach for modelling electrical machines is also an old approach. Carpenter [11] described this technique already in 1968. This was before FEM was developed and sufficient calculation power was available. Twenty years

later Ostović presented a model for a squirrel cage induction machine [74]. Further he wrote a very detailed reference book [75]. Already within this work, he presented models for taking skewing and eccentricity into account. Later he also applied the MEC approach to claw-pole generators [76], a pure 3D problem caused by the claw-pole construction. Nowadays, this approach is still in the focus of interest as an alternative to 3D FEM simulations, e.g. [47], [87], [15], [90]. The MEC approach can be also used for calculating eddy currents as shown in [12], [14]. Furthermore, iron and magnet losses [88] or eccentricity [37], [94] can be modelled using MECs.

The FE-based model approach uses FE simulations for creating characteristic curves. Mohammed et al. did extensive work on this topic and presented various physical variable models for electrical machines [50], [49], [58], [52], [82] and transformers [59]. They presented several improvements [53], [44], considered iron losses [54] or winding faults [56]. Furthermore, they used these models in several applications [51], [57], [55], for optimization tasks [83] or extended it for high frequency capabilities [48]. However, there are also other researches working on this topic, e.g. [19], [36], [80].

1.3 Contribution of this work to science

The FE-based model approach has been analyzed and all implementation issues have been discussed in this work. Based on this study an extendable implementation for this model approach has been worked out. This includes, on the one hand, the implementation of the model itself and on the other hand the work flow that is necessary for using such models. The workflow consists of three issues: the required FEM simulations, the interpolation parameter preprocessing and the transient MBD simulation.

The scientific contributions of this work have been published by the author in [60]-[65]. These publications are briefly reviewed below.

The most important requirement for the workflow is simplicity. This is achieved by using only state of the art simulation techniques and FEM post processing techniques. In this context an improved algorithm for the variation of the input parameters for the FEM simulations has been presented in [64]. Due to the fact that the memory demand and the calculation effort for determining interpolation parameters for multi-dimensional look-up tables increases exponentially with the number of dimensions, an efficient algorithm for determining multi-dimensional cubic spline parameters has been also presented in [64].

The developed FE-based model of a permanent magnet synchronous machine (PMSM) has been presented in [61]. This model differs from already presented models by the choice of the quantities that are applied to the model by characteristic curves as well as by the used interpolation method. These changes make the model easier to use and simplify the FEM preprocessing. In [62] a FE-based model for a wound rotor induction machine has been presented.

The extension potential of the FE-based model approach has been shown in [65]. In this work skewing has been taken into account by applying the multi-slice technique for 2D FEM simulations to the FE-based model approach. Due to the chosen parameter values for the characteristic curves this extension is very easy to implement and the additional calculation effort is very low.

Finally, an extended FE-based model for a PMSM for taking rotor eccentricity into account has been presented in [63]. This was achieved by adding two additional parameter values for the characteristic curves. This expands the parameter space of the model and enables the consideration of a rotor displacement. Furthermore, two additional look-up tables have been added for taking the magnetic drag caused by rotor displacement into account. In combination with the multi-slice technique any kind of rotor eccentricity as well as rotor bending could be approximated. The validation of this model has been presented in [60].

1.4 Outline of this work

In chapter 1 the motivation for the work and the location of the work within the field of simulation techniques is presented. Furthermore, a review of literature shows the current state of simulation techniques and gives an overview of already developed machine models.

Chapter 2 goes more in detail and presents all mathematical and technical fundamentals used in this work. This includes further the theoretical background for the relevant simulation methods. A brief introduction of several machine model approaches is carried out in chapter 3. A concluding comparison is done for finding the model approach that best fits the needed requirements.

In chapter 4 the finite element based circuit model approach is explained in more detail. All improvements of this model approach that have been carried out by this work are presented there. This includes the FE modeling process, algorithms developed for the parameter determination and data pre-processing as well as some implementation details. The used assumptions and consequential limitations are discussed. An explanation of the validation workflow concludes this chapter.

The next chapter 5 presents the implementation and validation of various electrical machine models. This includes detailed derivations for each machine model type, a description of the used FE-machine model and several comparisons for errors, calculation times and memory demand between the new models and the according transient reference FE-model simulation.

In chapter 6 the extension potential of the FE-based model approach is shown. This includes the consideration of skewing and an approximation for dynamic rotor eccentricity for permanent magnet synchronous machines.

The final chapter 7 concludes the work and shows open issues for further research and development activities.

2 FUNDAMENTALS

2.1 Electromagnetic fundamentals

From the physical point of view almost all electromagnetic effects are described by Maxwell's equations presented in subsection 2.1.2. However, these equations cannot be solved analytically for general problems and are not suited very well for solving engineering tasks fast. Therefore, the circuit theory, a more practical approach, is widely used for engineering purposes.

2.1.1 Circuit theory for lumped elements

In this subsection the circuit theory for lumped elements is summarized. This includes Kirchhoff's laws for describing the network as well as the equations for the lumped elements including Ohm's law. Furthermore, all lumped elements used in this work for modeling electrical machines are described.

Methods and tools used for solving such electric network problems, such as nodal analysis and *Berkeley SPICE* are not in the focus of this work but can be found in literature, e.g. [89].

Lumped circuits consist of lumped elements and ideal wires. The ideal wires are just used to define the element interconnection and can be assumed as stretched nodes. Thus, they have no representation in real world and any energy conversion occurs only within the lumped elements. These lumped elements like resistors, inductances or voltage sources describe the whole electromagnetic behavior of the circuit. This means that no external phenomena or parasitic effects exist. For all lumped elements and thus for the whole lumped circuit a negligible physical dimension is assumed [1]. Under these assumptions both Kirchhoff's laws [16] are valid:

Kirchhoff's current law (K1). *For any lumped electric circuit, for any of its nodes, and for any time, the algebraic sum of all branch currents leaving the node is zero.*

Kirchhoff's voltage law (K2). *For any lumped electric circuit, for any of its loops, and for any time, the algebraic sum of the branch voltages around the loop is zero.*

For modeling electrical machines, only a small set of circuit elements is necessary. These are, on the one hand, the passive elements resistor, inductor and mutual inductor. Furthermore, voltage source elements are used for modeling power supplies or voltages induced due to motion.

A simple example of such an electric circuit is shown in Fig. 2.1 with the voltage source S_1, the resistors R_1, R_2 and the inductance L_1.

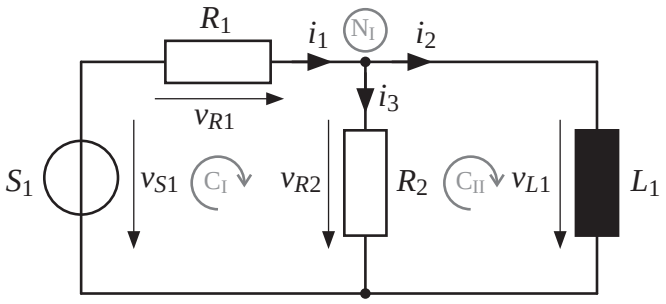

Figure 2.1: Example of a simple circuit with lumped elements. The voltage source S_1 and the resistors R_1 and R_2 build the voltage loop C_I, the inductor L_1 and R_2 build C_{II}. In the node N_I the current i_1 is divided into i_2 and i_3. The corresponding equations are shown in (2.1) to (2.3).

The equations for the loops C_I, C_{II} and the node N_I are

$$C_I: \quad -v_{S1} + v_{R1} + v_{R2} = 0 \tag{2.1}$$

$$C_{II}: \quad -v_{R2} + v_{L1} = 0 \tag{2.2}$$

$$N_I: \quad -i_1 + i_2 + i_3 = 0 \tag{2.3}$$

The resistor represents the conversion of electrical energy to thermal energy. For electrical machines, this is the power loss in the copper and iron. For transient processes the resistor acts as a damping element. Ohm's law (2.4) describes the relationship between the voltage drop v over the resistor, the current i flowing through the resistor and the resistance R of the resistor:

$$v = i \cdot R \qquad \text{(Ohm's law)}. \tag{2.4}$$

Using (2.4), the instantaneous electrical power p can be written as

$$p = v \cdot i = i^2 \cdot R = \frac{v^2}{R}. \tag{2.5}$$

The inductor element represents the self-inductance L of a coil. This is the ratio between the magnetic flux linkage Ψ linked with the coil and the current i in the coil

$$L = \frac{\Psi}{i} = N\frac{\Phi}{i}, \tag{2.6}$$

with the magnetic flux Φ and the number of windings N for the case that all windings are linked with the same magnetic flux. The inductance takes the geometric dimensions of the coil, the number of windings and the material properties into account. For linear materials the magnetic flux is proportional to the current, leading to a constant inductance. However, for coils that are made of ferromagnetic materials saturation occurs. This is caused by the

nonlinear permeability of such materials. Hence, the inductance is a nonlinear function of the current in general:

$$L = f(i). \tag{2.7}$$

The element equation for an inductor in time domain is defined by Faraday's law

$$v = \frac{d\psi}{dt} = \frac{d}{dt}(L \cdot i) = L\frac{di}{dt} \quad \text{for constant } L, \tag{2.8}$$

and can be rewritten for time harmonic signals as

$$\underline{V} = j2\pi f L \cdot \underline{I} = j\omega L \cdot \underline{I} = jX_L \cdot \underline{I}, \tag{2.9}$$

with the imaginary unit j, the frequency f , the angular frequency ω, the inductive reactance X_L and the phasors for the voltage $\underline{V}$ and the current $\underline{I}$.

Using (2.7) and (2.8), the instantaneous power for inductances can be written as

$$p = v \cdot i = \frac{d}{dt}(L \cdot i) \cdot i = \frac{dL}{dt} \cdot i^2 + L \cdot \frac{di}{dt} \cdot i = L \cdot \frac{di}{dt} \cdot i \Big|_{L=\text{constant}}. \tag{2.10}$$

The mutual inductor element represents the mutual inductance M between two coils and describes the magnetic coupling between them. It is defined as

$$M = M_{12} = \frac{\Psi_{12}}{i_2} \stackrel{!}{=} M_{21} = \frac{\Psi_{21}}{i_1}. \tag{2.11}$$

The equivalence between M_{12} and M_{21} is due to the reciprocity theorem [29]. The voltage equations for two coupled coils as shown in Fig.2.2 can be written as

$$v_1 = \frac{d\Psi_1}{dt} = \frac{d}{dt}(L_1 \cdot i_1 + M \cdot i_2) = L_1\frac{di_1}{dt} + M\frac{di_2}{dt}\Big|_{L_1, M=\text{constant}}, \tag{2.12}$$

$$v_2 = \frac{d\Psi_2}{dt} = \frac{d}{dt}(L_2 \cdot i_2 + M \cdot i_1) = L_2\frac{di_2}{dt} + M\frac{di_1}{dt}\Big|_{L_2, M=\text{constant}}. \tag{2.13}$$

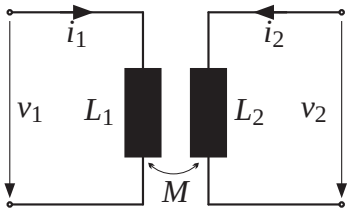

Figure 2.2: Two coupled coils

The total instantaneous power for constant inductances has the form

$$p = v_1 \cdot i_1 + v_2 \cdot i_2 = L_1\frac{di_1}{dt}i_1 + M\frac{di_2}{dt}i_1 + L_2\frac{di_2}{dt}i_2 + M\frac{di_1}{dt}i_2. \tag{2.14}$$

For non-linear materials all inductances L_1, L_2 and M_{12} depend on all coils currents:

$$L_1 = f(i_1, i_2), \; L_2 = f(i_1, i_2), \; M = f(i_1, i_2). \tag{2.15}$$

In electrical machines an electro-mechanical energy conversion takes place. This requires induced voltages due to motion and thus rotor position dependent inductances as presented in subsection 2.4.2. However, within the theory of lumped elements, inductances are only energy storage elements. Thus any energy conversation must be modeled with additional controlled voltage sources or resistances.

2.1.2 Electromagnetic field equations

The electromagnetic field equations, also called Maxwell's equations, describe the electromagnetic phenomena by field quantities. These equations [39] are written as

$$\nabla \times \mathbf{H} = \mathbf{J} + \frac{\partial \mathbf{D}}{\partial t} \qquad \text{(Ampére's law)}, \tag{2.16}$$

$$\nabla \times \mathbf{E} = -\frac{\partial \mathbf{B}}{\partial t} \qquad \text{(Faraday's law)}, \tag{2.17}$$

$$\nabla \cdot \mathbf{B} = 0 \qquad \text{(Gauss' law for magnetism)}, \tag{2.18}$$

$$\nabla \cdot \mathbf{D} = \rho_V \qquad \text{(Gauss' law)}, \tag{2.19}$$

with the Nabla operator ∇, the magnetic field intensity vector $\mathbf{H}$, the current density vector $\mathbf{J}$, the electric flux density vector $\mathbf{D}$, the electric field intensity vector $\mathbf{E}$, the magnetic flux density vector $\mathbf{B}$ and the electric volume charge density ρ_V. Ampére's law implies furthermore the principle of charge conversation [39]:

$$\nabla \cdot (\nabla \times \mathbf{H}) \equiv 0 = \nabla \cdot \left(\mathbf{J} + \frac{\partial \mathbf{D}}{\partial t} \right) = \nabla \cdot \mathbf{J} + \frac{\partial \rho_V}{\partial t}. \tag{2.20}$$

This set of differential equations describes the sources and whirls of the electromagnetic field quantities. These field quantities are defined uniquely from a mathematical point of view provided suitable boundary conditions are also specified. However, for a physical interpretation of these relations an integral form is better suited. The transformation utilizes the Gauss' theorem (2.21) and the Stokes' theorem (2.22).

Gauss' theorem [39] describes the equivalence of a volume integral for the divergence of a vector field $\mathbf{X}$ over a volume V and the surface integral of $\mathbf{X}$ over the volume's surface ∂V:

$$\iiint_V \nabla \cdot \mathbf{X} \, dV = \oiint_{\partial V} \mathbf{X} \cdot d\mathbf{s}. \tag{2.21}$$

From a physical point of view, the volume integral accumulates all sources within the volume and the surface integral determines the flux flowing through the volume surface.

Stokes' theorem [39] represents the equivalence of a surface integral for the curl of a vector field $\mathbf{X}$ over a surface $\mathbf{S}$ and the closed line integral of $\mathbf{X}$ over the surface's boundary $\partial\mathbf{S}$:

$$\iint_{\mathbf{S}} (\nabla \times \mathbf{X}) \cdot d\mathbf{s} = \oint_{\partial\mathbf{S}} \mathbf{X} \cdot d\mathbf{l}. \tag{2.22}$$

Using (2.21) and (2.22), Maxwell's equations can be rewritten in their integral form [39] as

$$\oint_{\partial\mathbf{S}} \mathbf{H} \cdot d\mathbf{l} = \iint_{\mathbf{S}} \left(\mathbf{J} + \frac{\partial \mathbf{D}}{\partial t} \right) \cdot d\mathbf{s} \qquad \text{(Ampére's law)}, \tag{2.23}$$

$$\oint_{\partial\mathbf{S}} \mathbf{E} \cdot d\mathbf{l} = -\iint_{\mathbf{S}} \frac{\partial \mathbf{B}}{\partial t} \cdot d\mathbf{s} \qquad \text{(Faraday's law)}, \tag{2.24}$$

$$\oiint_{\partial V} \mathbf{B} \cdot d\mathbf{s} = 0 \qquad \text{(Gauss' law for magnetism)}, \tag{2.25}$$

$$\oiint_{\partial V} \mathbf{D} \cdot d\mathbf{s} = \iiint_{V} \rho_V \, dV = Q \qquad \text{(Gauss' law)}, \tag{2.26}$$

with the total volume charge Q.

Additionally to Maxwell's equations, three tensorial equations are used to describe the influence of material, as shown in [32]. These are

$$\mathbf{B} = \overline{\mu}\,\mathbf{H},\ \mathbf{D} = \overline{\varepsilon}\,\mathbf{E} \ \text{ and } \mathbf{J} = \overline{\sigma}\,\mathbf{E}, \tag{2.27}$$

with the magnetic permeability tensor $\overline{\mu}$, the electric permittivity tensor $\overline{\varepsilon}$ and the electric conductivity tensor $\overline{\sigma}$. All material tensors are not constant in general. They vary with the position in space, the temperature, the frequency or the field quantities. For isotropic materials these tensors become scalars leading to

$$\mathbf{B} = \mu\mathbf{H} = \mu_0\mu_r\mathbf{H}, \tag{2.28}$$

$$\mathbf{D} = \varepsilon\mathbf{E} = \varepsilon_0\varepsilon_r\mathbf{E}, \tag{2.29}$$

$$\mathbf{J} = \sigma\mathbf{E}, \tag{2.30}$$

with the relative permeability μ_r and the permeability of free space $\mu_0 = 4\pi \times 10^{-7}\,\mathrm{H/m}$, the relative permittivity ε_r and the permittivity of free space $\varepsilon_0 \cong 8.8541 \times 10^{-12}\,\mathrm{F/m}$. For ferromagnetic materials, saturation needs to be considered. This implies the decrease of the relative permeability at higher field strengths. Saturation is a nonlinear effect and is typically considered in electromagnetic simulations by characteristic B-H curves.

For electrical machines, Maxwell's equations can be simplified. There are no free volume charges ρ_V present, thus Gauss' law (2.19) becomes a homogeneous equation. Furthermore, any wave propagation effects can be neglected due to the different scales of the material parameters σ and $\omega\varepsilon$ in the conducting domain and the small geometric machine dimensions compared with the wave length in the non-conducting domain. Writing Ampére's law (2.16) for the conducting domain under consideration of the material equations

(2.29) and (2.30) in time harmonic notation leads to

$$\nabla \times \mathbf{H} = \mathbf{J} + j\omega\mathbf{D} = \sigma\mathbf{E} + j\omega\varepsilon\mathbf{E} = \hat{\sigma}\mathbf{E}, \tag{2.31}$$

$$\hat{\sigma} := \sigma + j\omega\varepsilon, \tag{2.32}$$

with the complex conductivity $\hat{\sigma}$. The conducting materials used in electrical machines are copper and aluminum for the electrical conductors and iron or steel for the magnetic flux conducting parts and the complementary construction parts. In every case, a conductivity of $\sigma > 10^6\,\mathrm{S/m}$ can be assumed for those materials. In the conducting domain the permittivity is in the scale of ε_0. Thus, the real part of the conductivity is dominant and the permittivity can be neglected within conductors. In the non-conducting domain a relative permittivity of $\varepsilon_r < 10$ and a relative permeability of $\mu_r \approx 1$ can be assumed. This leads to a wave length λ of

$$\lambda = \frac{c}{f} = \frac{1}{\sqrt{\mu\varepsilon}\cdot f} = \frac{1}{\sqrt{\mu_r\varepsilon_r\mu_0\varepsilon_0}\cdot f} = \frac{c_0}{\sqrt{\mu_r\varepsilon_r}\cdot f} \tag{2.33}$$

with the speed of electromagnetic waves in materials c and in the vacuum c_0. For typical frequencies that appear in electrical machines the wave length is much larger than the geometric dimensions and thus the influence of $\mathbf{D}$ can be neglected. Hence Gauss' law can also be disregarded. This leads finally to the quasi-static Maxwell equations

$$\nabla \times \mathbf{H} = \mathbf{J}, \tag{2.34}$$

$$\nabla \times \mathbf{E} = -\frac{\partial \mathbf{B}}{\partial t}, \tag{2.35}$$

$$\nabla \cdot \mathbf{B} = 0, \tag{2.36}$$

$$\tag{2.37}$$

including the solenoidality of $\mathbf{J}$

$$\nabla \cdot \mathbf{J} = 0, \tag{2.38}$$

derived from equation (2.34). The quasi-static Maxwell equations describe all effects of magnetic induction including skin effect and eddy currents in conductors but neglect any capacitive effects.

2.1.3 Electromagnetic forces

Electromagnetic forces are body forces. They act throughout the whole volume of a body. The Lorentz force law, the Maxwell stress tensor or the virtual displacement can be used to calculate them. In this subsection, a short summary of these methods is presented.

The Lorentz force law

In physical experiments electrostatic forces on charged particles and electromagnetic forces on moving charged particles can be observed. These forces are combined by the Lorentz force law. The force **F** acting on a charged particle with the charge q is

$$\mathbf{F} = q\left(\mathbf{E} + \mathbf{v} \times \mathbf{B}\right), \tag{2.39}$$

with the particle velocity **v**. The force density **f** of a body with distributed charges can be derived from (2.39) as

$$\mathbf{f} = \rho_V \left(\mathbf{E} + \mathbf{v} \times \mathbf{B}\right) = \rho_V \mathbf{E} + \mathbf{J} \times \mathbf{B}, \tag{2.40}$$

with the charge velocity **v** in every point of space and the relationship $\mathbf{J} = \rho_V \mathbf{v}$. The total body force acting on an object can be determined by a volume integral of **f** over the object's volume

$$\mathbf{F} = \iiint_V \mathbf{f} dV. \tag{2.41}$$

Neglecting the electrostatic force, the force on a straight current-carrying conductor filament of length vector **l** in a homogeneous magnetic field **B** can be written as

$$\mathbf{F} = i\left(\mathbf{l} \times \mathbf{B}\right), \tag{2.42}$$

with the charge velocity in (2.40) defined in a reference system of the conductor.

The Maxwell stress tensor

In continuum mechanics a force density can be written as the divergence of a second order stress tensor field. This approach leads to the Maxwell stress tensor $\overline{\mathbf{T}}$ and

$$\mathbf{f} = \operatorname{div} \overline{\mathbf{T}} - \varepsilon_0 \mu_0 \frac{\partial \mathbf{S}}{\partial t}, \tag{2.43}$$

with the Poynting vector **S**, representing the electromagnetic power flux. The Maxwell stress tensor in vacuum can be derived from (2.40) using Ampére's law (2.16) and Gauss's law (2.19)

$$\begin{aligned} \mathbf{f} &= (\nabla \cdot \mathbf{D})\,\mathbf{E} + \left(\nabla \times \mathbf{H} - \frac{\partial \mathbf{D}}{\partial t}\right) \times \mathbf{B} \\ &= \varepsilon_0 (\nabla \cdot \mathbf{E})\,\mathbf{E} + \frac{1}{\mu_0} (\nabla \times \mathbf{B}) \times \mathbf{B} - \varepsilon_0 \frac{\partial \mathbf{E}}{\partial t} \times \mathbf{B}. \end{aligned} \tag{2.44}$$

This equation can be rewritten as

$$\begin{aligned} \mathbf{f} =& \varepsilon_0 \left((\nabla \cdot \mathbf{E})\,\mathbf{E} - \mathbf{E} \times (\nabla \times \mathbf{E})\right) \\ &+ \frac{1}{\mu_0} \left((\nabla \cdot \mathbf{B})\,\mathbf{B} - \mathbf{B} \times (\nabla \times \mathbf{B})\right) \\ &- \varepsilon_0 \frac{\partial}{\partial t} \left(\mathbf{E} \times \mathbf{B}\right), \end{aligned} \tag{2.45}$$

using

$$\frac{\partial \mathbf{E}}{\partial t} \times \mathbf{B} = \frac{\partial}{\partial t}(\mathbf{E} \times \mathbf{B}) - \mathbf{E} \times \frac{\partial \mathbf{B}}{\partial t}, \tag{2.46}$$

and Faraday's law (2.17) as well as Gauss' law for magnetism (2.18). Finally, the force density can be written as

$$\begin{aligned} \mathbf{f} =& \varepsilon_0 \left[(\nabla \cdot \mathbf{E}) \mathbf{E} + (\mathbf{E} \cdot \nabla) \mathbf{E} \right] + \frac{1}{\mu_0} \left[(\nabla \cdot \mathbf{B}) \mathbf{B} + (\mathbf{B} \cdot \nabla) \mathbf{B} \right] \\ & - \frac{\varepsilon_0}{2} \nabla (\mathbf{E} \cdot \mathbf{E}) - \frac{1}{2\mu_0} \nabla (\mathbf{B} \cdot \mathbf{B}) - \underbrace{\varepsilon_0 \frac{\partial}{\partial t} (\mathbf{E} \times \mathbf{B})}_{= \varepsilon_0 \mu_0 \frac{\partial \mathbf{S}}{\partial t}}, \end{aligned} \tag{2.47}$$

using the vector calculus identity [29]

$$\mathbf{X} \times (\nabla \times \mathbf{X}) = \frac{1}{2} \nabla (\mathbf{X} \cdot \mathbf{X}) - (\mathbf{X} \cdot \nabla) \mathbf{X} \tag{2.48}$$

for $\mathbf{E}$ and $\mathbf{B}$ to eliminate the curls in (2.45). The first four terms on the right side of (2.47) are equal to the divergence of the Maxwell stress tensor while the last term describes the force density due to radiation as shown in (2.43). Indeed, writing the x-component of the force density and neglecting the radiation term (which can be done at low frequencies) leads to:

$$\begin{aligned} f_x =& \varepsilon_0 \left[\frac{\partial E_x}{\partial x} E_x + \frac{\partial E_y}{\partial y} E_x + \frac{\partial E_z}{\partial z} E_x + E_x \frac{\partial E_x}{\partial x} + E_y \frac{\partial E_x}{\partial y} + E_z \frac{\partial E_x}{\partial z} \right] + \\ & \frac{1}{\mu_0} \left[\frac{\partial B_x}{\partial x} B_x + \frac{\partial B_y}{\partial y} B_x + \frac{\partial B_z}{\partial z} B_x + B_x \frac{\partial B_x}{\partial x} + B_y \frac{\partial B_x}{\partial y} + B_z \frac{\partial B_x}{\partial z} \right] - \\ & \varepsilon_0 \left(E_x \frac{\partial E_x}{\partial x} + E_y \frac{\partial E_y}{\partial x} + E_z \frac{\partial E_z}{\partial x} \right) - \frac{1}{\mu_0} \left(B_x \frac{\partial B_x}{\partial x} + B_y \frac{\partial B_y}{\partial x} + B_z \frac{\partial B_z}{\partial x} \right). \end{aligned} \tag{2.49}$$

The divergence of a second order tensor field $\overline{\mathbf{T}}$ is defined as

$$\operatorname{div} \overline{\mathbf{T}} = \sum_{i=1}^{3} \sum_{j=1}^{3} \frac{\partial T_{ij}}{\partial x_j} \mathbf{e}_i = \sum_{i=1}^{3} \left(\frac{\partial T_{i1}}{\partial x_1} + \frac{\partial T_{i2}}{\partial x_2} + \frac{\partial T_{i3}}{\partial x_3} \right) \mathbf{e}_i, \tag{2.50}$$

with the basis vectors $\mathbf{e}_i$. For $\mathbf{e}_1 = \mathbf{e}_x$ the tensor elements T_{11}, T_{12} and T_{13} are used for calculating the x-component of $\mathbf{f}$. These tensor elements can be found by a comparison of (2.49) and (2.50) for $i = 1$. For example, all terms with a partial derivative with respect to x in (2.49) corresponds to the term $\frac{\partial T_{11}}{\partial x_1}$ in (2.50):

$$\begin{aligned} \frac{\partial T_{11}}{\partial x_1} =& \varepsilon_0 \left(\frac{\partial E_x}{\partial x} E_x + E_x \frac{\partial E_x}{\partial x} \right) + \frac{1}{\mu_0} \left(\frac{\partial B_x}{\partial x} B_x + B_x \frac{\partial B_x}{\partial x} \right) - \\ & \varepsilon_0 \left(E_x \frac{\partial E_x}{\partial x} + E_y \frac{\partial E_y}{\partial x} + E_z \frac{\partial E_z}{\partial x} \right) - \frac{1}{\mu_0} \left(B_x \frac{\partial B_x}{\partial x} + B_y \frac{\partial B_y}{\partial x} + B_z \frac{\partial B_z}{\partial x} \right). \end{aligned} \tag{2.51}$$

This leads finally for T_{11} to

$$T_{11} = \varepsilon_0 \left(E_1 E_1 - \frac{1}{2} (\mathbf{E} \cdot \mathbf{E}) \right) + \frac{1}{\mu_0} \left(B_1 B_1 - \frac{1}{2} (\mathbf{B} \cdot \mathbf{B}) \right). \tag{2.52}$$

The identification of T_{12} and T_{13} can be done in a similar manner. Furthermore, all remaining tensor elements can be found using f_y, the y-component of the force density and its z-component f_z. This leads finally to the definition of the Maxwell stress tensor

$$T_{ij} = \varepsilon_0 \left(E_i E_j - \frac{1}{2} (\mathbf{E} \cdot \mathbf{E}) \, \delta_{ij} \right) + \frac{1}{\mu_0} \left(B_i B_j - \frac{1}{2} (\mathbf{B} \cdot \mathbf{B}) \, \delta_{ij} \right), \tag{2.53}$$

with the Kronecker symbol δ_{ij} defined as

$$\delta_{ij} = \begin{cases} 1 & \text{if } i = j, \\ 0 & \text{otherwise.} \end{cases} \tag{2.54}$$

The resulting electromagnetic force $\mathbf{F}$ acting on an object can be determined as

$$\mathbf{F} = \iiint_V \operatorname{div} \overline{\mathbf{T}} dV = \oiint_{\partial V} \overline{\mathbf{T}} \cdot d\mathbf{s}, \tag{2.55}$$

using the Maxwell stress tensor and the tensorial Gauss' theorem (2.21). The advantage of the Maxwell stress tensor is that it needs to be evaluated only at the objects surface. Furthermore, for an object in free space (or air) any surface that envelops the object can be used. For example, the air gap of an electrical machine is a suitable surface to determine the force acting on the rotor. Therefore, the assumption of vacuum (or air) during the derivation of the Maxwell stress tensor is no restriction to its application. In quasi-static case, as assumed for electrical machines, the Maxwell stress tensor can be simplified [68]. All terms including the electric field intensity $\mathbf{E}$ can be neglected and the Maxwell stress tensor can be rewritten as

$$T_{ij} = \frac{1}{\mu_0} \left(B_i B_j - \frac{1}{2} (\mathbf{B} \cdot \mathbf{B}) \, \delta_{ij} \right). \tag{2.56}$$

Method of virtual displacement

The third method commonly used to determine electromagnetic forces is the method of virtual displacement (or virtual work principle). This method is based on the conservation of energy in isolated systems [29]. Let us assume an electromagnetic system consisting of N coils, the corresponding power supplies for these coils and ferromagnetic components. Furthermore, no power dissipation due to resistive or hysteresis losses shall occur. This means that, for constant coil currents i_k, all supply voltages v_k are zero and the power supplies deliver no output. Thus, the stored energy W_{mag} is constant:

$$W_{mag} = \iiint_V \int_0^{\mathbf{B}} \mathbf{H} \cdot d\tilde{\mathbf{B}} \, dV = \text{const.} \tag{2.57}$$

A displacement $\mathbf{r}$ of any component of this system (coil or ferromagnetic component) leads to a mechanical work W_{mech}:

$$W_{mech} = \int_0^{\mathbf{r}} \mathbf{F} \cdot d\tilde{\mathbf{r}}, \tag{2.58}$$

and to a change of the stored magnetic energy ΔW_{mag}:

$$\Delta W_{mag} = W_{mag}^{(\mathbf{r})} - W_{mag}^{(0)} = \iiint_V \int_0^{\mathbf{B}^{(\mathbf{r})}} \mathbf{H} \cdot d\tilde{\mathbf{B}}\, dV - \iiint_V \int_0^{\mathbf{B}^{(0)}} \mathbf{H} \cdot d\tilde{\mathbf{B}}\, dV \tag{2.59}$$

where the superscripts $^{(0)}$ and $^{(\mathbf{r})}$ denote the quantity before and after the displacement. Furthermore, the power supplies have to do additional work W_{source} to keep the currents constant. This is caused by induced voltages v_k in the coils due to a change of the flux linkages ψ_k in the coils:

$$v_k = -\frac{d\psi_k}{dt} = -\frac{\partial \psi_k}{\partial \mathbf{r}} \frac{d\mathbf{r}}{dt}, \tag{2.60}$$

and leads for W_{source} to

$$\begin{aligned} W_{source} &= \sum_{k=1}^{N} \int_0^t i_k v_k d\tau = \sum_{k=1}^{N} i_k \int_0^t v_k d\tau = \sum_{k=1}^{N} i_k \int_0^t \left(-\frac{\partial \psi_k}{\partial \mathbf{r}} \frac{d\mathbf{r}}{d\tau} \right) d\tau \\ &= -\sum_{k=1}^{N} i_k \int_0^{\mathbf{r}} \frac{\partial \psi_k}{\partial \tilde{\mathbf{r}}} \cdot d\tilde{\mathbf{r}} = -\sum_{k=1}^{N} i_k \int_{\psi_k^{(0)}}^{\psi_k^{(\mathbf{r})}} d\tilde{\psi}_k = -\sum_{k=1}^{N} i_k \left(\psi_k^{(\mathbf{r})} - \psi_k^{(0)} \right) \\ &= \sum_{k=1}^{N} i_k \psi_k^{(0)} - \sum_{k=1}^{N} i_k \psi_k^{(\mathbf{r})}. \end{aligned} \tag{2.61}$$

The expression $\sum_{k=1}^{N} i_k \psi_k$ can be transformed into a corresponding volume integral by freezing the permeability in the whole domain. Thus linearity is enforced and a decomposition of $\mathbf{B}$ and $\mathbf{H}$ into coil related components $\mathbf{B}_k$ and $\mathbf{H}_k$ is possible:

$$\mathbf{B} = \sum_{k=1}^{N} \mathbf{B}_k; \quad \mathbf{H} = \sum_{k=1}^{N} \mathbf{H}_k. \tag{2.62}$$

The magnetic energy of the k^{th} coil with constant inductance (linear case) is defined as

$$W_{mag}^k = \frac{L_k i_k^2}{2} = \frac{\psi_k i_k}{2}, \tag{2.63}$$

or written with field quantities:

$$W_{mag}^k = \frac{1}{2} \iiint_V \mathbf{H}_k \cdot \mathbf{B}_k dV. \tag{2.64}$$

Thus, the expression $i_k \psi_k$ is equal to the volume integral of $\mathbf{H}_k \cdot \mathbf{B}_k$ and (2.61) can be rewritten as

$$W_{source} = \sum_{k=1}^{N} \iiint_V \mathbf{H}_k^{(0)} \cdot \mathbf{B}_k^{(0)} dV - \sum_{k=1}^{N} \iiint_V \mathbf{H}_k^{(\mathbf{r})} \cdot \mathbf{B}_k^{(\mathbf{r})} dV \tag{2.65}$$

Due to the conservation of energy in an isolated system, the total energy is constant:

$$W_{source} + \Delta W_{mag} + W_{mech} = 0. \tag{2.66}$$

Using (2.59) and (2.65) leads to

$$\begin{aligned} W_{mech} = &- \left(\iiint_V \int_0^{\mathbf{B}^{(\mathbf{r})}} \mathbf{H} \cdot d\tilde{\mathbf{B}}\, dV - \iiint_V \int_0^{\mathbf{B}^{(0)}} \mathbf{H} \cdot d\tilde{\mathbf{B}}\, dV \right) \\ &- \left(\sum_{k=1}^{N} \iiint_V \mathbf{H}_k^{(0)} \cdot \mathbf{B}_k^{(0)} dV - \sum_{k=1}^{N} \iiint_V \mathbf{H}_k^{(\mathbf{r})} \cdot \mathbf{B}_k^{(\mathbf{r})} dV \right) \\ = &\iiint_V \mathbf{H}^{(\mathbf{r})} \cdot \mathbf{B}^{(\mathbf{r})} dV - \iiint_V \int_0^{\mathbf{B}^{(\mathbf{r})}} \mathbf{H} \cdot d\tilde{\mathbf{B}}\, dV \\ &- \left(\iiint_V \mathbf{H}^{(0)} \cdot \mathbf{B}^{(0)} dV - \iiint_V \int_0^{\mathbf{B}^{(0)}} \mathbf{H} \cdot d\tilde{\mathbf{B}}\, dV \right) \end{aligned} \tag{2.67}$$

The expressions on the right side are equal to the magnetic co-energy W_{co} defined as

$$W_{co} := \iiint_V \mathbf{H} \cdot \mathbf{B} dV - \iiint_V \int_0^{\mathbf{B}} \mathbf{H} \cdot d\tilde{\mathbf{B}}\, dV. \tag{2.68}$$

Thus, (2.67) can be rewritten as

$$\int_0^{\mathbf{r}} \mathbf{F} \cdot d\tilde{\mathbf{r}} = W_{co}^{(\mathbf{r})} - W_{co}^{(0)} = \int_0^{\mathbf{r}} \nabla W_{co} \cdot d\tilde{\mathbf{r}}, \tag{2.69}$$

using (2.58) for the mechanical work. Finally, the force can be identified as the gradient of the magnetic co-energy

$$\mathbf{F} = \nabla W_{co}. \tag{2.70}$$

2.2 Finite element method

The history of the finite element method (FEM) started in the middle of the 20th century and it was primarily introduced in mechanical engineering. The application in electrical engineering started in the 1970s. Nowadays, the finite element method is used in almost all fields of engineering. This fast deployment is mainly caused by the rapid development of computer systems and thus the rise of available computing power.

This section summarizes the finite element method, especially its application for electromagnetic simulations. Furthermore, the typically used formulations for solving electromagnetic problems are presented. The focus thereby is on problems that typically occur in the simulation of electrical machines.

2.2.1 Basics of the finite element method

The finite element method is a numerical method for approximately solving boundary value problems [33]. This family of problems occurs in many technical fields where the problem is described by differential equations within a problem domain Ω. Additionally, a set of explicitly given boundary conditions at the domain boundary $\Gamma := \partial\Omega$ is required to make the solution unique. In mathematical notation this problem can be written as

$$\mathcal{L}(\phi) = f, \tag{2.71}$$

with the differential operator $\mathcal{L}(.)$, the excitation function f and the unknown quantity ϕ in Ω. At the domain boundary several constraints can be used. These mean in the simplest case prescribing of the solution itself (Dirichlet condition) or the derivative of the solution with respect to the boundary's normal direction vectors (Neumann condition). In addition, more complicated conditions can be formulated, for example impedance or absorbing conditions.

However, instead of solving the boundary value problem exactly, an alternative formulation of the problem can be used. Thereby, the solution ϕ is approximated by N expansion (or basis) functions v_i as

$$\tilde{\phi} = \sum_{i=1}^{N} c_i v_i, \tag{2.72}$$

with the approximated solution $\tilde{\phi}$ and the corresponding coefficients c_i. These coefficients are unknown and have to be determined during the solution process. Under the assumption that the chosen basis functions v_i are able to describe the solution exactly in the whole domain, the exact solution will be found. However, this is not the case in general and thus the solution found is only an approximation. The most commonly used technique for determining the unknown coefficients is the Galerkin method.

Galerkin method

The Galerkin method [33] is a weighted residual method. That means that the residual r defined as

$$r = \mathcal{L}\left(\tilde{\phi}\right) - f = \mathcal{L}\left(\sum_{i=1}^{N} c_i v_i\right) - f \tag{2.73}$$

is minimized for the approximated solution $\tilde{\phi}$ of the boundary-value problem given in (2.71). For the exact solution the residual vanishes in the whole domain leading to

$$\int_\Omega r d\Omega = 0. \tag{2.74}$$

Without doubt, this equation cannot be satisfied for $\tilde{\phi}$ in general. However, it can be assumed that for some weighting functions w_i the weighted residual integral vanishes:

$$\int_\Omega w_i r \, d\Omega = 0. \tag{2.75}$$

This approach leads to the general formulation of the weighted residual method. For the Galerkin method the expansion functions v_i for calculating $\tilde{\phi}$ are also used as weighting functions $w_j := v_j$. This leads finally to N equations

$$\int_\Omega v_j \mathcal{L}\left(\sum_{i=1}^{N} c_i v_i\right) - v_j f d\Omega = 0 \quad \text{for } 1 \leq j \leq N, \tag{2.76}$$

for all N unknown coefficients c_i.

Domain discretization

The support of a function is defined as the subset of the domain where the function is not zero. For the Galerkin method, the expansion functions v_i for the trial function $\tilde{\phi}$ in (2.72) can be freely chosen with respect to the support of those functions. Thus, the support of the expansion functions covers the whole domain in general. For a good approximation of the real solution these expansion functions need to be able to roughly approximate the solution itself. Therefore, they can become very complex and thus difficult to find. However, if the support of these expansion functions is reduced to subdomains, each v_i needs only to approximate the solution in the supported subdomain only. This requirement is much easier to achieve and leads to simpler expansion functions. This approach is illustrated for the one-dimensional case in Fig. 2.3. The expansion functions

$$v_i(x) = \begin{cases} 1 - \frac{x - x_{i-1}}{x_i - x_{i-1}} & \text{if } x_{i-1} < x < x_i, \\ 1 - \frac{x - x_i}{x_{i+1} - x_i} & \text{if } x_i \leq x < x_{i+1}, \\ 0 & \text{otherwise,} \end{cases} \tag{2.77}$$

with a support reduced to $\Omega_i = [x_{i-1},\, x_{i+1}]$ are utilized to approximate the solution for the complete domain $\Omega = [x_0,\, x_4]$. The boundary conditions $\phi(x_0)$ and $\phi(x_4)$ are the coefficients of the corresponding approximation functions v_0 and v_4.

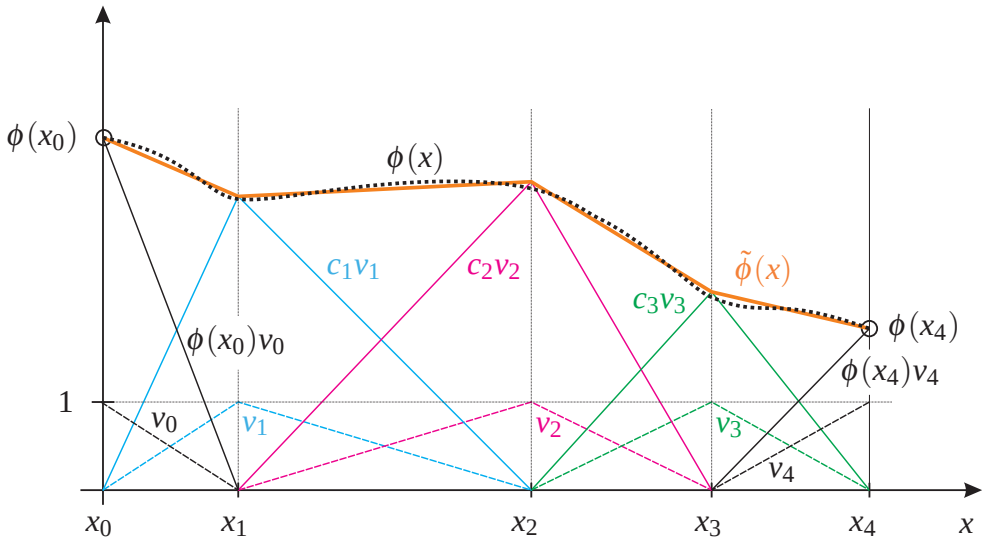

Figure 2.3: Solution and approximated solution using hat function for each subdomain

Finite elements

The example shown in Fig. 2.3 illustrates the finite element method although no finite elements have been defined yet. This definition is given in this subsection. Obviously, all subdomains defined in subsection 2.2.1 are overlapping, caused by the definition of the expansion functions and their support. However, the subdomains Ω_i can be also defined as intervals $[x_{i-1},\ x_i]$ and all v_i can be split at x_i. This leads finally to four subdomains and eight expansion functions for the example shown in Fig. 2.3. For each subdomain two basis functions are defined . These non-overlapping subdomains with the corresponding basis functions are called finite elements (FE). In case of the example these are one-dimensional (1D), linear finite elements.

The finite elements can be also higher dimensional. Triangular- and quadrilateral- elements are mainly used in two-dimensional (2D) space and tetrahedral-, triangular prism- and hexahedral elements are mostly used for three-dimensional (3D) problems. The finite elements comprise several nodes, the corresponding basis functions and shape functions. The shape functions describe the shape of the FE and thus the subdomain boundaries by the edges and facets of the FE. Typically, linear or quadratic shape functions are used. If the shape functions and basis functions are polynomials of the same order the elements are called isoparametric. Fig. 2.4 shows several examples of 2D and 3D elements.

The expansion functions defined in (2.77) are node based. This approach works well for the approximation of scalar fields like potentials or temperature in 2D or 3D case. For the approximation of vectorial fields, edge based expansion functions are commonly used. This approach assigns each edge of the finite element the value of the line integral of the vectorial field quantity along the corresponding edge [8]. Therefore, the continuity

of the tangential component of the field between adjacent elements is fulfilled exactly. An example element is shown in Fig. 2.4.d.

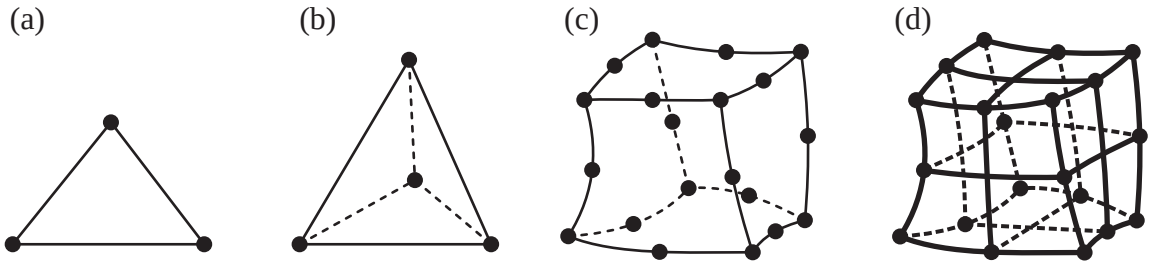

Figure 2.4: Examples of finite elements [33]: (a) 2D: Linear triangular nodal element with 3 nodes. (b) 3D: Linear tetrahedral nodal element with 4 nodes. (c) 3D: Quadratic hexahedral nodal element with 20 nodes. (d) 3D: Quadratic hexahedral edge element with 20 nodes and 36 edges.

2.2.2 FEM formulations of quasi-static electromagnetic fields

The differential operator in (2.71) was defined generally and thus abstract in the sense of engineering. In this subsection the boundary value problems that occur when modeling electrical machines are discussed. The system of differential equations is defined by the quasi-static Maxwell's equations (2.34)-(2.38), leading to eddy current problems. Such problems involve two domain groups, the group of conducting domains Ω_C and the group of non-conducting domains Ω_N. Current fed coils and voltage fed coils are included in Ω_N. Permanent magnets can be modelled in the whole domain using appropriate material properties. This is a boundary value problem for $\mathbf{E}_C$, $\mathbf{J}_C$, $\mathbf{B}_C$, $\mathbf{H}_C$ in Ω_C and $\mathbf{B}_N$, $\mathbf{H}_N$ in Ω_N. The complete set of differential equations is given as:

$$\begin{array}{cc} \text{in } \Omega_C\text{:} & \text{in } \Omega_N\text{:} \\ \nabla \times \mathbf{H}_C = \mathbf{J}_C, & \nabla \times \mathbf{H}_N = \mathbf{J}_N, \\ \nabla \times \mathbf{E}_C = -\frac{\partial \mathbf{B}_C}{\partial t}, & \\ \nabla \cdot \mathbf{B}_C = 0, & \nabla \cdot \mathbf{B}_N = 0, \\ \mathbf{B}_C = \mu \mathbf{H}_C, & \mathbf{B}_N = \mu \mathbf{H}_N, \\ \mathbf{J}_C = \sigma \mathbf{E}_C, & \end{array} \tag{2.78}$$

with the boundary conditions

$$\begin{array}{ccc} \text{in } \Omega_C\text{:} & \text{on } \Gamma_i : & \text{in } \Omega_N\text{:} \\ \mathbf{H}_C \times \mathbf{n} = \mathbf{0} \text{ on } \Gamma_{HC}, & \mathbf{H}_C \times \mathbf{n} - \mathbf{H}_N \times \mathbf{n} = \mathbf{0}, & \mathbf{H}_N \times \mathbf{n} = \mathbf{K} \text{ on } \Gamma_{HN}, \\ \mathbf{E}_C \times \mathbf{n} = \mathbf{0} \text{ on } \Gamma_{EC}, & \mathbf{B}_C \cdot \mathbf{n} - \mathbf{B}_N \cdot \mathbf{n} = 0, & \mathbf{B}_N \cdot \mathbf{n} = -b \text{ on } \Gamma_{BN} \end{array} \tag{2.79}$$

where Γ_i is the interface between Ω_C and Ω_N, $\mathbf{n}$ is the surface normal vector, $\mathbf{K}$ is an impressed vector field and b is an impressed scalar field. The topology of such problems is

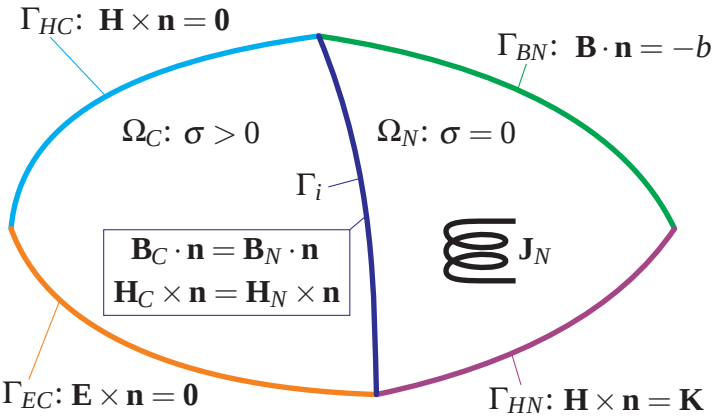

Figure 2.5: General topology of an eddy current problem.

shown in Fig. 2.5. The solution consists of the magnetic field distribution in the whole domain as well as the eddy current distribution in the conducting domain. Two formulations are commonly used to describe such 3D eddy current problems. These are the $\mathbf{A},V$-$\mathbf{A}$-formulation and the $\mathbf{T},\Phi$-Φ-formulation briefly described in the following subsections.

$\mathbf{A},V$-$\mathbf{A}$-formulation

The $\mathbf{A},V$-$\mathbf{A}$-formulation utilizes the magnetic vector potential $\mathbf{A}$ and the electric scalar potential V in Ω_C and $\mathbf{A}$ in Ω_N for describing the eddy current problem. The introduction of $\mathbf{A}$ is justified by Gauss's law for magnetism (2.36). Due to the fact that the divergence of the curl of any vector field $\mathbf{X}$ in $\mathbb{R}^3$ is identically zero:

$$\nabla\cdot(\nabla\times\mathbf{X})\equiv 0, \tag{2.80}$$

the magnetic flux density $\mathbf{B}$ can be assumed to be the curl of $\mathbf{A}$:

$$\mathbf{B}=\nabla\times\mathbf{A}. \tag{2.81}$$

The quasi-static Ampére's law (2.34) leads to

$$\nabla\times\left(\mu^{-1}\nabla\times\mathbf{A}\right)=\mathbf{J}, \tag{2.82}$$

and the quasi-static Faraday's law (2.35) to

$$\nabla\times\mathbf{E}=-\nabla\times\frac{\partial\mathbf{A}}{\partial t}. \tag{2.83}$$

Note that $\mathbf{A}$ is not unique, since its divergence has not been defined. Taking into account that the curl of the gradient of any scalar function X is identically zero:

$$\nabla\times(\nabla X)\equiv\mathbf{0}, \tag{2.84}$$

the electric field intensity vector $\mathbf{E}$ can be written as

$$\mathbf{E} = -\frac{\partial \mathbf{A}}{\partial t} - \nabla V = -\frac{\partial}{\partial t}(\mathbf{A} + \nabla v), \tag{2.85}$$

with the modified electric scalar potential v. The current density vector $\mathbf{J}$ can be rewritten as

$$\mathbf{J} = -\sigma\left(\frac{\partial \mathbf{A}}{\partial t} + \nabla V\right) = -\sigma\frac{\partial}{\partial t}(\mathbf{A} + \nabla v). \tag{2.86}$$

The introduction of $\mathbf{A}$ and V (or v) satisfies (2.35) and (2.36) implicitly and leads with (2.27) and (2.38) finally to

$$\nabla \times \left(\mu^{-1}\nabla \times \mathbf{A}\right) + \sigma\frac{\partial \mathbf{A}}{\partial t} + \sigma\nabla V = 0 \text{ in } \Omega_C, \tag{2.87}$$

$$\nabla \cdot \left(\sigma\frac{\partial \mathbf{A}}{\partial t} + \sigma\nabla V\right) = 0 \text{ in } \Omega_C, \tag{2.88}$$

$$\nabla \times \left(\mu^{-1}\nabla \times \mathbf{A}\right) = \mathbf{J}_N \text{ in } \Omega_N \tag{2.89}$$

where $\mathbf{J}_N$ is the impressed current density for modeling coils in Ω_N. The boundary conditions are:

$$\left(\mu^{-1}\nabla \times \mathbf{A}\right) \times \mathbf{n} = \mathbf{0} \text{ on } \Gamma_{HC}, \tag{2.90}$$

$$\sigma\left(\frac{\partial \mathbf{A}}{\partial t} + \nabla V\right) \cdot \mathbf{n} = 0 \text{ on } \Gamma_{HC}, \tag{2.91}$$

$$\mathbf{n} \times \mathbf{A} = \mathbf{0} \text{ and } V = \text{const on } \Gamma_{EC}, \tag{2.92}$$

$$\left(\mu^{-1}\nabla \times \mathbf{A}\right) \times \mathbf{n} = \mathbf{K} \text{ on } \Gamma_{HN}, \tag{2.93}$$

$$\mathbf{n} \times \mathbf{A} = \boldsymbol{\alpha} \text{ on } \Gamma_{BN}. \tag{2.94}$$

Equation (2.91) is a consequence of (2.87) and (2.90). Due to the vanishing tangential components of $\mathbf{H}$, both the normal component of $\nabla \times \mathbf{H}$ and the normal component of $\mathbf{J}$ are zero. It is pointed out that, $\mathbf{A}$ and V (or v) are not unique. Their uniqueness can be achieved by gauging (i.e. specifying the divergence of $\mathbf{A}$), but this is not necessary to describe the field quantities uniquely.

$\mathbf{T}, \Phi$-Φ-formulation

The $\mathbf{T}, \Phi$-Φ-formulation utilizes the current vector potential $\mathbf{T}$ and the magnetic scalar potential Φ in Ω_C and Φ in Ω_N for describing the eddy current problem [8]. The introduction of $\mathbf{T}$ is motivated by the solenoidality of $\mathbf{J}$ in the quasi-static case, see (2.38). Due to (2.80), the current density $\mathbf{J}$ can be assumed to be the curl of $\mathbf{T}$:

$$\mathbf{J} = \nabla \times \mathbf{T}. \tag{2.95}$$

The quasi-static Ampére's law (2.34) leads to

$$\nabla \times \mathbf{H} = \nabla \times (\mathbf{T} + \mathbf{T}_0), \tag{2.96}$$

with the reduced current vector potential $\mathbf{T}$ to describe the eddy currents in Ω_C and the impressed current vector potential $\mathbf{T}_0$ prescribing the total current in current fed coils in the whole problem domain:

$$\nabla \times \mathbf{T}_0 = \mathbf{J}_N. \tag{2.97}$$

Using (2.84) leads to

$$\mathbf{H} = \mathbf{T} + \mathbf{T}_0 - \nabla \cdot \Phi \text{ in } \Omega_C, \tag{2.98}$$

$$\mathbf{H} = \mathbf{T}_0 - \nabla \cdot \Phi \text{ in } \Omega_N. \tag{2.99}$$

Using Faraday's law (2.35) and Gauss' law for magnetism (2.36), the differential equations for the $\mathbf{T}, \Phi$-Φ-formulation are

$$\nabla \times \left(\sigma^{-1} \nabla \times \mathbf{T}\right) + \frac{\partial}{\partial t}\left(\mu\left(\mathbf{T} - \nabla\Phi\right)\right) = -\nabla \times \left(\sigma^{-1} \nabla \times \mathbf{T}_0\right) - \frac{\partial}{\partial t}\left(\mu \mathbf{T}_0\right) \text{ in } \Omega_C, \tag{2.100}$$

$$\nabla \cdot \left(\mu \mathbf{T} - \mu \nabla \Phi\right) = -\nabla \cdot \left(\mu \mathbf{T}_0\right) \text{ in } \Omega_C, \tag{2.101}$$

$$\nabla \cdot \left(\mu \nabla \Phi\right) = \nabla \cdot \left(\mu \mathbf{T}_0\right) \text{ in } \Omega_N. \tag{2.102}$$

The corresponding boundary conditions are

$$\mathbf{n} \times \mathbf{T} = \mathbf{n} \times \mathbf{T}_0 \text{ and } \Phi = \text{const on } \Gamma_{HC}, \tag{2.103}$$

$$\left(\sigma^{-1} \nabla \times \mathbf{T}\right) \times \mathbf{n} = -\left(\sigma^{-1} \nabla \times \mathbf{T}_0\right) \times \mathbf{n} \text{ on } \Gamma_{EC}, \tag{2.104}$$

$$\mu\left(\mathbf{T} - \nabla\Phi\right) \cdot \mathbf{n} = \mu \mathbf{T}_0 \cdot \mathbf{n} \text{ on } \Gamma_{EC}, \tag{2.105}$$

$$\Phi = \text{const on } \Gamma_{HN}, \tag{2.106}$$

$$\mu \frac{\partial \Phi}{\partial \mathbf{n}} = b + \mu \mathbf{T}_0 \cdot \mathbf{n} \text{ on } \Gamma_{BN}. \tag{2.107}$$

None of the introduced quantities $\mathbf{T}$, $\mathbf{T}_0$ and Φ are defined uniquely. Furthermore, for multiply connected domains Ω_C, additional constraints are required. It is mentioned that the benefit of this formulation is the lower number of unknowns compared with the $\mathbf{A}, V$-$\mathbf{A}$-formulation. This is due to the fact that only a scalar field is used in the non-conducting domain to describe the problem instead of a vector field.

2.3 Interpolation methods

In this section, a brief overview of interpolation methods is given and the cubic spline interpolation method is explained in detail. Interpolation is a technique for the approximation of a function defined by sampling points. Such sampled functions are typically created by series of measurements or simulations. The sampled quantities and the corresponding test parameters are stored in look-up tables. For test parameter values not sampled, the continuity of the sampled quantity is assumed. In most relevant cases, this is fulfilled for physical quantities. The quality of the interpolation in the sense of accuracy, stability and calculation cost depends on the used interpolation method and the number of sampling points.

Interpolation methods can be classified into two main categories. The first category uses interpolation functions with a support in the whole parameter space. This method is well suited if the function to interpolate is known very well. In such cases, a few sampling points are sufficient to determine the interpolation function parameters. Examples of this category are polynomial interpolation (Lagrange polynomials), exponential interpolation or trigonometric interpolation.

The second category uses functions with a support reduced to a subdomain of the parameter space. Thus, this approach employs simpler interpolation functions and leads to a faster evaluation. Polynomials of a low degree are widely used for the interpolation due to the simplicity of their evaluation. For example, the piecewise constant (zero-degree) interpolation method (Fig. 2.6a) and the piecewise linear (first degree) interpolation method (Fig. 2.6b) belong to this family. The use of polynomials with a degree of three leads to the cubic spline interpolation method (Fig. 2.6c) described in the next subsection. The main advantage of a cubic spline technique is that it leads to a continuous and smooth

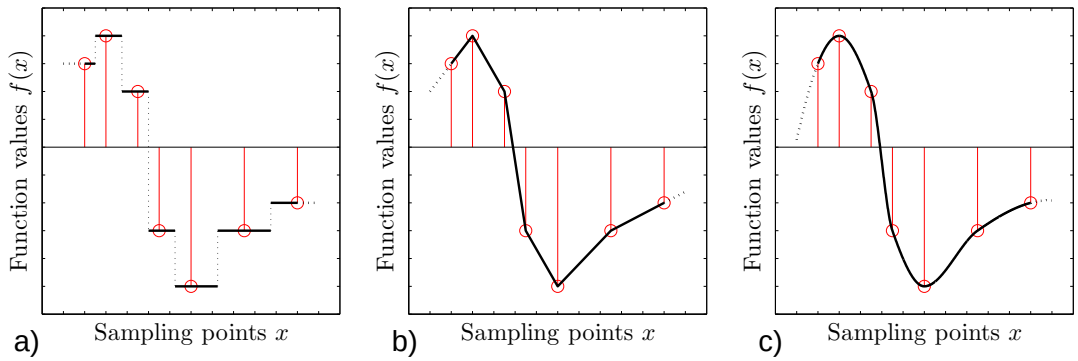

Figure 2.6: Examples of piecewise polynomial interpolation methods: (a) Piecewise constant interpolation: The function value is not continuous. (b) Piecewise linear interpolation: The function value is continuous , the first derivative is discontinuous (C^0-continuity). (c) Cubic spline interpolation: The function value, the first derivative and the second derivative are continuous (C^2-continuity).

interpolation function even in higher dimensional case.

2.3.1 Cubic spline interpolation method in one dimension

The cubic spline interpolation method utilizes cubic polynomials for a piecewise interpolation. For a dataset of M sampled data points (x, y), the interpolation polynomial $p_\kappa(x)$ for the κ^{th} of the $M-1$ segments is defined as:

$$p_\kappa(x) = a_0^\kappa + a_1^\kappa (x - x_\kappa) + a_2^\kappa (x - x_\kappa)^2 + a_3^\kappa (x - x_\kappa)^3, \tag{2.108}$$

with the spline coefficients a_0^κ, a_1^κ, a_2^κ, a_3^κ and

$$x_\kappa \leq x < x_{\kappa+1}, \tag{2.109}$$
$$1 \leq \kappa \leq M-1. \tag{2.110}$$

All $4(M-1)$ spline coefficients are defined by four constraints per segment. These are:

$$p_\kappa(x_\kappa) = y_\kappa \text{ and } p_\kappa(x_{\kappa+1}) = y_{\kappa+1}, \tag{2.111}$$
$$p'_\kappa(x_{\kappa+1}) = p'_{\kappa+1}(x_{\kappa+1}), \tag{2.112}$$
$$p''_\kappa(x_{\kappa+1}) = p''_{\kappa+1}(x_{\kappa+1}), \tag{2.113}$$

with the first derivate $p'(x)$ and the second derivative $p''(x)$. The constraints defined in (2.111) enforce continuity of the function to interpolate. Obviously, all $M-1$ coefficients a_0^κ are identified as $a_0^\kappa = y_\kappa$. The constraints in (2.112) and (2.113) enforce a smooth connection of the segments at all $M-2$ intermediate sampling points. Thus, this approach leads to a continuous and smooth interpolation of the function value. Furthermore, the first order derivatives are smooth and the second order derivatives are still continuous (C^2-continuity) [10].

Taking into account that all coefficients a_0^κ have already been determined, the resulting system of equations can be written as:

$$\begin{bmatrix} s_1 & s_1^2 & s_1^3 & 0 & 0 & 0 & \cdots & 0 & 0 & 0 \\ 1 & 2s_1 & 3s_1^2 & -1 & 0 & 0 & \cdots & 0 & 0 & 0 \\ 0 & 2 & 6s_1 & 0 & -2 & 0 & \cdots & 0 & 0 & 0 \\ 0 & 0 & 0 & s_2 & s_2^2 & s_2^3 & \cdots & 0 & 0 & 0 \\ 0 & 0 & 0 & 1 & 2s_2 & 3s_2^2 & \cdots & 0 & 0 & 0 \\ 0 & 0 & 0 & 0 & 2 & 6s_2 & \cdots & 0 & 0 & 0 \\ \vdots & \vdots & \vdots & \vdots & \vdots & \vdots & \ddots & \vdots & \vdots & \vdots \\ 0 & 0 & 0 & 0 & 0 & 0 & \cdots & s_{M-1} & s_{M-1}^2 & s_{M-1}^3 \end{bmatrix} \begin{pmatrix} a_1^1 \\ a_2^1 \\ a_3^1 \\ a_1^1 \\ a_2^1 \\ \vdots \\ a_2^M \\ a_3^M \end{pmatrix} = \begin{pmatrix} y_2 - y_1 \\ 0 \\ 0 \\ y_3 - y_2 \\ 0 \\ \vdots \\ 0 \\ y_M - y_{M-1} \end{pmatrix}, \tag{2.114}$$

with the segment width $s_\kappa := x_{\kappa+1} - x_\kappa$ and a system matrix with $3(M-1)$ columns and $3(M-1)-2$ rows.

For a unique solution, two additional equations are required. They can be freely chosen but in many cases they are used to define the behavior of the spline at the boundaries. This is done by specifying $p'(x)$ or $p''(x)$ at the first and last sampling points.

A natural choice is to force the second order derivatives $p_1''(x_1)$ and $p_{M-1}''(x_M)$ to vanish:

$$p_1''(x_1) = 0 \quad \text{and} \quad p_{M-1}''(x_M) = 0. \tag{2.115}$$

This ansatz will be referred to as natural boundary condition. It allows a smooth contact with a straight line for linear extrapolation.

For periodic functions, periodicity can be enforced by

$$p_1'(x_1) = p_{M-1}'(x_M) \text{ and } p_1''(x_1) = p_{M-1}''(x_M), \tag{2.116}$$

with the constraint $y_1 = y_M$.

The resulting cubic spline interpolation for a dataset with four sampling points and natural boundary conditions is shown in Fig. 2.7. Furthermore, all used third order polynomials and the linear functions for extrapolation in both outer segments are shown.

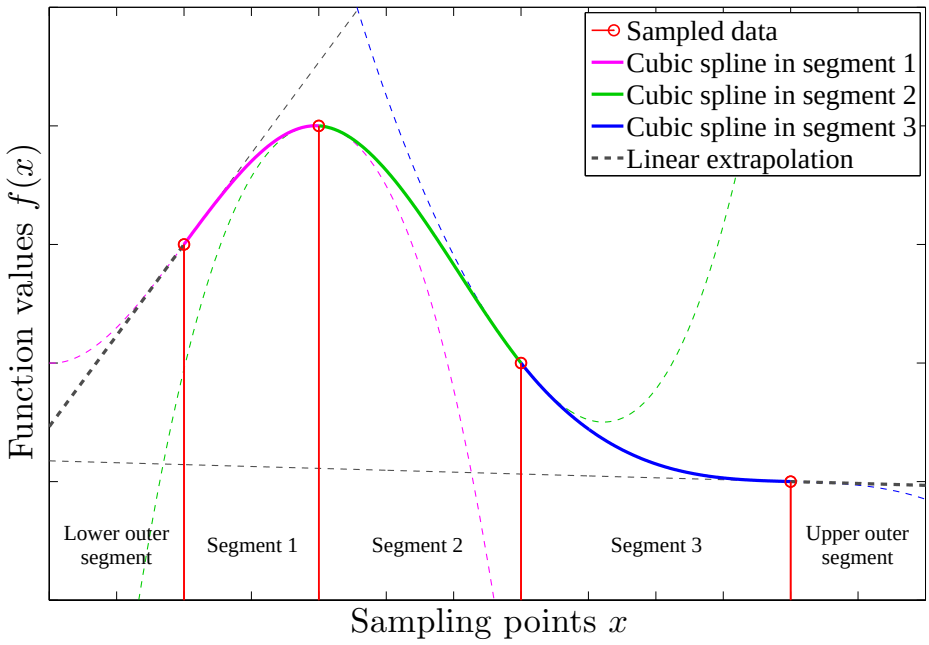

Figure 2.7: Example for a cubic spline interpolation with a dataset of four sampling points and with natural boundary conditions. A linear extrapolation is shown in the lower and upper outer segment.

2.3.2 Higher dimensional cubic spline interpolation

Under the assumption of a rectangular sampling grid, the cubic spline interpolation method can be easily extended for higher dimensional interpolation tasks. Such a sampling grid leads for each segment to a rectangle in 2D or a rectangular cuboid in 3D. The interpolation polynomial in each segment becomes multivariate. For a function in 3D parameter space with the parameters x, y and z and for the ι^{th} segment in x-direction, the κ^{th} segment in y-direction and the λ^{th} segment in z-direction, the tri-cubic polynomial can be written as

$$p_{\iota,\kappa,\lambda}(x,y,z) = \sum_{k=0}^{3}\sum_{j=0}^{3}\sum_{i=0}^{3} a_{k,j,i}^{\iota,\kappa,\lambda}\ (x-x_\iota)^i\ (y-y_\kappa)^j\ (z-z_\lambda)^k, \tag{2.117}$$

with $x_\iota \leq x < x_{\iota+1}$, $y_\kappa \leq y < y_{\kappa+1}$ and $z_\lambda \leq z < z_{\lambda+1}$. This polynomial is defined by $4^3 = 64$ coefficients $a_{0,0,0}$ to $a_{3,3,3}$. Thus 64 equations per segment are required for a unique representation. As proven in [43], for C^1-continuity at the segment boundaries of adjacent segments, continuity of the function value (F), the first order partial derivatives (f_x, f_y, f_z), the second order mixed partial derivatives (f_{xy}, f_{xz}, f_{yz}) and the third order mixed partial derivative (f_{xyz}) at all sampling points have to be enforced. This leads to 8 equations for each of the 8 vertices of the rectangular cuboid shaped segment.

2.3.3 Evaluation of polynomials

The evaluation of polynomials can be done very efficiently using Horner's method

$$p(x) = \sum_{i=0}^{N} a_i\, x^i = a_0 + a_1 x^1 + a_2 x^2 + \cdots + a_N x^N \tag{2.118}$$

$$= a_0 + x\,(a_1 + x\,(a_2 + \cdots + x\,(a_{N-1} + x\,a_N)\cdots)) \tag{2.119}$$

where $p(x)$ is a polynomial of degree N. Compared with the direct evaluation of the monomial form (2.118) of the polynomial which requires at least $2N-1$ floating point multiplications, Horner's method (2.119) requires only N floating point multiplications. This is the absolute minimum for the evaluation of a polynomial with a degree of N. Furthermore, the numerical errors occurring using Horner's method are less than evaluating the monomials directly [30].

Horner's method can be also applied to multivariate polynomials, e.g. for a polynomial in two variables x and y it has the form:

$$\begin{aligned} p(x,y) &= \sum_{j=0}^{M}\sum_{i=0}^{N} a_{j,i}\, x^i\, y^j = \sum_{j=0}^{M} p_j(x)\, y^j = \\ &= p_0(x) + y\,(p_1(x) + y\,(p_2(x) + \cdots + y\,(p_{M-1}(x) + y\,p_M(x))\cdots)), \end{aligned} \tag{2.120}$$

with the sub-polynomials $p_j(x)$ again evaluated by Horner's method. This cascaded approach also gets by with the minimum number of floating point operations.

2.4 Electrical machines

In this section a short overview of electrical machines is given. An electrical machine in this sense is a rotating machine that converts electrical energy into mechanical energy and vice versa. Therefore, an electrical machine consists of (at least) two components: the fixed stator and the movable (typically pivot-mounted) rotor. Both components are part of the magnetic circuit.

From the electrical point of view, an electrical machine consists of at least two magnetically coupled coil systems. One coil system is typically called excitation coil system and is responsible for the main flux generation. For machine types with a direct current (DC) fed excitation coil system, this coil system can be replaced by permanent magnets. The second coil system is called armature coil system. Within this coil system voltages are induced due to motion. This nomenclature is historically based on the mode of operation of DC-machines. Thus, it is only reasonably for DC machines and synchronous machines (SM), for induction machines (IM) this classification is not applicable. Commonly, one coil system is located on the stator, the other one on the rotor. However, reluctance machines, for instance, combine both coil systems on the stator.

2.4.1 Classification of electrical machines

Due to the high number of different machine designs any classification can only be done in very general terms [67]. A very simple classification for electrical machines can be carried out depending on the kind of energy conversation, i.e. one can distinguish between generators and motors. A generator transforms mechanical energy into electrical energy, a motor, in contrast, converts energy in the opposite direction. However, every electrical machine can work in motor mode as well as in generator mode. The working mode only depends on the external operating conditions and is thus independent of machine design.

Another classification can be done based on the configuration of the magnetic flux paths within the machine. For a cylindrical coordinate system with the axis of rotation along the z-axis (Fig. 2.8a) three main 2D configurations can be found.

The first configuration has the magnetic flux paths in the $r\phi$-plane. This leads to the conventional machine design with cylindrical rotor as shown in Fig. 2.8b. The air gap is of the shape of a cylinder barrel.

In contrast, the second configuration has the flux paths in the $z\varphi$-plane. This results in a machine with disc rotor (Fig. 2.8c). The air gap in this case is shaped as an annulus. In both configurations a hetero-polar magnetic field in rotational direction (φ-direction) occurs.

The third configuration is characterized by flux paths in the rz-plane. This leads to a homo-polar magnetic field in φ-direction as shown in Fig. 2.8d. For this configuration both cylinder barrel shaped and annular shaped air gaps are possible. It leads, for instance, to unipolar machines and transversal flux machines.

The magnetic flux paths in a machine could also have a more complex three dimensional

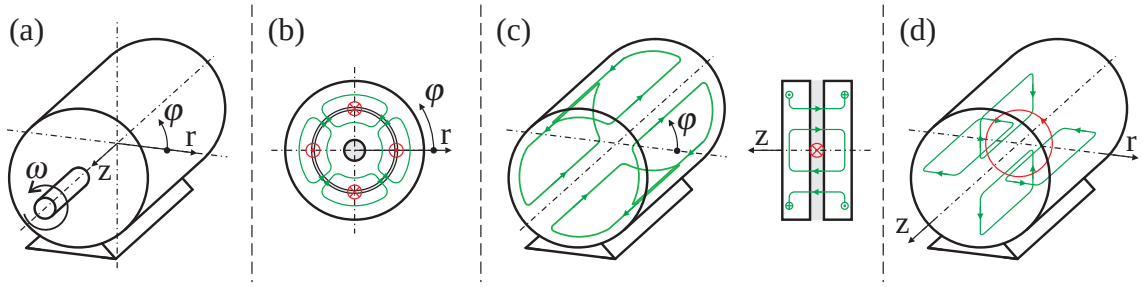

Figure 2.8: Machine classification based on the flux path (green) configuration [67]: (a) Definition of the reference system in polar coordinates: The axis of rotation is the z-axis. (b) Flux path configuration in $r\varphi$-plane: This leads to a cylindrical rotor with cylinder barrel shaped air gap (gray) and a z-directional current feed (red), i.e. the traditional machine design. (c) Flux path configuration in $z\varphi$-plane: This leads to a disc shaped rotor with a circular ring shaped air gap and a r-directional current feed. (d) Flux path configuration in rz-plane: This leads to a homo-polar magnetic field in rotational direction. For this flux path configuration both, cylindrical and disc shaped rotors are possible.

shape in general. The claw pole machine for instance belongs to this category. However, this classification mainly influences the structural form of the machine and allows the machine designer to customize the electrical machine to the available shape and amount of space. Note, that the electrical properties of the machine are not determined by this classification.

The next classification to be discussed in this work is based on the torque generation mechanism. The machine torque can be calculated using the Maxwell stress tensor as shown in (2.55). Using a cylinder barrel shaped surface $\mathbf{S}$ and $\overline{\mathbf{T}}$ in cylinder coordinates leads to

$$\mathbf{F} = \oiint_{\mathbf{S}} \overline{\mathbf{T}} \cdot d\mathbf{s} = \oiint_{\mathbf{S}} \begin{bmatrix} T_{rr} & T_{\varphi r} & T_{zr} \\ T_{\varphi r} & T_{\varphi\varphi} & T_{z\varphi} \\ T_{zr} & T_{z\varphi} & T_{zz} \end{bmatrix} \cdot \mathbf{e}_r ds = \oiint_{\mathbf{S}} \begin{pmatrix} T_{rr} \\ T_{\varphi r} \\ T_{zr} \end{pmatrix} ds, \tag{2.121}$$

with the tensor elements

$$T_{rr} = \frac{1}{\mu_0}\left(B_r^2 - \frac{1}{2}|\mathbf{B}|\right), \tag{2.122}$$

$$T_{\varphi r} = \frac{1}{\mu_0} B_\varphi B_r, \tag{2.123}$$

$$T_{zr} = \frac{1}{\mu_0} B_z B_r, \tag{2.124}$$

as shown in (2.56). This leads to the machine torque as

$$\boldsymbol{\tau} = \mathbf{r}_S \times \mathbf{F} = r_S \mathbf{e}_r \times \mathbf{F} = r_S F_\varphi = r_S \oiint_{\mathbf{S}} \frac{1}{\mu_0} B_\varphi B_r ds, \tag{2.125}$$

with the radius r_S of **S**. Only the interaction between the normal component B_r and the tangential component B_φ of the magnetic flux density leads to a tangential force component F_φ and thus to a torque. Furthermore, B_r and B_φ are periodical in circumferential direction. Therefore, a spatial Fourier decomposition for both components can be performed. This leads finally to the result that for any torque generation B_r-waves and B_φ-waves of the same ordinal number are required, else the integral in (2.125) vanishes. Furthermore, the phase shift between the corresponding B_r- and B_φ-waves must not be 90°, otherwise the integral in (2.125) vanishes, too. Depending on how these waves are generated, four mechanisms for the torque generation can be distinguished:

- Synchronous electro-dynamic torque
- Asynchronous electro-dynamic torque
- Reluctance torque
- Hysteresis torque

For this classification, DC machines and synchronous machines belong to the same category. DC machines use a commutator to keep the relative position between the rotor field and the stator field constant. Synchronous machines use a poly-phase armature coil system to generate a rotating field. This field rotates with the same speed as the rotor field and thus the relative position between the two fields is kept constant. Hence, a synchronous electro-dynamic torque is generated in both cases.

Induction machines (IM) belong to the second category. One poly-phase coil system generates a rotating magnetic field. This field induces voltages in the second poly-phase coil system. This leads to a current flow in the second coil system. The interaction between the fields of the two coil system finally leads to a torque generation. However, the induction process in the second coil system requires a relative movement between the rotating field and the rotor. Therefore, this torque generation is called asynchronous. Depending on the rotor design, induction machines can be further sub-classified into machines with a slip ring rotor and machines with a squirrel cage rotor.

Reluctance torque and hysteresis torque utilize material properties to generate torque. Thus the rotor of such machines is designed to be magnetically anisotropic in circumferential direction and includes no coil system.

It should be mentioned that more than one of these mechanisms typically occur in electrical machines simultaneously. However, for every machine, a primary mechanism can be found which is mainly responsible for the torque generation. All other mechanisms that occur are typically unwanted because they mainly produce torque harmonics and thus deteriorate the machine behavior.

2.4.2 Mode of operation

In this subsection, the general requirements for an electro-mechanical energy conversion are discussed. Therefore, a machine of only two coupled coils is assumed as shown in Fig.

2.9. This system can be assumed as isolated and an analysis of the power balance leads to

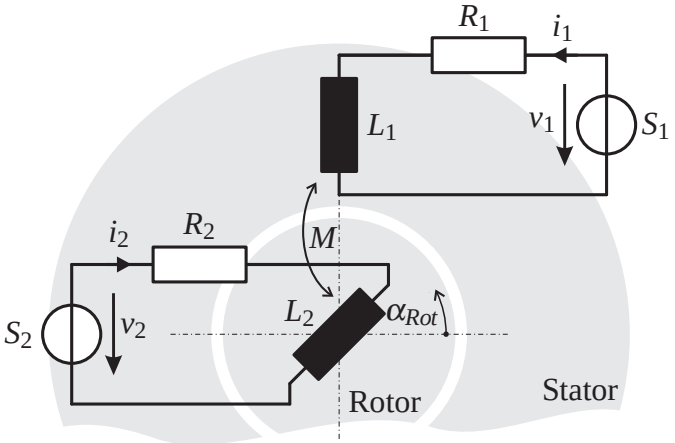

Figure 2.9: Electrical machine with two coupled coil systems, one is located on the stator and the other on the rotor. The electric network for a power balance analysis is shown.

$$P_{mech} + P_{source} + \frac{dW_{mag}}{dt} + P_{loss} = 0, \tag{2.126}$$

with the mechanical power P_{mech} at the shaft

$$P_{mech} = \tau \frac{d\alpha_{Rot}}{dt} \tag{2.127}$$

where τ denotes the machine torque, the electrical power P_{source} applied from the two voltage sources S_1, S_2

$$P_{source} = -v_1 i_1 - v_2 i_2, \tag{2.128}$$

the rate of change of the magnetic energy $\frac{dW_{mag}}{dt}$ in the two coils of the machine

$$\begin{aligned} \frac{dW_{mag}}{dt} &= \frac{d}{dt} \sum_{i=1}^{2} \sum_{j=1}^{2} \frac{1}{2} L_{ij} i_i i_j = \frac{d}{dt} \left(\frac{1}{2} L_1 i_1^2 + \frac{1}{2} L_2 i_2^2 + M i_1 i_2 \right) \\ &= \frac{1}{2} \frac{dL_1}{dt} i_1^2 + L_1 i_1 \frac{di_1}{dt} + \frac{1}{2} \frac{dL_2}{dt} i_2^2 + L_2 i_2 \frac{di_2}{dt} + \frac{dM}{dt} i_1 i_2 + M \frac{di_1}{dt} i_2 + M i_1 \frac{di_2}{dt}, \end{aligned} \tag{2.129}$$

and finally the losses P_{loss} that occur in the system

$$P_{loss} = P_{Cu} + P_{skin} + P_{eddy} + P_{hyst} + P_{frict} + P_{excess}, \tag{2.130}$$

with the copper losses P_{Cu} and the skin effect losses P_{skin} in the coils, the eddy current losses P_{eddy} and hysteresis losses P_{hyst} in the iron, the friction losses P_{frict} (e.g.: bearings,

air drag, ...) and finally the excess losses P_{excess} that combine all other losses (e.g.: deformation due to magnetostriction, radiated acoustic noise, ...). For simplicity only the copper losses

$$P_{Cu} = \sum_{i=1}^{2} R_i i_i^2 = R_1 i_1^2 + R_2 i_2^2 \tag{2.131}$$

in the two coils shall be considered.

According to circuit theory, the voltage equations for the two electric circuits can be written as

$$-v_1 + R_1 i_1 + \frac{d}{dt}(L_1 i_1 + M i_2) = 0, \tag{2.132}$$

$$-v_2 + R_2 i_2 + \frac{d}{dt}(L_2 i_2 + M i_1) = 0 \tag{2.133}$$

where it has been taken into account that the inductances can be time dependent due to the relative motion of the two coils. Multiplying the first equation with i_1 and the second one with i_2 leads further to

$$-v_1 i_1 + R_1 i_1^2 + \frac{dL_1}{dt} i_1^2 + L_1 \frac{di_1}{dt} i_1 + \frac{dM}{dt} i_2 i_1 + M \frac{di_2}{dt} i_1 = 0, \tag{2.134}$$

$$-v_2 i_2 + R_2 i_2^2 + \frac{dL_2}{dt} i_2^2 + L_2 \frac{di_2}{dt} i_2 + \frac{dM}{dt} i_1 i_2 + M \frac{di_1}{dt} i_2 = 0. \tag{2.135}$$

Adding the two equations and using (2.126), (2.128), (2.129) leads to

$$P_{mech} = \frac{1}{2} \frac{dL_1}{dt} i_1^2 + \frac{1}{2} \frac{dL_2}{dt} i_2^2 + \frac{dM}{dt} i_1 i_2, \tag{2.136}$$

and finally (2.127) can be rewritten as

$$\tau = \frac{1}{2} \left(\frac{dL_1}{d\alpha_{Rot}} i_1^2 + \frac{dL_2}{d\alpha_{Rot}} i_2^2 \right) + \frac{dM}{d\alpha_{Rot}} i_1 i_2. \tag{2.137}$$

Therefore, the generation of an electromechanical torque requires at least one inductance that depends on the rotor position. This leads further to the conclusion that any electromechanical energy conversion requires voltages induced due to motion.

Furthermore it is mentioned that the analysis of the power balance is the most common description of electrical machines. It is valid for all electrical machines and describes all effects that occur. The problem with this approach is the difficulty in determining the machine parameters (inductances, resistances and loss terms). All these parameters are functions of the machine currents and the rotor position. Furthermore, they also depend on continuum phenomena like eddy currents, hysteresis and so on. Therefore, this approach is not generally applicable.

However, under the assumption that most continuum phenomena are negligible, only a finite number of state variables is sufficient to describe the machine behavior. Thus,

the infinite dimensional parameter space collapses to a low-dimensional one. This finally allows a very general classification of electrical machines only depending on the number of required state variables. This classification is used for the finite element based circuit machine model approach as shown in chapter 4.

Although the focus of this subsection was on rotating machines, most statements can be applied to linear motors or inductive actuators too.

3 MODELING ELECTRICAL MACHINES

Many different model approaches for electrical machines can be found in literature. However, most of these model approaches can be classified into:

- Analytical models
- Magnetic equivalent circuit models
- Numerical models

In this context, analytical models are models that reduce the electrical machine to its air gap. Thus, any iron is assumed to be infinitely permeable and non-conductive. Analytical functions are used to describe the slotting and the electric loading of the windings. Mathematical superposition, for instance using Fourier decomposition, is often utilized. Thus linearity is assumed, that is only approximately fulfilled in steady state. Nevertheless, analytical models are very fast to evaluate and cover harmonic effects. Furthermore, the interplay of the system parameters and their effect to the operation can be distinguished. This allows a deep insight in the behavior of electrical machines. Therefore, these model approaches are well suited for design, optimization and control tasks. Fundamental wave models (FWM) are the most elementary representatives. Further, field harmonics approach (FHA) and winding functions approach (WFA) belong to this class of models.

Magnetic equivalent circuit (MEC) models describe the magnetic circuit of an electrical machine with a lumped network. Thus, the iron in the machine is considered. These models can be evaluated very fast and nonlinearity can be considered with nonlinear element equations or characteristic curves. However, the parameterization of these models requires detailed knowledge of the machine design and could become very extensive. Nevertheless, these models are well suited for design and optimization tasks.

Numerical models utilize discretization methods as finite element, finite volume or finite difference method for solving the electromagnetic field equations. A detailed knowledge of the machine design is required and the modeling effort is typically high. Furthermore, these models are computationally very demanding, but the coverage of effects caused by slotting, saturation or eddy currents is very high. Therefore, this approach can be used for local design optimization or problem analysis. Furthermore, this approach can be used for determining machine parameters for other model approaches.

In the next subsections a brief introduction into the commonly used model approaches is given.

3.1 Fundamental wave model approach (FWMA)

This well-known model approach assumes several simplifications as sketched for a permanent magnet synchronous machine in Fig. 3.1. A detailed description of all assumptions and derivations for various machine types can be found in literature, for instance in [68], [7], [90] or [17]. Within this section only a brief summary shall be presented.

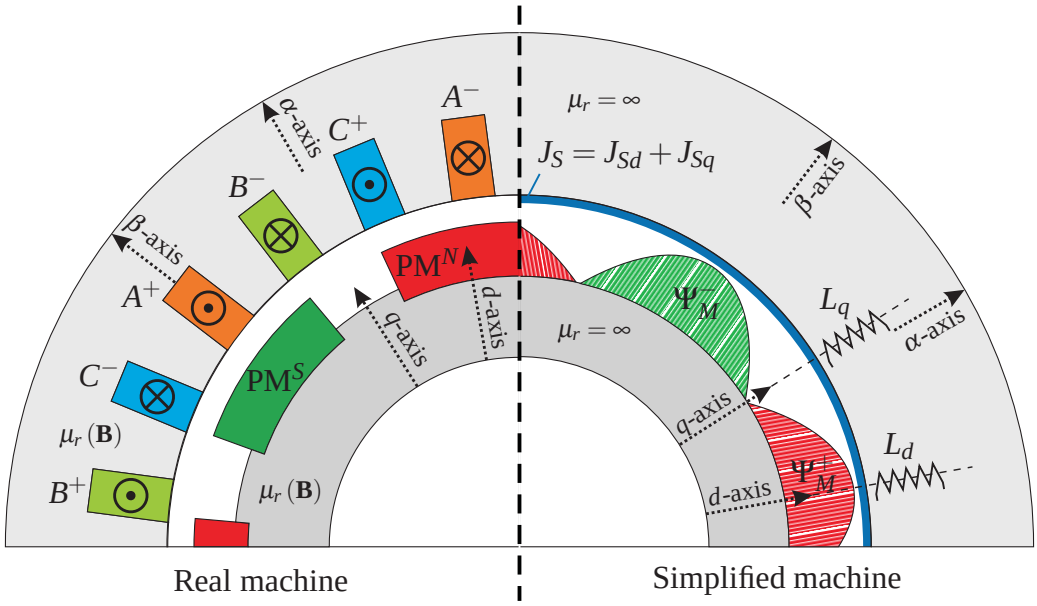

Figure 3.1: Comparison between a real machine (left) and the simplified machine for the fundamental wave model approach (right). The real machine consists of slots, a 3-phase coil system (*ABC*) located in these slots resulting in a discrete distributed electric loading in circumferential direction, specially shaped permanent magnets (PM) with a defined pole covering factor and ferromagnetic material with a nonlinear permeability $\mu_r = f(\mathbf{B})$. The simplified machine is characterized by a homogenized geometry without any slots and infinite permeable material for rotor and stator. The distributed three-phase coil system on the stator is replaced by an equivalent two-phase coil system in the rotor related dq-reference system (electrically orthogonal). The resulting coil system is characterized by the inductances for the d-direction L_d and for the q-direction L_q. The magnets are replaced by the main flux linkage Ψ_M. This quantity describes the magnetic flux that interacts with the surface current density J_S (electric loading) in the air gap. All quantities in the air gap are assumed to be sinusoidally distributed in circumferential direction.

This model approach replaces the complete machine by its air gap and considers only the fundamental wave in circumferential direction of the spatial electric loading wave and spatial flux waves assumed in the air gap [7]. The fundamental wave in this context is

related to a full electrical period, i.e. a magnetic pole pair. The spatial wave for the electric loading is further decomposed into its corresponding components in a freely chosen orthogonal reference system (e.g. stator related $\alpha\beta$-system, rotor related dq-system). For both components of this two-phase system corresponding inductances (e.g. L_d and L_q) are introduced. Further, all quantities of the three-phase system are transformed into this system. For example, the voltage equations for a PMSM ([78]) can be written as

$$v_d = R_{Cu} i_d + L_d \frac{di_d}{dt} - \omega_{el} L_q i_q, \tag{3.1}$$

$$v_q = R_{Cu} i_q + L_q \frac{di_q}{dt} + \omega_{el} \left(L_d i_d + \Psi_M \right), \tag{3.2}$$

with the voltage v_d and current i_d in direct direction, the voltage v_q and current i_q in quadrature direction, the stator copper resistance R_{Cu} and the electrical machine speed ω_{el}. The machine torque τ can be written as

$$\tau = \frac{3}{2} n_{mp} \left[\Psi_M i_q + \left(L_d - L_q \right) i_d i_q \right], \tag{3.3}$$

with the number of magnetic pole pairs n_{mp}, as shown in [78].

The stator related $\alpha\beta$-reference system and the rotor related dq-reference system are the mostly used reference systems. Both system are geometrically orthogonal with respect to an electrical period. The $\alpha\beta$-system is orientated with the magnetic axis of the coil of phase *A*, the dq-system is orientated with the axis of the magnetic north pole of the rotor, as shown in Fig. 3.1. For the transformation of the three phase *ABC*-system into the $\alpha\beta 0$-system the Clarke transformation described by the matrix $\mathbf{C}$ is used, e.g. for the machine currents:

$$\mathbf{i}_{\alpha\beta 0} = \mathbf{C} \mathbf{i}_{ABC}. \tag{3.4}$$

Under the assumption that the magnetic axis of phase *A* coincides with the α-direction (as shown in Fig. 3.1) this linear transformation is defined as

$$\mathbf{C} = \begin{bmatrix} \cos 0 & \cos\frac{2\pi}{3} & \cos\frac{4\pi}{3} \\ \sin 0 & \sin\frac{2\pi}{3} & \sin\frac{4\pi}{3} \\ \frac{1}{3} & \frac{1}{3} & \frac{1}{3} \end{bmatrix} = \begin{bmatrix} 1 & -\frac{1}{2} & -\frac{1}{2} \\ 0 & \frac{\sqrt{3}}{2} & -\frac{\sqrt{3}}{2} \\ \frac{1}{3} & \frac{1}{3} & \frac{1}{3} \end{bmatrix}, \tag{3.5}$$

and its inverse is

$$\mathbf{C}^{-1} = \begin{bmatrix} \frac{2}{3} & 0 & 1 \\ -\frac{1}{3} & \frac{1}{\sqrt{3}} & 1 \\ -\frac{1}{3} & -\frac{1}{\sqrt{3}} & 1 \end{bmatrix}. \tag{3.6}$$

Several versions of this transform with various scale factors can be found in literature, e.g.:

$$\mathbf{C} = \begin{bmatrix} \frac{2}{3} & -\frac{1}{3} & -\frac{1}{3} \\ 0 & \frac{1}{\sqrt{3}} & -\frac{1}{\sqrt{3}} \\ \frac{1}{3} & \frac{1}{3} & \frac{1}{3} \end{bmatrix}, \; \mathbf{C}^{-1} = \begin{bmatrix} 1 & 0 & 1 \\ -\frac{1}{2} & \frac{\sqrt{3}}{2} & 1 \\ -\frac{1}{2} & -\frac{\sqrt{3}}{2} & 1 \end{bmatrix}, \tag{3.7}$$

for preserving the amplitude. For a balanced three phase system the 0-component vanishes, thus the transformation can be simplified:

$$\mathbf{C} = \begin{bmatrix} \cos 0 & \cos 120 & \cos 240 \\ \sin 0 & \sin 120 & \sin 240 \end{bmatrix} = \begin{bmatrix} 1 & -\frac{1}{2} & -\frac{1}{2} \\ 0 & \frac{\sqrt{3}}{2} & -\frac{\sqrt{3}}{2} \end{bmatrix}, \; \mathbf{C}^{-1} := \begin{bmatrix} \frac{2}{3} & 0 \\ -\frac{1}{3} & \frac{1}{\sqrt{3}} \\ -\frac{1}{3} & -\frac{1}{\sqrt{3}} \end{bmatrix}. \tag{3.8}$$

The $\alpha\beta 0$-system (or $\alpha\beta$-system) can be further transformed into the rotor related $dq0$-system (or dq-system). This system has the advantage for synchronous machines that all alternating quantities of the stator become direct quantities in this reference system. For this purpose the Park transformation $\mathbf{P}(\alpha_{Rot})$ is used. From a mathematical point of view this transformation is a rotational transformation for the α and β components. It is defined as

$$\mathbf{P}(\alpha_{Rot}) = \begin{bmatrix} \cos\alpha_{Rot} & \sin\alpha_{Rot} & 0 \\ -\sin\alpha_{Rot} & \cos\alpha_{Rot} & 0 \\ 0 & 0 & 1 \end{bmatrix} \tag{3.9}$$

with the rotor position α_{Rot} in electrical degrees. The inverse transformation is defined as

$$\mathbf{P}(\alpha_{Rot})^{-1} = \mathbf{P}(-\alpha_{Rot}), \tag{3.10}$$

and is similar to a counter clock wise rotation. Note, the Park transformation is additive:

$$\mathbf{P}(\alpha_{Rot} + \beta_{Rot}) = \mathbf{P}(\alpha_{Rot})\,\mathbf{P}(\beta_{Rot}). \tag{3.11}$$

3.2 Field harmonics approach (FHA)

The field harmonics approach substitutes the complete machine by its air gap (or a notionally increased air gap for taking the effects of slotting or saturation into account). Further, analytical functions are used for describing the current loading distribution $J_S(\varphi,t)$ and the permeance of the air gap $\Lambda(\varphi,t)$ in circmferential direction. These functions are decomposed into spatial waves using a Fourier analysis. The interplay of these spatial waves leads to magnetic fields in the air gap. These fields can be further classified by their cause [84] and a detailed analysis of harmonics in the magnetic field can be carried out (e.g. [70], [72]). This approach is widely used for loss determinations (e.g. [71], [73]) or noise and vibration (NVH) investigations of induction machines (e.g. [42]). The FHA can be also applied to permanent magnet synchronous machines (e.g. [100], [97], [98], [99]) and used for optimizing the magnet shape or minimizing cogging torque ([96], [101]).

For example, the electric loading J_S as shown in Fig. 3.2 can be assumed as a Fourier series

$$J_S(\varphi,t) = \sum_{\nu} J_{S,\nu} \cos(\nu\varphi - \omega t - \phi) \tag{3.12}$$

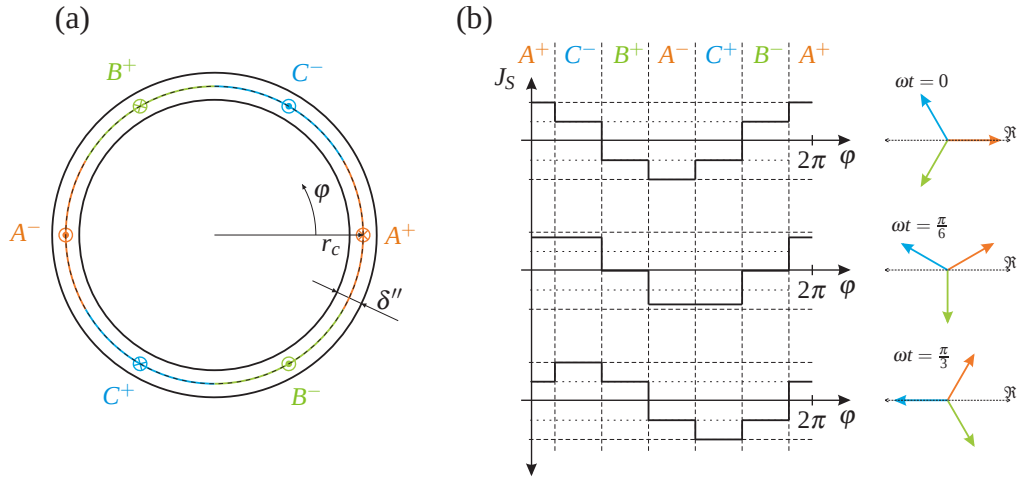

Figure 3.2: Field harmonics approach: (a) Overview of a machine with one magnetic pole pair and a winding with six sectors. An infinite number of slots are assumed. Thus the electric loading J_S for each winding sector is constant. Rotor and stator iron is assumed to be infinite-permeable, slotting and saturation effects are considered by a notional increased air gap δ''. (b) Diagrams for electric loading J_S at different times.

with the spatial ordinal number ν. For integer-slot windings only odd ordinal numbers can occur. Furthermore, any ν that is divisible by three cannot occur in three-phase systems. Therefore, all occurring ν can be written using

$$\nu = n_{mp}(1+6g) \quad \text{with} \quad g = 0, \pm 1, \pm 2, \pm 3, \ldots \tag{3.13}$$

where negative values represent spatial waves that move in mathematical negative (clockwise) direction along the air gap in circumferential direction. The corresponding MMF distribution $\Theta(\varphi,t)$ can be calculated using (3.12) as

$$\Theta(\varphi,t) = r_c \int J_S(\varphi,t)\,d\varphi \tag{3.14}$$

with the radius of the air gap r_c. This ansatz requires infinitely permeable iron for rotor and stator, thus any MMF drop in the iron has to be considered by a notionally increased air gap δ''. The resulting radial magnetic field density in the air gap $B(\varphi,t)$ can be determined by multiplication of $\Theta(\varphi,t)$ with the permeance of the air gap in radial direction $\Lambda(\varphi,t)$

$$B(\varphi,t) = \Lambda(\varphi,t)\Theta(\varphi,t). \tag{3.15}$$

The permeance function $\Lambda(\varphi,t)$ is used for taking slotting and saturation effects into account. For that purpose a spatial Fourier transformation of the permeance function is done leading to

$$\Lambda(\varphi,t) = \frac{\mu_0}{\delta(\varphi,t)} = \Lambda_0 + \sum_{\lambda} \Lambda_\lambda \sin(\lambda\varphi - \omega_\lambda t - \phi_\lambda) \quad \text{with} \quad \Lambda_0 = \frac{\mu_0}{\delta''} \tag{3.16}$$

with Λ_0 representing the permeance of the notionally increased air gap and the spatial ordinal number λ for the permeance waves caused by slotting and saturation.

3.3 Winding function approach (WFA)

The winding function approach replaces the complete machine by its air gap (or a notionally increased air gap for taking the effects of slotting or saturation into account) in the same manner as the FHA. However, the WFA describes the coupling of the windings by analytical functions, as shown in [21]. A winding in that sense is defined as all N loops that share the same two slots. Further, it is assumed that all windings are located in the center of the air gap and its copper cross section is negligible. Thus the electric loading can be modelled by two Dirac delta functions, as shown in Fig. 3.3.

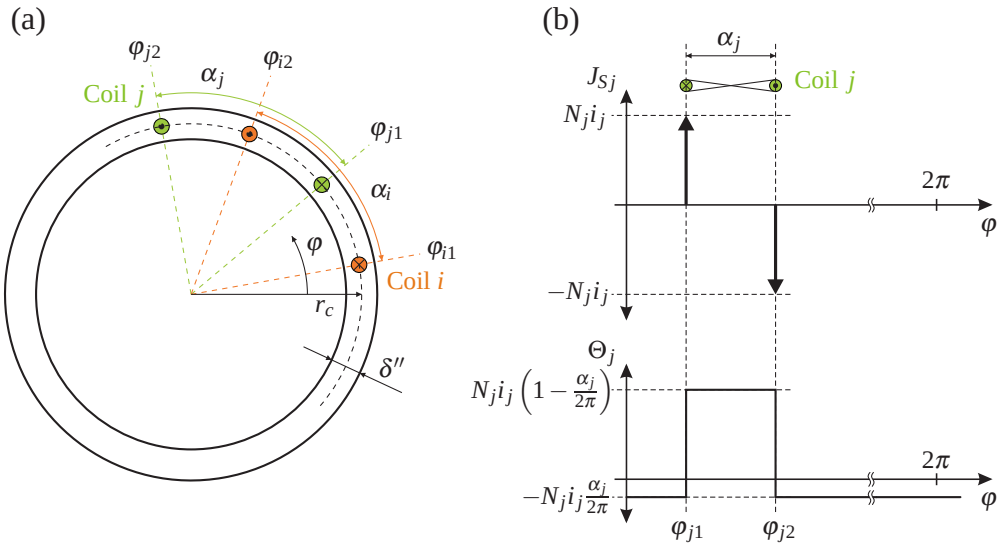

Figure 3.3: Winding function approach: (a) Overview of two coupled coils. Both coils are assumed to be located in the center of the air gap (with the radius r_c) with vanishing copper cross section. Rotor and stator iron is assumed to be infinitely permeable, slotting and saturation effects are considered by a notionally increased air gap δ''. (b) Diagrams for electric loading J_S (top) and magnetomotive force Θ over the air gap (bottom) for the j^{th}-coil.

Each winding is defined by its winding distribution function $w = f(\varphi)$ and its normalized MMF distribution function $W = f(\varphi)$. In the simplest case, these functions can be written for the j^{th}-coil as

$$w_j(\varphi) = \begin{cases} 1 & \text{if } \varphi_{j1} \leq \varphi \leq \varphi_{j2}, \\ 0 & \text{otherwise,} \end{cases} \tag{3.17}$$

with the starting angle φ_{j1} and the ending angle φ_{j2} of the j^{th}-coil and

$$W_j(\varphi) = \begin{cases} 1 - \frac{\alpha_j}{2\pi} & \text{if } \varphi_{j1} \leq \varphi \leq \varphi_{j2}, \\ -\frac{\alpha_j}{2\pi} & \text{otherwise,} \end{cases} \tag{3.18}$$

with the angular coil width α_j, as shown in Fig. 3.3.a. Using (3.18), the MMF distribution $\Theta_j(\varphi)$ for the j^{th} coil in circumferential direction can be written as

$$\Theta_j(\varphi) = N_j i_j W_j(\varphi) \tag{3.19}$$

with the number of windings N_j and the current i_j of the j^{th} coil, as shown in Fig. 3.3.b. Thus, the flux density distribution in the air gap $B_j(\varphi)$ can be written as

$$B_j(\varphi) = \frac{\mu_0}{\delta''}\Theta_j(\varphi) = \frac{\mu_0}{\delta''} N_j i_j W_j(\varphi) \tag{3.20}$$

with the notional increased air gap length δ''. The magnetic flux $\Psi_{i,j}$ that is linked with the i^{th}-coil can be written as

$$\Psi_{i,j} = N_i r_c l_{Fe} \int_{\varphi_{i,1}}^{\varphi_{i,2}} B_j d\varphi = N_i N_j i_j \frac{\mu_0 r_c l_{Fe}}{\delta''} \int_0^{2\pi} w_i W_j d\varphi \tag{3.21}$$

with the effective iron length l_{Fe} and the radius of the air gap r_c. Finally, the resulting mutual inductance $M_{i,j}$ can be written as

$$M_{i,j} = \frac{\Psi_{i,j}}{i_j} = N_i N_j \frac{\mu_0 r_c l_{Fe}}{\delta''} \int_0^{2\pi} w_i W_j d\varphi. \tag{3.22}$$

By taking the connection of all windings, the coil resistances and leakage inductances into account, the voltage equations for the machine can be written, as shown in [21]. This approach can be extended using modified functions for $w(\varphi)$ and $W(\varphi)$. For instance, the linear increase of the electric loading in the slot opening can be modeled in that way [25] or [28]. Furthermore, saturation effects can be considered by a modulated air gap $\delta'' = f(\varphi)$, leading for (3.22) to

$$M_{i,j} = \frac{\Psi_{i,j}}{i_j} = N_i N_j \mu_0 r_c l_{Fe} \int_0^{2\pi} \frac{w_i \tilde{W}_j}{\delta''} d\varphi. \tag{3.23}$$

Additional constraints are required in this case to ensure the solenoidality of the magnetic field. A modified normalized MMF distribution $\tilde{W}(\varphi)$ is required too, leading to the modified winding function approach (MWFA), as described in [2], [35] or [31]. The torque calculation can be done using the magnetic co-energy as presented in [34].

3.4 Magnetic equivalent circuit (MEC) approach

The circuit theory for electrical circuits described in subsection 2.1.1 can be also applied to magnetic circuits as presented e.g. in [11]. This approach is motivated by a segmentation of the magnetic problem domain into flux tubes, see e.g. [75], [90]. Each flux tube can be modeled by an equivalent circuit in form of a loop with magnetic resistances and sources. These loops can be finally merged and simplified using techniques of circuit theory. This

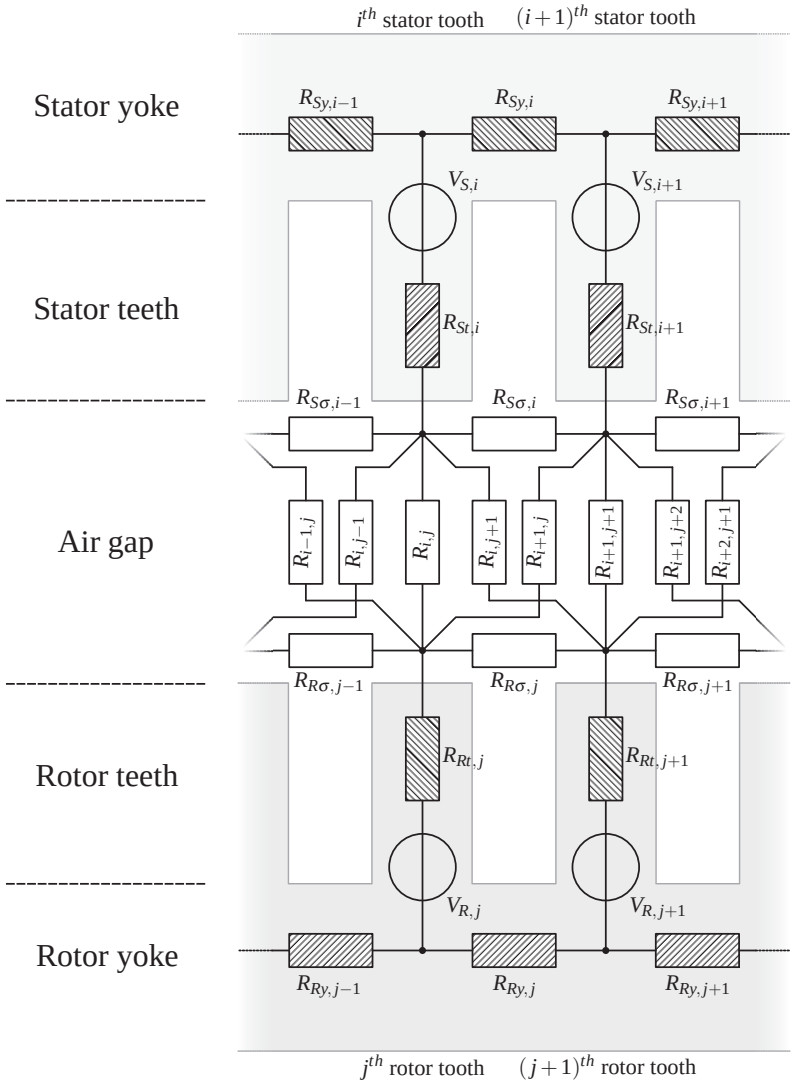

Figure 3.4: Detail of the magnetic equivalent circuit of an asynchronous machine (Source: [75]). All shaded resistors have a nonlinear behavior. The connection between rotor and stator as well as the resistances of all coupling elements are dependent on rotor position.

leads to a magnetic equivalent circuit for the magnetic problem domain. A detail of an MEC model of a machine is shown in Fig. 3.4. The magnetic flux through each element is assumed to be homogeneous and unidirectional, e.g.[75]. Thus, this method can be seen as a very coarse 1D finite element method approach.

Similar to electrical circuits, this approach can be used for transient as well as harmonic simulations. However, all magnetic resistors representing flux paths in ferromagnetic materials have a strong nonlinear behavior. Therefore, any harmonic simulations can be done only for a predefined operating point (i.e. small signal analysis). Furthermore, all parasitic flux paths over air have to be taken into account because they are mainly responsible for the stray flux and thus influence the behavior of the electrical machine.

Modeling electrical machines using the MEC approach is a well-known technique that is still used as seen in [76],[47],[87],[15]. Motion is considered by changing the circuit interconnection of the air gap elements. Eddy current effects can be taken into account [12] as well as iron and magnet losses calculated [88]. Furthermore, many approaches about modelling skewing or eccentricity can be found in literature, e.g. [75], [37], [94].

However, the model creation of a machine requires detailed information of its design and parameterization of the MEC is typically very costly. Analytical calculations or the finite element method is used for that purpose.

3.5 Finite element models

These models utilize the finite element method to solve the electromagnetic field equations within electrical machines. For this purpose, a detailed knowledge of the machine design is required. This includes appropriate material models for the used materials, too. Thus, a very high coverage of effects caused by saturation, slot harmonics, eddy currents or losses can be achieved. Furthermore, a deep view inside the electrical machine becomes possible. This allows local optimization of the machine design. However, the simulation cost for such models is typically very high compared with analytical model approaches. In this section several issues and hints for modeling electrical machines with FEM are presented. These are:

- Comparison between 2D and 3D models
- Utilization of symmetry planes
- Consideration of motion
- Initialization of transient simulations
- Interconnection of coils and voltage sources
- Force and torque determination
- Flux determination

Many of those issues mainly depend on the available features of the FEM-software package used. Within this work *ANSYS 14.5* was mainly employed. Therefore, this subsection relates to this software package. Further information about *ANSYS 14.5*, the suggested methods and used commands can be found in the *ANSYS 14.5* manual [4].

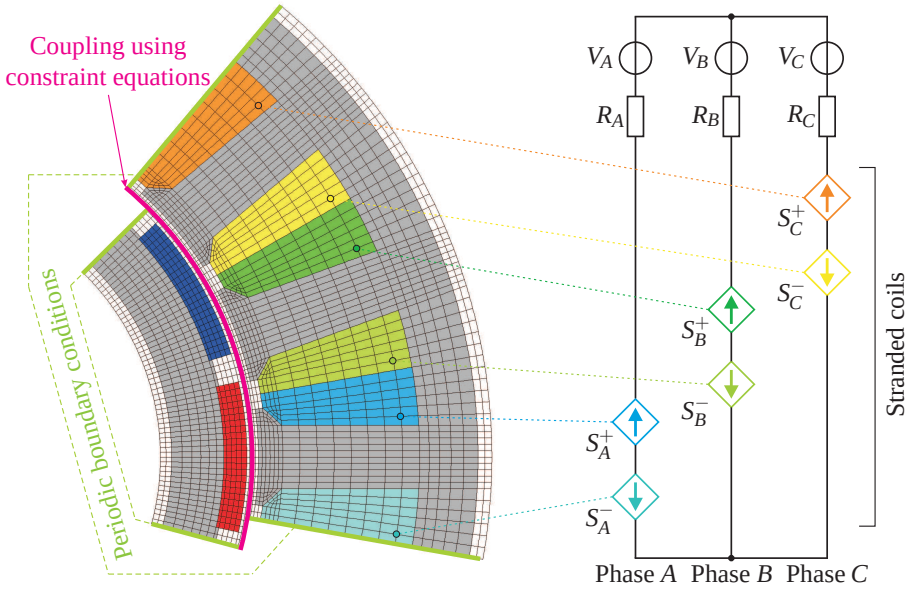

Figure 3.5: 2D FE model of a permanent magnet synchronous machine. This model uses circuit elements for connecting the machine coils and voltage sources. The symmetry planes of the machine are utilized to minimize the model size. Periodic boundary conditions (green) are used for coupling the resulting cutting planes. The sliding interface (magenta) allows a movement between rotor and stator.

3.5.1 Comparison between 2D models and 3D models

The most important difference between 2D models and 3D models is the model size. 2D FEM models are typically small problems, i.e. the number of finite elements and thus the number of degrees of freedoms (DOFs) is much smaller than for 3D models. This leads to a much smaller simulation cost for 2D models (typically in the range of seconds to minutes) than for 3D models (typically in the range of hours to days or weeks). Furthermore, the use of 3D models comes along with a much higher modeling effort.

Due to the fact that many electrical machine topologies can be assumed to be homogeneous in the axial direction, 2D models are sufficient for many simulation tasks during the design phase of electrical machines. Even slight changes in axial direction (e.g. caused by skewing of the rotor or rotor eccentricity) can be approximated by 2D models. For this purpose, the 2D FE multi-slice technique is available, as described in e.g. [77] [92], [20], [27] and [65].

However, the consideration of end winding effects or eddy currents in conducting machine parts (e.g. permanent magnets, press fingers, housing, ...) usually necessitate 3D models.

The choice of the FE model to be used mainly depends on the effects that should be covered by the simulation. Due to the lower modeling effort and the smaller computation effort, 2D models should be preferred if applicable. Note that the model depth should always be kept as high as necessary but as low as possible.

3.5.2 Utilization of symmetry planes

To accomplish short simulation times, the FE model should have as few finite elements as possible. For this purpose, symmetry planes in the machine can be utilized. For machines with a number of magnetic pole pairs $n_{mp} > 1$, modeling of only one magnetic pole pair is in many cases sufficient. However, modeling of such a machine segment requires a periodic boundary condition at the cutting planes. This can be realized by coupling the corresponding nodes or edges of the cutting planes. Many FEM tools provide such a periodic boundary condition. In *ANSYS 14.5* the *CP*-command (see [4]) can be used for that purpose, as shown in Fig. 3.5.

Modeling of only one magnetic pole would be sufficient, too, but then an anti-periodic boundary condition is required. The consideration of the reversed magnetic flux condition between the cutting planes could be realized by constraint equations. In *ANSYS 14.5* the *CE*-command can be used for this purpose.

3.5.3 Consideration of motion

For magnetostatic or harmonic simulations no movement between rotor and stator is required. Thus, rotor and stator can be simply meshed as one connected problem domain. In contrast, transient simulations require a relative movement between rotor and stator. Therefore, rotor and stator need to be meshed as two separate problem domains leading to two disconnected components. Therefore, an additional interface between these components is required.

The simplest approach for such an interface is using the same, uniformly distributed mesh for the surfaces of both components. Thus, the mesh on both sides of the interface is identical even if one of the components is rotated through an angle that corresponds to a multiple of the mesh size in circumferential direction. This *clicking-mesh*-approach allows a direct coupling of nodes or edges without any interpolation. However, additional requirements for the mesh lead to a higher modeling effort (e.g. an additional layer in the air gap is typically used to make the mesh uniformly distributed). Furthermore, only discrete angles for the rotation are possible and thus a variable time step size depending on the rotational speed is required. Both constraints limit the practicability of this method. Nevertheless, no interpolation is required and thus no interpolation error occurs. In *ANSYS 14.5* the *CE*-command (see [4]) can be used for this coupling technique. The *CP*-command

would not work in this case, because the nodal coupling needs to be changed in every time step.

Another approach that gets along without any interpolation is the *moving-band*-technique. This method re-meshes a defined region (the moving band) between the components in every time step of the simulation. Therefore, an arbitrarily movement without any interpolation could be achieved. However, all elements of the moving band must be re-created in every time step. Therefore, the system matrix of the FE model needs to be re-assembled in every time step slowing down the simulation. Additionally, an appropriate software design for handling the changing node and element numbers of the moving band is required. Furthermore, it has been shown in [13] that spatial harmonics caused by the changing aspect ratio of the elements occur. The effect of this numerical error can be only minimized by increasing the number of the finite elements in circumferential direction. *ANSYS 14.5* does not provide any built-in macro for supporting the *moving-band*-technique for transient electromagnetic simulations.

If a uniform mesh density is not applicable or an arbitrary movement between rotor and stator is required, the field quantities at the interface need to be interpolated. For scalar field quantities this approach is straight forward as shown below. However, any interpolation of vectorial DOFs has to fulfill the properties of the vector field quantity specified by its curl and divergence. For edge elements this becomes even more complex because the corresponding DOFs are integral values of the vector field quantity evaluated along the edge as shown in [26]. However, coupling of vectorial quantities is still object of current research activities, as illustrated in [3], [5], [79].

The coupling of scalar fields could be achieved by constraint equations. In this sense, one side of the interface is called the master and the other the slave. The constraints describe a calculation rule between the DOFs of the slave nodes and the DOFs of the master nodes. Polynomials, shape or expansion functions of the FE or more complex functions can be used for the interpolation. This is typically achieved by the use of special interface elements, for example contact or mortar elements. In *ANSYS 14.5 contact*- and *target*-elements can be used for this purpose, see [4]. However, mesh related harmonics in the air gap field caused by interpolation errors could occur. Therefore, a sufficient mesh density for the chosen interpolation method is required. Furthermore, it is suggested to locate the interface in the center of the air gap. Additionally, a layer of at least two air elements on both sides of the interface should be modeled. However, a generally valid criterion could not be given. To ensure the proper function of the coupling interface, an investigation of the resulting field quantities in the air gap is required.

For a linear interpolation the *CE*-command can be used in *ANSYS 14.5*. This method is illustrated in Fig. 3.5. Furthermore, *ANSYS 14.5* provides the macro *CEINTF* (see [4]) that performs this coupling for the nodes of a selected interface automatically. Note that the *CE*-command models movement only by coupling nodes. Thus, a real movement of the components is not necessary and neither rotor nor stator needs to be rotated.

3.5.4 Initialization of transient simulations

An important issue of transient simulations is the initialization of the model. The transient effect after the start up could need many simulation steps to accomplish the steady state. This behavior is mainly influenced by the time constants of the system. Thus, the simulation time is increased needlessly. However, using the correct initial values for the field quantities will prevent any transient effects after start up. If the steady state currents of the machine are known, a magnetostatic simulation in advance can be carried out to initialize the transient simulation. However, eddy current effects cannot be considered by this approach. In such a case, a harmonic simulation could be carried out. This approach leads to a good initial guess for the field quantities and further to a marked decrease of simulation steps during start up, as described in [86].

3.5.5 Interconnection of coils and coupling with circuits

The interconnection of different coils and the coupling with circuit elements is another important issue for transient simulations of electrical machines. In *ANSYS 14.5* several circuit elements are available for this purpose. The *CIRCU124*-elements allow the coupling of stranded coils or massive conductors with other circuit elements. Furthermore, resistors and independent as well as controlled voltage and current sources are available, see [4] for more details. A circuit coupled FE model is shown in Fig. 3.5.

3.5.6 Force and torque determination

The methods used for force and torque calculation are the method of virtual displacement and the Maxwell stress tensor as presented in subsection 2.1.3. The method of virtual displacement allows the determination of the force and torque acting on a component. This is done by determining the gradient of the magnetic co-energy of the component. It is known that electromagnetic FEM simulations calculate the magnetic energy in the problem domain very exactly even if the local solution is not exact. This is caused by the fact that the functional that is minimized for the solution corresponds to the magnetic energy. Thus, the method of virtual displacement leads to good results even at coarser meshes.

For the Maxwell stress tensor, the surface integral (2.55) need to be evaluated. This requires a very exact local solution of the field quantities on the integral's surface. Therefore, the Maxwell stress tensor requires a finer mesh than the method of virtual displacement does. Furthermore, the component's surface should be smooth because high numerical errors could occur at corners and edges of the surface. However, the Maxwell stress tensor allows an evaluation of the mechanical stress density. Thus, local forces (e.g. force acting on a single stator tooth) can be calculated, as shown in [91]. This is an advantage compared to the method of virtual displacement.

The force and torque calculation in *ANSYS 14.5* is done in the post processing stage. Therefore, so called *Force Flags* must be set on the surface of the component during the

modeling stage. The built-in macro *FMAGBC* can be used for this purpose. The evaluation of the force and torque can be done with the macros *FMAGSUM* and *TORQSUM*. These macros use both of the above described methods for the evaluation of force and torque, see [4]. Thus, a direct comparison between these methods can be done. In this context, a bad agreement typically indicates a too coarse mesh in the air gap region. Note that the *TORQSUM* macro can be only used for 2D models.

3.5.7 Flux linkage and inductance determination

For determining flux linkages and inductances of electrical machines, FEM simulations are widely used. In this subsection the equations used for this purpose are summarized. The focus is on FEM tools using the $\mathbf{A},V$-$\mathbf{A}$-formulation because almost all commercial 2D FEM tools use this or a modified version of this formulation.

The magnetic flux Φ through any surface $\mathbf{S}$ can be calculated with the magnetic vector potential $\mathbf{A}$ as

$$\Phi = \iint_{\mathbf{S}} \mathbf{B} \cdot d\mathbf{s} = \iint_{\mathbf{S}} (\nabla \times \mathbf{A}) \cdot d\mathbf{s} = \oint_{\partial \mathbf{S}} \mathbf{A} \cdot d\mathbf{l}, \tag{3.24}$$

using Stokes' theorem (2.22). Note that (3.24) assumes a well-defined boundary for the surface $\mathbf{S}$. For real coils with a conducting cross section $\Gamma > 0$, both the coil's surface and its contour $\partial\mathbf{S}$ are ambiguous. However, a generally valid equation for determining the flux that is linked with any coil could be derived from (3.24). For this purpose, the whole conductive domain of a coil is divided in N sub-coils. Thus, the whole coil can be assumed as circuit of parallel connected sub-coils. The k^{th} sub-coil is defined by the current i_k

$$i_k = \iint_{\Gamma_k} \mathbf{J} \cdot d\mathbf{s} \tag{3.25}$$

constant along the sub-coils contour $\partial\mathbf{S}_k$. Note that this sectioning leads in general to a conducting cross section Γ_k that is not constant along $\partial\mathbf{S}_k$. However, the volume of the whole conductive domain of the coil is not changed by this sectioning

$$\iiint_{\Omega} dV \equiv \sum_{k=1}^{N} \iiint_{\Omega_k} dV. \tag{3.26}$$

This construction leads for $N \to \infty$ to a vanishing Γ_k. Thus, (3.24) can be used for calculating Φ_k of each sub-coil. Considering that Φ_k is linked only with the ${}^{i_k}/_{i_{tot}}$ -th part of the total current i_{tot}, the flux linkage Ψ of the whole coil can be determined by summing up all Φ_k weighted with the corresponding fractional amount of the coil current. This leads to

$$\begin{aligned}\Psi &= \lim_{N\to\infty} \sum_{k=1}^{N} \frac{i_k}{i_{tot}} \oint_{\partial \mathbf{S}_k} \mathbf{A} \cdot d\mathbf{l} = \frac{1}{i_{tot}} \lim_{N\to\infty} \sum_{k=1}^{N} \oint_{\partial \mathbf{S}_k} i_k \mathbf{A} \cdot d\mathbf{l} = \frac{1}{i_{tot}} \lim_{N\to\infty} \sum_{k=1}^{N} \oint_{\partial \mathbf{S}_k} \left(\iint_{\Gamma_k} \mathbf{J} \cdot d\mathbf{s} \right) \mathbf{A} \cdot d\mathbf{l} \\ &= \frac{1}{i_{tot}} \lim_{N\to\infty} \sum_{k=1}^{N} \oint_{\partial \mathbf{S}_k} \iint_{\Gamma_k} (\mathbf{J} \cdot \mathbf{A})\, d\mathbf{s} \cdot d\mathbf{l} = \frac{1}{i_{tot}} \lim_{N\to\infty} \sum_{k=1}^{N} \iiint_{\Omega_k} \mathbf{J} \cdot \mathbf{A} dV = \frac{1}{i_{tot}} \iiint_{\Omega} \mathbf{J} \cdot \mathbf{A} dV,\end{aligned} \tag{3.27}$$

as detailed in [45].

In the 2D case, (3.27) needs to be adapted. Only the z-components of $\mathbf{A}$ and $\mathbf{J}$ need to be considered and the conductor cross section in z-direction is constant. The contour has to be split into the positive coil side (Γ^+, current flow in $+z$-direction) and negative coil side (Γ^-, current flow in $-z$-direction). This becomes necessary, because in (3.27) $d\mathbf{s}$ has the same direction as the current flow whereas in 2D case $d\mathbf{s}$ is $+z$-directed. Finally, the integration along the contour is simplified to a multiplication with the length l_z and the number of turns N_C. This leads to

$$\begin{aligned}\Psi &= \frac{1}{i_{tot}} \lim_{N\to\infty} \sum_{i=1}^{N} \oint_{\partial \mathbf{S}_i} \iint_{\Gamma_i} (\mathbf{J}\cdot\mathbf{A})\, d\mathbf{s}\cdot d\mathbf{l} = \frac{1}{i_{tot}} \lim_{N\to\infty} \sum_{i=1}^{N} N_C l_z \left(\iint_{\Gamma_i^+} J_z A_z d\mathbf{s} - \iint_{\Gamma_i^-} J_z A_z d\mathbf{s} \right) \\ &= N_C \frac{l_z}{i_{tot}} \left(\iint_{\Gamma^+} J_z A_z d\mathbf{s} - \iint_{\Gamma^-} J_z A_z d\mathbf{s} \right).\end{aligned} \tag{3.28}$$

For constant current densities J_z^+ and J_z^- within the corresponding conducting cross sections of the positive coil side Γ^+ and the negative coil side Γ^-, (3.28) can be simplified to

$$\Psi = N_C \frac{l_z}{i_{tot}} \left(J_z^+ \iint_{\Gamma^+} A_z d\mathbf{s} - J_z^- \iint_{\Gamma^-} A_z d\mathbf{s} \right) = N_C l_z \left(\frac{1}{\Gamma^+} \iint_{\Gamma^+} A_z d\mathbf{s} - \frac{1}{\Gamma^-} \iint_{\Gamma^-} A_z d\mathbf{s} \right), \tag{3.29}$$

using $\Gamma^+ = \frac{J_z^+}{i_{tot}}$ and $\Gamma^- = \frac{J_z^-}{i_{tot}}$.

The corresponding inductance of the coil can be determined by (2.6). In case of more than one coil an induction matrix including all self and mutual inductances needs to be determined. For linear materials this can be achieved by impressing a test current into one coil and determining the resulting fluxes in all coils. This procedure is repeated for every coil. Alternatively, the magnetic energy can be used to determine the inductances

$$L = \frac{2W_{mag}}{i^2}. \tag{3.30}$$

In the nonlinear case, this method needs to be adapted because the correct saturation state of the material needs to be considered. One method to achieve this can be found in [6]. In a first step, a nonlinear simulation with the actual coil currents has to be carried out. In a second step the actual permeability for every finite element needs to be determined. In a third step, these values are used as linear material parameters and the required linear simulations are carried out. Obviously, this method is very costly in terms of simulation time.

3.6 Finite element based model approach

The finite element based model approach combines the benefits of the circuit model approach (fast evaluation) and the finite element model approach (high coverage of effects

caused by e.g. slotting or saturation). This is achieved by describing the behavior of the elements of the circuit model by characteristic curves. The parameterization of these characteristic curves is done by several finite element simulations in advance. One approach for the implementation is to utilize magnetostatic FEM-simulations, as e.g. in [49]. Herewith, the characteristic curves become sampled by variation of the FE simulation input parameters like rotor position or machine currents. The sampled data are stored in look-up tables and are evaluated by a suitable interpolation technique. This implementation will be described in full length in the next chapter 4. Other implementations use time harmonic or transient FEM-simulations for this purpose, as shown e.g. in [9]. Many effects like cogging torque, slot harmonics and saturation but also rotor eccentricity can be covered by the FE-based model approach. Finally it should be mentioned that every change of the magnetic circuit or the coil design necessitates a new look-up table determination. Therefore, this approach is not suited for electromagnetic machine design purposes.

3.7 Conclusion

All discussed machine model approaches have several benefits but also disadvantages that limit their application. Thus, the model requirements for multibody dynamics simulations have to be defined first as already done in subsection 1.1.2. These requirements necessitate a model in the time domain that is fast to evaluate and covers torque ripple and saturation effects. However, these requirements can be fulfilled by almost all model approaches. Only the finite element models have to be excluded because of their high simulation costs.

However, there are also some additional requirements because the machine models should become part of a MBD-simulation tool. Therefore, all models must be generic. Furthermore, the focus of MBD simulations is on modeling whole systems. The electrical machine is only one part and it has to be assumed that the user of the MBD-tool is not familiar with electrical machines. Thus, all models must be easy to use and fast configurable. This is a first restriction because the configuration of a generic MEC or WFA model is difficult due to the high number of parameters and requires at least a basic electromagnetic knowledge. Furthermore, most of these parameters are more abstract and calculation rules have to be defined for their determination. Finally, it has to be considered that practically no manufacturer of electrical machines is willing to give design data of the machine to the customer. Such data are typically confidential because they would allow everyone to copy the machine. Thus, this is a restriction to all model approaches that require detailed knowledge of the electrical machine design.

Taking all these additional requirements into account leads to the conclusion that the finite element based circuit model approach is best suited for the application within a MBD-simulation. This model approach is easy to configure because only the correct set of look-up tables for the corresponding machine has to be selected. Furthermore, it is the only approach that is able to hide the whole machine design because the whole look-up table generation can be done by the manufacturer of the machine. Thus no geometric or material

specifications have to be made public. Depending on the chosen model implementation, as shown in chapter 4, the parameter calculation for the look-up tables can be done without defining new calculation methods.

4 FINITE ELEMENT BASED CIRCUIT MODELING

The conclusions of the last chapter show that the FE based circuit modeling approach is best suited for modeling electrical machines in multi-body dynamics simulations. Therefore, this approach is presented in more detail. It is based on characteristic curves stored in look-up tables. The whole information of the machine behavior is stored in these look-up tables. Thus, they are used to evaluate the quantities needed during the transient MBD simulation. Nevertheless, there are many implementation issues to be solved to get an applicable model. This chapter focuses mainly on rotating machines but almost all considerations are also valid for instance for linear motors or actuators like inductive valves.

The results of this chapter have been published in [60] and [64].

4.1 Parameter variables and look-up table quantities

The choice of the model parameter variables and the choice of the physical quantities stored in the look-up tables are the most important implementation decisions. These decisions mainly influence the preprocessing effort of the model approach, the memory demand for the look-up tables and the accuracy and convergence behavior of the transient simulation.

It has been shown in subsection 2.4.2 that for an electro-mechanical energy conversion at least one inductance has to depend on rotor position. Thus, the angular rotor position α_{Rot} can be identified as a necessary parameter. Due to symmetry reasons, it is sufficient to vary this variable only in an interval of $180^{\circ\mathrm{E}}$ (electrical degrees). In case of a symmetric three-phase design, this interval can be further reduced to $60^{\circ\mathrm{E}}$.

Additionally to the mechanical parameter, the electromagnetic state of the machine needs to be defined by parameter variables. For this purpose, the currents or flux linkages of the coils can be used in general. The use of currents leads to flux linkages (or inductances) stored in the look-up tables whereas the use of the flux linkages leads to currents (or inductances) stored in the look-up tables:

$$v = Ri + \frac{d\psi(i)}{dt} = Ri + \frac{dL(i)\,i}{dt} = Ri(\psi) + \frac{d\psi}{dt} = R\frac{\psi}{L(\psi)} + \frac{d\psi}{dt}. \tag{4.1}$$

In principle, the two approaches are equivalent. However, the use of currents has several advantages compared to that of using flux linkages:

- The look-up table generation during preprocessing becomes simpler. Using the flux linkages directly as input for a 2D-FE simulation can be achieved for one coil by presetting of the magnetic vector potential A_z (see subsection 3.5.7). However, this requires knowledge about the exact current density distribution within the copper cross

section of the coil. In case of more than one coil, the coupling between them has to be also known. Therefore, this approach is hardly applicable. Thus, coil currents have to be used as input for the magnetostatic FE simulations. This leads to characteristic curves for the flux linkages parameterized by the machine currents. For getting flux linkage parameter variables an inversion of these characteristic curves is required leading to a non-rectangular sampling grid. The storage scheme and the evaluation of the interpolation function for such data tables become more extensive.

- Impressing machine currents to the FE based machine model requires currents as parameter variables. Taking into account that the look-up tables store the whole machine behavior, the 2D FE multi-slice technique can be simply emulated by the FE based model approach. This extension of the FE based model approach is presented in chapter 6. However, impressing the machine currents is necessary for this approach.

- A variation of the machine length can be realized easier. This is for example required in the design stage of an electrical drive. By changing the machine length, the output power and torque of the machine can be scaled. During this scaling process the machine currents stay constant whereas the machine fluxes change. This can be easily realized for electric current parameters by a simple scaling of the flux linkages, inductances and torque. For flux linkage parameter variables the look-up table evaluation has to be modified. In case of pre-calculated interpolation parameters as suggested in section 4.3 even new look-up tables are required.

Furthermore, and independent of currents or flux linkages being used, any linear combination of them can be also used as parameter variables. This linear transformation also influences the look-up table generation process and its evaluation. For instance, the Clarke- and Park-transformation (described in section 3.1) can be used to transform a stator related three-phase system into a rotor related $dq0$-system. This leads to three advantages compared to the use of phase quantities:

- The saturation state of the machine becomes nearly independent of the rotor position. This can be utilized to design a more effective parameter variation algorithm during look-up table generation, as described in subsection 4.2.1.

- The components in the $dq0$-system do not change significantly in steady state. Thus, transient simulations can be carried out with larger time steps.

- In addition to the last item, it is not necessary to load the whole data table into memory. Only the segments for all rotor positions with the actual current state have to be loaded.

It is pointed out that the use of transformed parameter variables has no influence on the ability of the FE based model approach to take account of saturation as well as of the non-sinusoidal variation of the variables both in space and time. Contrary to fundamental wave

models, no additional simplifications are required or assumed. From a mathematical point of view only a change of the basis of the parameter space is done.

In the following, electric currents are used for describing the state of electrical machines. Due to this implementation decision, flux linkages or inductances can be used as model parameters and have to be given by look-up tables.

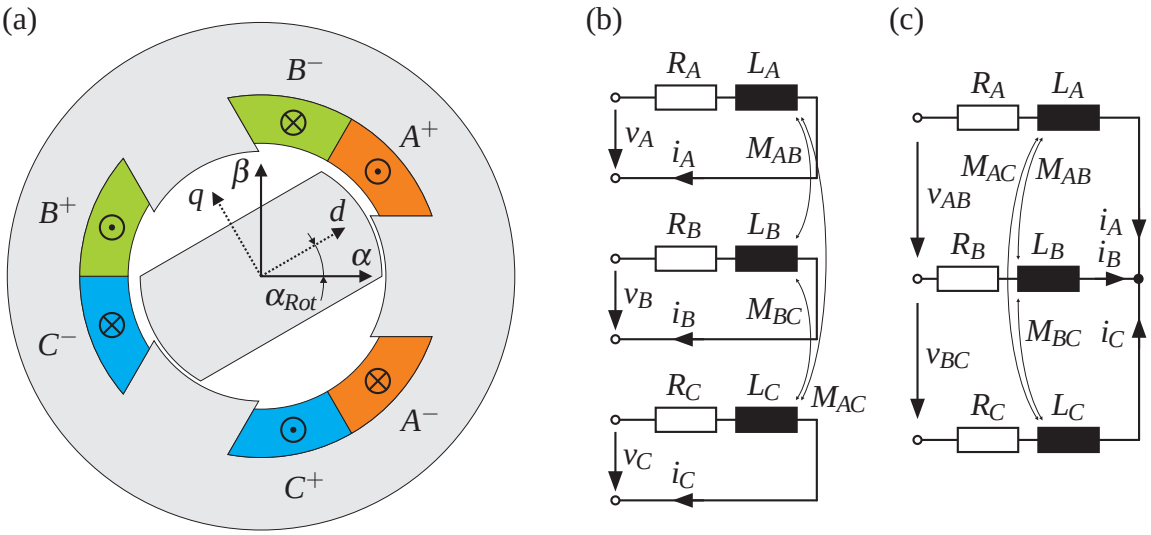

Figure 4.1: Hypothetical machine with a three-phase coil system on the stator and a rotor without coils. (a) Machine topology with the stator related $\alpha\beta$-system and the rotor related dq-system. (b) Equivalent circuit diagram for the stator coil system with independent coils. (c) Equivalent circuit diagram for the stator coil system in Y-connection with isolated star point.

Let us assume a hypothetical machine for all further considerations in this section, as shown in Fig. 4.1a. This machine has a three-phase coil system on the stator and a rotationally asymmetric rotor without any coils. Thus, it represents a crude reluctance machine. For this machine with independent stator coils (Fig. 4.1b), the voltage equations using inductances can be written as

$$\begin{pmatrix} v_A \\ v_B \\ v_C \end{pmatrix} = \begin{pmatrix} R_A i_A \\ R_B i_B \\ R_C i_C \end{pmatrix} + \frac{d}{dt} \underbrace{\begin{bmatrix} L_A & M_{AB} & M_{AC} \\ M_{AB} & L_B & M_{BC} \\ M_{AC} & M_{BC} & L_C \end{bmatrix}}_{=:\mathbf{L}} \begin{pmatrix} i_A \\ i_B \\ i_C \end{pmatrix}$$

$$= \begin{pmatrix} R_A i_A \\ R_B i_B \\ R_C i_C \end{pmatrix} + \left(\partial_{\alpha_{Rot}} \mathbf{L} \frac{d\alpha_{Rot}}{dt} + \partial_{i_d} \mathbf{L} \frac{di_d}{dt} + \partial_{i_q} \mathbf{L} \frac{di_q}{dt} + \partial_{i_0} \mathbf{L} \frac{di_0}{dt} \right) \begin{pmatrix} i_A \\ i_B \\ i_C \end{pmatrix} + \mathbf{L} \begin{pmatrix} \frac{di_A}{dt} \\ \frac{di_B}{dt} \\ \frac{di_C}{dt} \end{pmatrix}, \tag{4.2}$$

using $dq0$-components for the current feed state. All inductances are functions of α_{Rot}, i_d, i_q and i_0. Due to symmetry of the inductance matrix $\mathbf{L}$ this approach requires no more than

six look-up tables. Furthermore, the function value as well as all four partial derivatives of each look-up table quantity has to be evaluated in general. Thus, an appropriate interpolation method is required. Alternatively, 18 additional look-up tables with the corresponding partial derivatives can be used.

In contrast, using flux linkages for describing this system leads to

$$\begin{aligned}\begin{pmatrix} v_A \\ v_B \\ v_C \end{pmatrix} &= \begin{pmatrix} R_A i_A \\ R_B i_B \\ R_C i_C \end{pmatrix} + \frac{d}{dt}\begin{pmatrix} \psi_A\left(\alpha_{Rot}, i_d, i_q, i_0\right) \\ \psi_B\left(\alpha_{Rot}, i_d, i_q, i_0\right) \\ \psi_C\left(\alpha_{Rot}, i_d, i_q, i_0\right) \end{pmatrix} \\ &= \begin{pmatrix} R_A i_A \\ R_B i_B \\ R_C i_C \end{pmatrix} + \begin{pmatrix} \partial_{\alpha_{Rot}}\psi_A \\ \partial_{\alpha_{Rot}}\psi_B \\ \partial_{\alpha_{Rot}}\psi_C \end{pmatrix}\frac{d\alpha_{Rot}}{dt} + \begin{bmatrix} \partial_{i_d}\psi_A & \partial_{i_q}\psi_A & \partial_{i_0}\psi_A \\ \partial_{i_d}\psi_B & \partial_{i_q}\psi_B & \partial_{i_0}\psi_B \\ \partial_{i_d}\psi_C & \partial_{i_q}\psi_C & \partial_{i_0}\psi_C \end{bmatrix}\begin{pmatrix} \frac{di_d}{dt} \\ \frac{di_q}{dt} \\ \frac{di_0}{dt} \end{pmatrix}.\end{aligned} \tag{4.3}$$

Without any additional constraints or simplifications this ansatz requires three look-up tables for the phase flux linkages and the evaluation of all four partial derivatives. Alternatively, 12 look-up tables with the corresponding partial derivatives can be used.

Obviously, both the calculation cost and the memory demand of the second approach is lower. Furthermore, the determination of flux linkages with FEM is simpler than the determination of the inductance matrix in nonlinear case as shown in subsection 3.5.7. Finally, it should be mentioned that the consideration of permanent magnets requires no additional actions in the second case. In the first case an additional look-up table is required because the flux due to permanent magnets is not included in $\mathbf{L}$.

Many publications in the literature can be found using inductances, e.g. [58], [19], [36]. This seems to be mainly caused by the fact that inductances are more popular and easier to measure. Furthermore, many FEM tools include an automated determination of the inductance matrix implemented. However, the use of flux linkages is the better choice for FE based machine models and is used in the following.

In many cases, additional constraints allow a simplification of (4.3) or (4.2). Typically, all coils on both the stator and the rotor are interconnected and build two poly-phase coil systems. Furthermore, these systems are symmetric too and several look-up tables can be saved. For the machine in Fig. 4.1 one look-up table for all flux linkages is sufficient. Due to the fact that the current state variables used are defined in a rotor related reference system, this look-up table has to be evaluated at different rotor positions but with the same currents:

$$\Psi_A\left(\alpha_{Rot}, i_d, i_q, i_0\right) = \Psi_B\left(\alpha_{Rot} - 120^{\circ\mathrm{E}}, i_d, i_q, i_0\right) = \Psi_C\left(\alpha_{Rot} - 240^{\circ\mathrm{E}}, i_d, i_q, i_0\right). \tag{4.4}$$

For the stator related $\alpha\beta$-coordinate system, the current feed state variables have to be transformed, too. In case of a Y-connection with isolated star point the additional constraint

$$i_A + i_B + i_C = 0 \tag{4.5}$$

for the machine currents has to be considered and thus i_0 vanishes. Furthermore, the phase voltages are unknown because the potential of the isolated star point is typically unknown.

However, two phase-to-phase voltage equations can be used in this case for describing the electrical behavior of the coil system. For the machine in Fig. 4.1 this leads finally to

$$\begin{aligned}\begin{pmatrix} v_{AB} \\ v_{BC} \end{pmatrix} = \begin{pmatrix} v_A - v_B \\ v_B - v_C \end{pmatrix} &= R_{ph} \begin{pmatrix} i_A - i_B \\ i_B - i_C \end{pmatrix} + \frac{d}{dt} \begin{pmatrix} \psi_A\left(\alpha_{Rot}, i_d, i_q\right) - \psi_B\left(\alpha_{Rot}, i_d, i_q\right) \\ \psi_B\left(\alpha_{Rot}, i_d, i_q\right) - \psi_C\left(\alpha_{Rot}, i_d, i_q\right) \end{pmatrix} \\ &= R_{ph} \begin{pmatrix} i_{AB} \\ i_{BC} \end{pmatrix} + \begin{pmatrix} \partial_{\alpha_{Rot}} \psi_{AB} \\ \partial_{\alpha_{Rot}} \psi_{BC} \end{pmatrix} \frac{d\alpha_{Rot}}{dt} + \begin{bmatrix} \partial_{i_d} \psi_{AB} & \partial_{i_q} \psi_{AB} \\ \partial_{i_d} \psi_{BC} & \partial_{i_q} \psi_{BC} \end{bmatrix} \begin{pmatrix} \frac{di_d}{dt} \\ \frac{di_q}{dt} \end{pmatrix},\end{aligned} \tag{4.6}$$

with the phase resistance R_{ph}. Taking (4.4) into account, just one phase-to-phase flux linkage (e.g. ψ_{AB}) is sufficient.

Additional to the electrical behavior of the machine, the mechanical behavior needs to be described too. This can be done by using approximations based on analytical models, as for example presented in [50] for a permanent magnet machine

$$\tau = \sum_{i \in \{A,B,C\}} n_{mp} \left(\frac{1}{2} \frac{dL_i(\alpha_{Rot})}{d\alpha_{Rot}} i_i^2 + \frac{d\psi_{R,i}(\alpha_{Rot})}{d\alpha_{Rot}} i_i \right) + \tau_{Cog}(\alpha_{Rot}), \tag{4.7}$$

with the number of magnetic pole pairs n_{mp}, the flux linkage caused by the permanent magnets per phase $\psi_{R,i}$ and an additional term to consider cogging torque τ_{Cog}. Obviously, this ansatz assumes linearity and thus neglects any saturation effects. In [44] an improved model approach is presented using

$$\tau = \sum_{i \in \{A,B,C\}} n_{mp} \left(\frac{1}{2} \frac{dL_i(\alpha_{Rot}, i_d, i_q)}{d\alpha_{Rot}} i_i^2 + \frac{d\psi_{R,i}(\alpha_{Rot}, i_d, i_q)}{d\alpha_{Rot}} i_i \right) + \tau_{Cog}(\alpha_{Rot}) \tag{4.8}$$

for considering saturation. It is mentioned that even in this case the magnetic energy and co-energy are assumed to be equal. Furthermore, an additional look-up table for $\tau_{Cog}(\alpha_{Rot})$ is required for both approaches. Cogging torque is a special kind of torque ripple that occurs in permanent magnet machines. It is caused by a varying magnetic reluctance in circumferential direction and is defined for open circuit condition only. However, torque ripple caused by varying magnetic reluctance is also part of the total torque ripple in normal operation as assumed in (4.8). Thus, this torque ripple depends on the material saturation which is not considered by the above approaches.

The simplest approach describing the mechanical behavior is the use of an additional look-up table for the machine torque τ

$$\tau = \tau(\alpha_{Rot}, i_d, i_q), \tag{4.9}$$

as presented in [61]. This approach requires only little additional calculation effort for determining the machine torque during the FEM simulations. However, it covers all effects taken into account by magnetostatic FEM and hence leads to a very accurate description of machine torque.

In the sense of highest possible model parameter consistency and accuracy, all required model parameters should be defined by characteristic curves that are generated by the same FEM simulations. This leads under the assumption of an adequate sampling of the parameter space to a FE based model that is comparable to a magnetostatic FE model. This is shown in the next chapter 5 for various machine types.

4.2 Creation of look-up tables by FE simulations

The look-up table creation process is the part of the FE based model approach consuming the most calculation time. Typically, a high number of FE simulations have to be carried out and thus a well-designed preprocessing task is required. However, it should be mentioned that the look-up table generation has to be done once only.

An investigation of the preprocessing workflow shows that the calculation cost is mainly influenced by the following issues:

- FE model size
- Number of required sampling points
- Simulation setup
- Parallelization

Reasonably, the FE model size should be kept as small as necessary and all machine symmetries should be utilized as shown in section 3.5. Furthermore, 3D-FEM models should be avoided for the look-up table generation process.

The number of required FE simulations should be also kept as low as possible. This number is similar to the number of required sampling points and is mainly influenced by the chosen interpolation method. For instance, a piecewise linear interpolation requires a higher number of sampling points to achieve the same interpolation quality as a cubic spline interpolation does.

Every nonlinear FEM simulation requires several nonlinear iterations to reach the solution. However, a reduction of the number of these nonlinear iterations reduces the required simulation time per sampling point. This could be achieved by an efficient simulation setup as shown in the next subsection 4.2.1.

Due to the fact that only magnetostatic FEM simulations have to be carried out, the preprocessing task could be parallelized. This is caused by the fact that all magnetostatic FE simulations are independent of each other. The degree of parallelization is only limited by the availability of resources.

The results in the following chapters show that the consideration of these issues leads to a feasible look-up table generation process.

4.2.1 FE simulation setup

Let us assume a FE based model with n parameter variables x_i and the corresponding number of sampling points N_i. In this case N_{Sample} simulations have to be carried out with

$$N_{Sample} = \prod_{i=1}^{n} N_i. \tag{4.10}$$

This means that the number of required simulations grows exponentially with the number of parameter variables.

The FE-based model of the hypothetical machine shown in the last section has $n = 3$ parameter variables. The corresponding simulation control structure is shown in Fig. 4.2a. Due to the fact that all loops are independent, they can be parallelized. For the outermost loop this approach is shown in Fig. 4.2b.

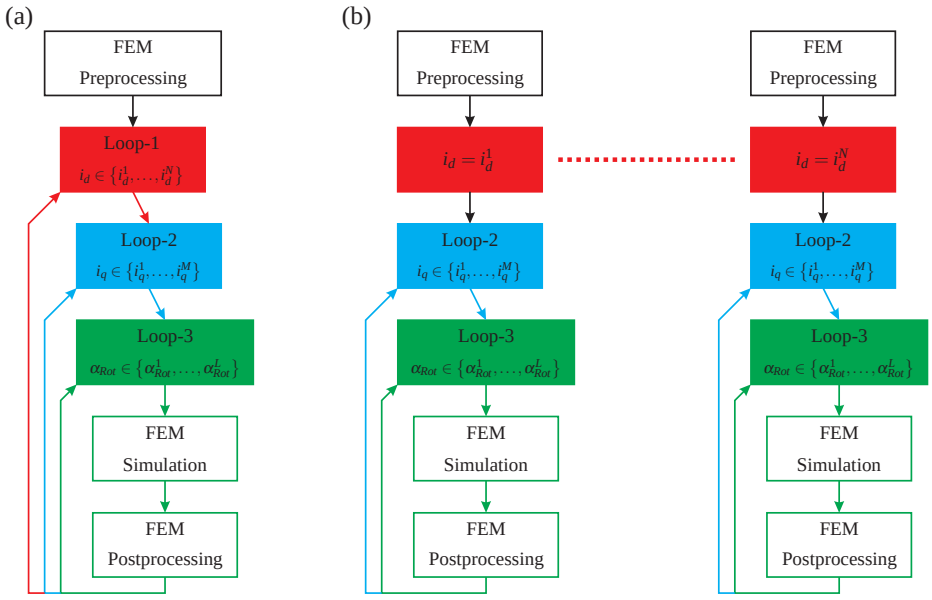

Figure 4.2: Simulation control flow diagram for the hypothetical machine shown in Fig. 4.1 with three parameter variables: (a) Flow diagram in case of no parallelization with three cascaded loops. (b) Flow diagram in case of parallelization of the outermost loop.

In case of nonlinear material properties (and this is the default case), every FEM simulation requires a couple of nonlinear iterations. A reduction of the number of these iterations can be expected if a good initial guess for the material properties is available. However, this requires two prerequisites:

- Impressing of initial material properties must be supported by the used FEM tool. In *ANSYS 14.5* for instance this can be achieved by doing a transient simulation without

time integration. Thus, it becomes a sequence of simple magnetostatic calculations but the material properties of the last simulation are used in each new one.

- A good initial guess for the material properties must be available. It is known that for transient nonlinear FEM simulations the number of nonlinear iterations is very small. This is caused by the fact that for two succeeding simulations the material properties do not change significantly. Thus the material properties of the last simulation are a very good initial guess for the new simulation. The same effect can be expected if the input parameters of the magnetostatic FE simulations are permutated in a way that the material properties do not change significantly. Therefore, the configuration of the loops becomes important.

The hypothetical machine shown in Fig. 4.1a with the equivalent circuit shown in Fig. 4.1c requires the parameter variables α_{Rot}, i_d and i_q as already mentioned before. Furthermore, it can be assumed that the most sampling points are required for the rotor position. This is caused by the fact that the field and torque harmonics due to slotting have to be sampled adequately enough. The parameters for the current feed state in contrast have to sample the effect of saturation only.

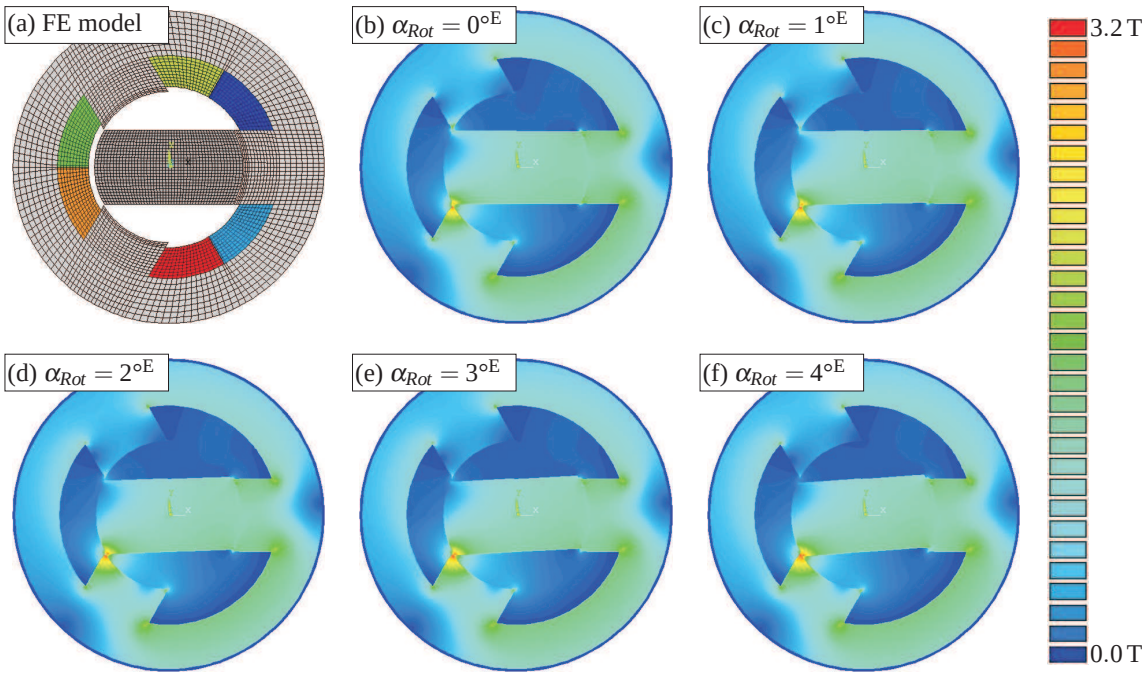

Figure 4.3: FEM simulations using the simulation flow shown in Fig. 4.2.a. (a) FE model of the hypothetical machine (Fig. 4.1). (b)-(f) Magnetic flux density for succeeding simulations. The rotor position α_{Rot} is changed in $1^{\circ E}$ steps while the state currents i_d, i_q are kept constant.

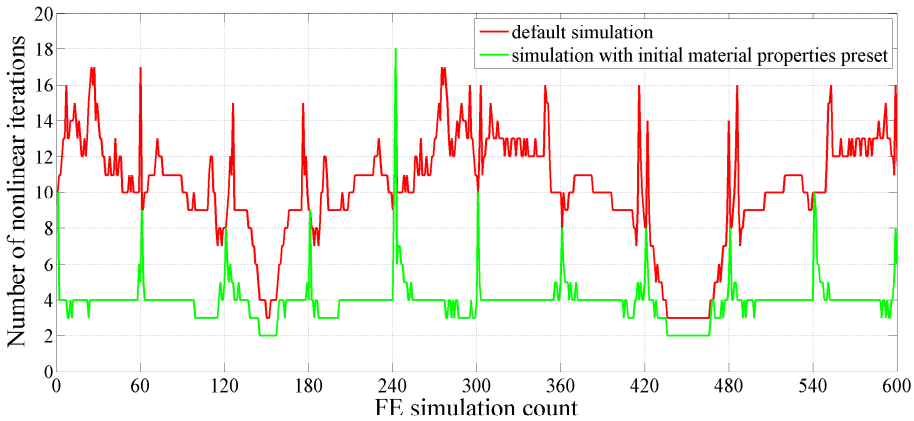

Figure 4.4: Comparison of the number of required nonlinear iterations: The red curve shows the number of iterations for magnetostatic simulations without any additional simulation flow control mechanisms. The green curve shows the number of iterations for the simulation flow with impressed initial material properties as suggested in this subsection. The periodic peaks of the number of nonlinear iterations every 60 simulations are caused by the change of the current feed state.

Therefore, it can be assumed that a small rotor rotation will have no significant influence on the material properties. This leads finally to the loop configuration shown in Fig. 4.2a with the innermost loop changing the rotor position. In Fig. 4.3, the FE model and several field plots for succeeding FE simulations with different rotor positions are shown. Obviously, the flux distribution between these simulations does not change significantly.

In Fig. 4.4 a comparison with FE simulations without the use of initial material properties and the simulation control mechanism suggested in this subsection is shown. The average number of nonlinear iterations for the used FE model is reduced from approximately 10 to 3.9 per simulation. This leads further to a simulation cost reduction from three hours to two hours. Thus 33 percent of the calculation cost are saved. Note, that for each FE simulation a modification of the FE model and a post processing for evaluating the look-up table quantities is necessary. Therefore, the simulation cost reduction is less than expected from the reduction of the number of nonlinear iterations. However, the reachable reduction mainly depends on the convergence behavior of the FE model. Therefore, a generally valid estimation cannot be established.

This approach can be basically applied to all machine types. This method is recommended especially for reluctance machines and permanent magnet machines. However, for machines with two coupled coil systems a further improved simulation flow can be found by keeping the magneto-motive force constant, as presented in the next subsection.

4.2.2 Method of constant magneto motive force

Let us assume a wound rotor induction machine with two three-phase coil systems in Y-connection and isolated star points (see subsection 5.4.2). The current feed state of this machine is defined by four current parameters. This leads in total to five parameter variables and thus to a very high number of required simulations. Using the algorithm shown in Fig. 4.2 speeds up the FE simulations by reducing the number of nonlinear iterations. However, for every simulation a new rotor position and new constraint equations have to be defined and the system matrix has to be reassembled. This procedure costs time and has to be repeated for every current feed state configuration. An improvement can be attained by additionally keeping the magneto-motive force constant.

The main flux in the machine is generated by the magneto-motive force Θ, again generated by both coil systems. It can be assumed that the saturation state of the machine depends mainly on Θ and that for a constant Θ this saturation state remains approximately constant. These two assumptions finally lead to the method of constant magneto-motive force, presented in [64]. This method is recommended for the look-up table generation for machines with more than one coil system.

To enforce a constant magneto-motive force Θ for several simulations, the same reference system for all current feed parameters has to be used. For the stator related $\alpha\beta$-system, Θ of the machine can be decomposed into the corresponding α- and β-components. This leads to

$$\Theta = \begin{pmatrix} \Theta_\alpha \\ \Theta_\beta \end{pmatrix} = \begin{pmatrix} \Theta_{S,\alpha} \\ \Theta_{S,\beta} \end{pmatrix} + \begin{pmatrix} \Theta_{R,\alpha} \\ \Theta_{R,\beta} \end{pmatrix} = N_S \begin{pmatrix} i_{S,\alpha} \\ i_{S,\beta} \end{pmatrix} + N_R \begin{pmatrix} i_{R,\alpha} \\ i_{R,\beta} \end{pmatrix}, \tag{4.11}$$

with the number of windings of the stator phase coil N_S and of the rotor phase coil N_R.

For the increments $\Delta\Theta_\alpha$ and $\Delta\Theta_\beta$ the additional constraints

$$\Delta\Theta_\alpha = N_S \Delta i_{S,\alpha} = N_R \Delta i_{R,\alpha}, \tag{4.12}$$

$$\Delta\Theta_\beta = N_S \Delta i_{S,\beta} = N_R \Delta i_{R,\beta}, \tag{4.13}$$

are required. Thus the same number of sampling points L for $i_{S,\alpha}$ and $i_{R,\alpha}$ and K for $i_{S,\beta}$ and $i_{R,\beta}$ must be used. However, this is typically no restriction because both coil systems are comparable in the sense of power transmission. In Fig. 4.5a, the default simulation loop configuration for a model with five parameter variables and thus five independent loops is shown. The improved loop configuration is shown in Fig. 4.5b. Notice that only the three outer loops are independent and the two inner loops depend on the loops for Θ_α and Θ_β. Furthermore, Fig. 4.5c shows the sampling scheme of the Θ_α parameter subspace. An additional control mechanism is required to select the possible i_S-i_R-combinations for the actual Θ-component. The corresponding pseudo code is shown in Fig. 4.5d.

In Fig. 4.6, several variations of the Θ-components are shown. For all shown configurations the total magneto-motive force Θ is equal but the composition with respect to its rotor and stator generated components vary.

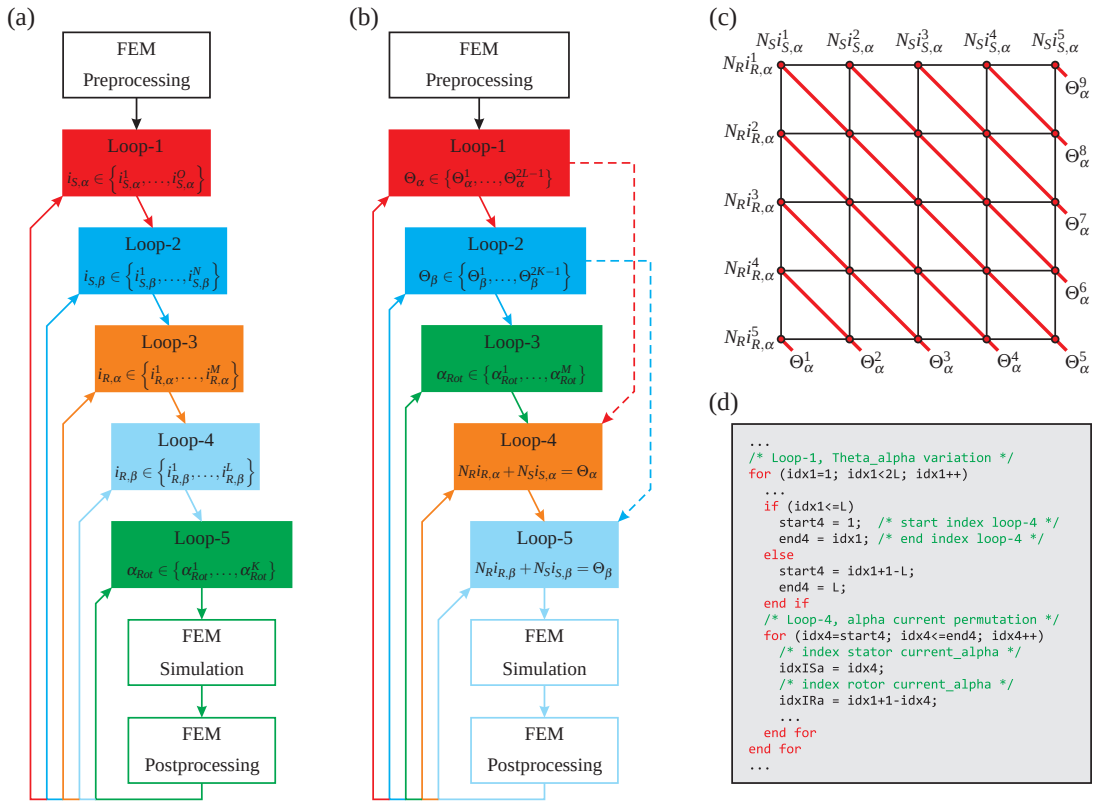

Figure 4.5: Simulation control flow diagram for a machine with five parameter variables: (a) Flow diagram using five independent loops. (b) Flow diagram for the method of constant magneto-motive force with two coupled loops to enforce a constant magneto-motive force. (c) Sampling scheme of the parameter space build by $i_{S,\alpha}$ and $i_{R,\alpha}$. Instead of an independent variation of both currents a coupled variation is done keeping Θ_α constant. This leads to the shown sampling scheme in diagonal direction (red). (d) Pseudo code for index determination for $i_{S,\alpha}$ and $i_{R,\alpha}$ permutation.

In Fig. 4.7, a comparison of the required number of nonlinear iterations between a simulation without any simulation flow control and the presented method of constant magneto-motive force is shown. These results relate to the WRIM model described in subsection 5.4.2. A reduction of the number of nonlinear iterations by about a factor of four has been achieved. The required FE simulation cost has been reduced by a factor of about three (from 570 h to 190 h). These results relate to the FE model used and are not valid in general. However, the proper functioning of the proposed method has been illustrated.

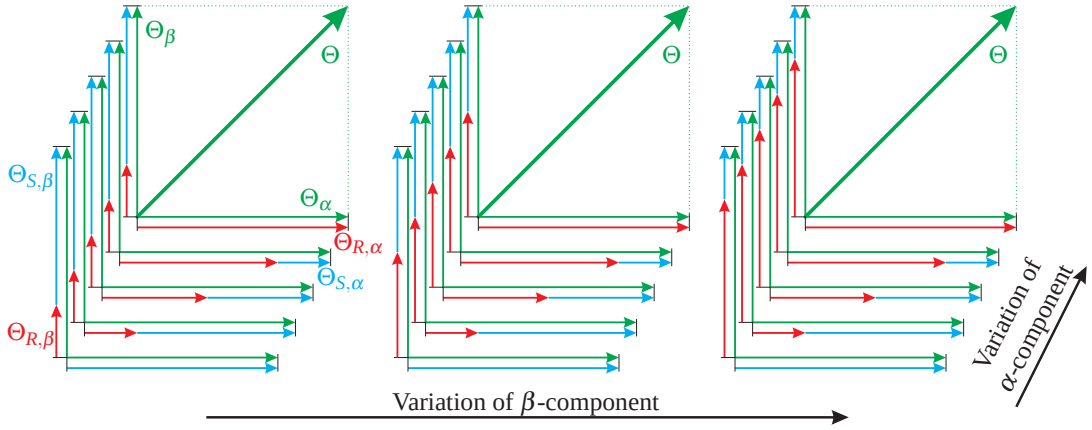

Figure 4.6: Variations of the Θ-components. For all 5×3 cases the total magneto-motive vector is the same. All 15 cases vary only in the way the α-component Θ_α and β-component Θ_β of Θ are composed with respect to the rotor and stator generated part. In this sense, five variations for Θ_α and three variations for Θ_β are shown.

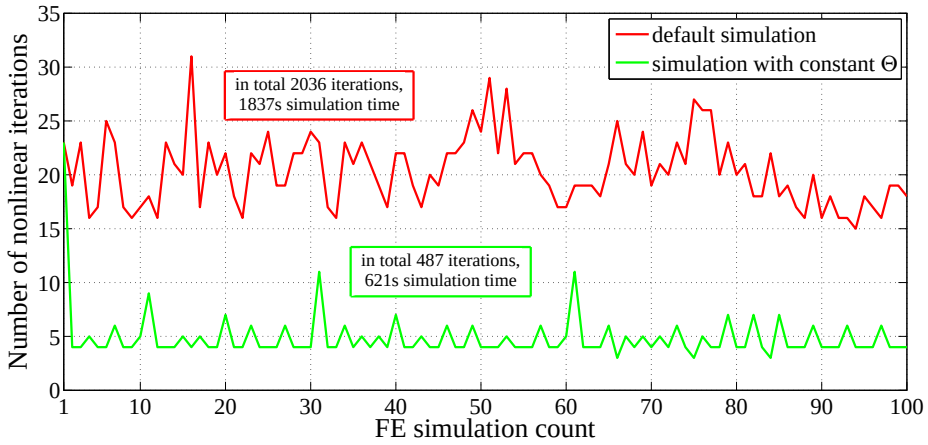

Figure 4.7: Comparison of required nonlinear iterations using the method of constant magneto-motive force: The red curve shows the required iterations for magnetostatic simulations without any additional simulation flow control mechanisms. The green curve shows the required iterations using the method of constant magneto-motive force.

4.3 Interpolation method

For the model defined in (4.3), an interpolation method with a direct evaluation of the first partial derivatives is required. Additionally, this system of equations is nonlinear and an iterative solution method is required. For a good convergence behavior, all interpolated

partial derivatives should be continuous. This condition is fulfilled within any segment for all interpolation functions which are at least C^1-continuous. But, at the segment boundaries, additional constraints are required to enforce this. For example, a linear interpolation is C^1-continuous in every segment but, at the segment boundaries, the first derivatives are not continuous. In contrast, a cubic spline interpolation can be made C^1-continuous in the whole parameter space. This is achieved by the right choice of constraints during the spline parameter determination as shown for a tri-cubic spline interpolation in subsection 2.3.2.

4.3.1 Continuity conditions for cubic splines in *n* variables

In this subsection, the required constraints for C^1-continuity in the whole parameter space for a n-dimensional cubic spline interpolation with a rectangular sampling grid is presented. In subsection 2.3.1, the parameter determination for a cubic-spline interpolation has been described. For every segment, four spline parameters have to be determined. This was done by using the function value F at the sampling points (sampled data) and two additional coupling terms to enforce C^2-continuity. This leads for the whole parameter space to a single system of equations as shown in (2.114). However, for C^1-continuity, the presetting of F and the first-order derivative f_x in every sampling is sufficient. This leads for every segment to a system of four equations

$$\begin{pmatrix} F\left(x^L\right) \\ f_x\left(x^L\right) \\ F\left(x^H\right) \\ f_x\left(x^H\right) \end{pmatrix} = \begin{bmatrix} 1 & 0 & 0 & 0 \\ 0 & 1 & 0 & 0 \\ 1 & \Delta x & \Delta x^2 & \Delta x^3 \\ 0 & 1 & 2\Delta x & 3\Delta x^2 \end{bmatrix} \begin{pmatrix} a_0 \\ a_1 \\ a_2 \\ a_3 \end{pmatrix}, \tag{4.14}$$

with the segment's lower bound x^L, the segment's higher bound x^H and $\Delta x := x^H - x^L$. Due to the monomial base, a_0 and a_1 are directly given and the resulting system of equations can be written as

$$\begin{pmatrix} F\left(x^H\right) - F\left(x^L\right) - f_x\left(x^L\right)\Delta x \\ f_x\left(x^H\right) - f_x\left(x^L\right) \end{pmatrix} = \begin{bmatrix} \Delta x^2 & \Delta x^3 \\ 2\Delta x & 3\Delta x^2 \end{bmatrix} \begin{pmatrix} a_2 \\ a_3 \end{pmatrix}. \tag{4.15}$$

This system is linearly independent for $|\Delta x| > 0$. It should be mentioned that an additional presetting of the second-order derivative f_{xx} in the sampling points leads to an overdetermined system of equations. This system is only solvable if all f_x and f_{xx} are equal to the corresponding values of the solution of (2.114).

In the n-dimensional case, all spline parameters can be also determined for every segment independently. In this case, 4^n constraints per segment are necessary to achieve a unique solution. The number of sampling points (vertices) that define every segment is 2^n. Thus, for every sampling point 2^n constraints are required. Furthermore, it is not possible to use any second-order (or higher-order) partial derivative with respect to one parameter because the multi-dimensional cubic spline collapses at all edges of any segment to a

one-dimensional cubic spline. In that case the system becomes over-determined again, as shown before. Therefore, only first-order partial derivatives with respect to one parameter can be used. In the 2D-case, this leads to F, f_x, f_y and f_{xy} and, in 3D case, to the constraints already shown in subsection 2.3.2. In general, these are:

$$F, \binom{n}{1} f_{x_i}, \binom{n}{2} f_{x_i x_j}, \binom{n}{3} f_{x_i x_j x_k}, \ldots, \binom{n}{n} f_{x_1 x_2 \ldots x_n}, \tag{4.16}$$

with $1 \leq i, j, k \leq n$ and $i \neq j \neq k$. This yields all required 2^n constraints per sampling point.

4.3.2 Proof of C^1-continuity for cubic splines in n variables

Using the spline construction shown in the previous subsection leads for 1D splines to C^1-continuity in the whole parameter space by the construction itself.

By mathematical induction, the same is true for all higher dimensional splines, as shown for three dimensional splines in [43]. The basic case for this method of proof is the bi-cubic spline. In the 2D case, the spline $p(x_1, x_2)$ of each segment collapses at the segment boundaries to 1D splines. This leads for both edges (E_1, E_3 in Fig. 4.8) in x_1-direction (i.e. with constant x_2) to

$$p^{E_1}(x_1) := p(x_1, x_2^L) = \sum_{i=0}^{3} a_{0,i} \tilde{x}_1^{\,i}, \tag{4.17}$$

$$p^{E_3}(x_1) := p(x_1, x_2^H) = \sum_{i=0}^{3} \underbrace{\left(\sum_{j=0}^{3} a_{j,i} \Delta x_2^{\,j} \right)}_{b_i} \tilde{x}_1^{\,i} = \sum_{i=0}^{3} b_i \tilde{x}_1^{\,i}, \tag{4.18}$$

with $x_1^L \leq x_1 < x_1^H$, $\tilde{x}_1 := x_1 - x_1^L$ and $\Delta x_2 := x_2^H - x_2^L$. These splines are defined uniquely by the values for F and f_{x_1} in the corresponding vertices. Thus, the splines for two adjacent segments are identical and continuity of $p(x_1, x_2)$ and $\partial_{x_1} p(x_1, x_2)$ is guaranteed.

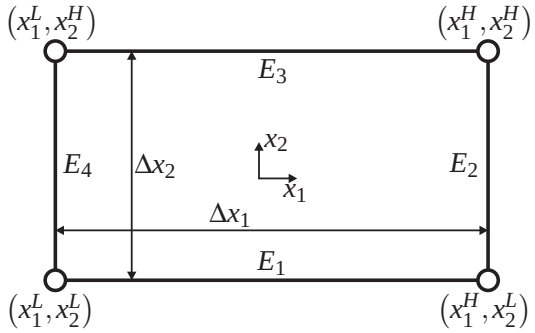

Figure 4.8: 2D segment: Rectangle with 4 vertices and 4 edges. On all edges E_1 to E_4 the bi-cubic spline $p(x_1, x_2)$ collapses into a cubic spline.

To show the continuity of $\partial_{x_2} p(x_1, x_2)$, the same ansatz can be used. For this purpose, the partial derivative with respect to the edge's constant parameter x_2 in both edges (E_1, E_3) has to been utilized:

$$\partial_{x_2} p^{E_1}(x_1) := \frac{\partial}{\partial x_2} p(x_1, x_2^L) = \sum_{i=0}^{3} a_{1,i} \tilde{x}_1^i, \tag{4.19}$$

$$\partial_{x_2} p^{E_3}(x_1) := \frac{\partial}{\partial x_2} p(x_1, x_2^H) = \sum_{i=0}^{3} \underbrace{\left(\sum_{j=1}^{3} j a_{j,i} \Delta x_2^{j-1} \right)}_{c_i} \tilde{x}_1^i = \sum_{i=0}^{3} c_i \tilde{x}_1^i. \tag{4.20}$$

These 1D splines and their partial derivative with respect to x_1 are equal to the preset values for f_{x_2} and $f_{x_2 x_1} = f_{x_1 x_2}$ in the corresponding vertices. Thus, the 1D splines of adjacent segments are also identical and hence C^1-continuity for E_1 and E_3 is ensured. A proof in the same manner can be done for both edges in x_2-direction (E_2, E_4) and thus with constant x_1. Therefore, C^1-continuity in the whole parameter space has been proved.

For the induction step, any n-dimensional spline is reduced to $(n-1)$-dimensional splines at its segment boundaries. Furthermore, the partial derivative with respect to the face's constant parameter also leads to a second $(n-1)$-dimensional spline for each face. For adjacent segments, both $(n-1)$-dimensional splines at the corresponding face are identical, and thus, C^1-continuity for the whole parameter space is ensured.

For a 4D spline interpolation for instance, each segment is a 4D hyper cuboid defined by $2^4 = 16$ vertices, as shown in Fig. 4.9. The spline $p(x_1, x_2, x_3, x_4)$ in every segment is defined by $4^4 = 256$ parameters

$$p(x_1, x_2, x_3, x_4) = \sum_{l=0}^{3} \sum_{k=0}^{3} \sum_{j=0}^{3} \sum_{i=0}^{3} a_{l,k,j,i} \tilde{x}_1^i \tilde{x}_2^j \tilde{x}_3^k \tilde{x}_4^l, \tag{4.21}$$

in which the values for $F, f_{x_1}, f_{x_2}, ..., f_{x_1 x_2}, ..., f_{x_1 x_2 x_3}, ..., f_{x_2 x_3 x_4}$ and $f_{x_1 x_2 x_3 x_4}$ are preset at every vertex.

Each segment is bounded by eight faces that are 3D rectangular cuboids. Thus, the 4D spline collapses at every face into a 3D spline. For instance for the face with $x_4 = x_4^L$ this 3D spline is defined uniquely by 8 vertices and the corresponding 8 preset values for $F, f_{x_1}, f_{x_2}, f_{x_3}, f_{x_1 x_2}, ...$ and $f_{x_1 x_2 x_3}$ in each vertex. These are the partial derivatives with respect to all variables but x_4. The same 3D spline is defined in the adjacent segment sharing this face. Thus, continuity of $p(x_1, x_2, x_3, x_4)$, $\partial_{x_1} p(x_1, x_2, x_3, x_4)$, $\partial_{x_2} p(x_1, x_2, x_3, x_4)$ and $\partial_{x_3} p(x_1, x_2, x_3, x_4)$ for this face segment is guaranteed.

Furthermore, the partial derivative with respect to the face's constant value x_4 collapses to a 3D spline at this face. This spline is defined uniquely with the values for $f_{x_4}, f_{x_1 x_4}, f_{x_2 x_4}, f_{x_3 x_4}, ...$ and $f_{x_1 x_2 x_3 x_4}$ at each vertex. These are all partial derivatives with respect to x_4. Due to the fact that the same can be done for the adjacent segment, $\partial_{x_4} p(x_1, x_2, x_3, x_4)$ is also continuous at this face. This leads finally to C^1-continuity in the whole parameter space, as shown in [64].

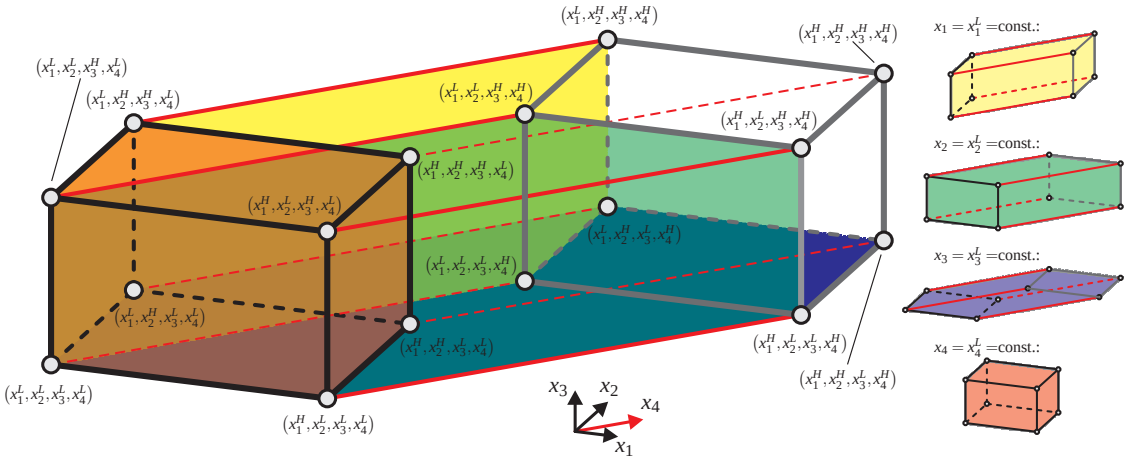

Figure 4.9: 4D hyper cuboid with 16 vertices and 8 rectangle cuboid shaped faces. All four cubes with one coordinate is equal to the lower bound are shown.

4.3.3 Spline parameter determination

For the spline parameter determination of a cubic spline, a single system of equations for the whole parameter space is used as already explained in subsection 2.3.1. For higher dimensional splines, this approach is limited because the number of spline parameters N_{para} increases exponentially with the number of dimensions n:

$$N_{para} = 4^n N_{Seg} = 4^n \prod_{i=1}^{n} (N_i - 1), \tag{4.22}$$

with the number of segments N_{Seg} and the number of sampling points N_i per dimension.

Nevertheless, the induction step of the proof of C^1-continuity can be used to design a recursive algorithm, as shown in [64]. Let us assume an n-dimensional spline segment with its reference vertex $V_{Ref} := \left(x_1^L, \ldots x_n^L\right)$. In this vertex all local coordinates $\tilde{x}_1$,...,$\tilde{x}_n$ vanish. For all segment faces including V_{Ref}, the n-dimensional spline collapses into an $(n-1)$-dimensional spline as shown before. Furthermore, all spline parameters of these $(n-1)$-dimensional splines can be directly identified as spline parameters of the n-dimensional spline. This is also valid for the partial derivative with respect to the face's constant coordinate as shown for a quint-cubic spline and for the face with $\tilde{x}_1 = 0$:

$$p(x_1, x_2, x_3, x_4, x_5)|_{\tilde{x}_1=0} = \sum_{m=0}^{3}\sum_{l=0}^{3}\sum_{k=0}^{3}\sum_{j=0}^{3} a_{m,l,k,j,0}\, \tilde{x}_2^{\,j}\, \tilde{x}_3^{\,k}\, \tilde{x}_4^{\,l}\, \tilde{x}_5^{\,m}, \tag{4.23}$$

$$\frac{\partial}{\partial x_1} p(x_1, x_2, x_3, x_4, x_5)\bigg|_{\tilde{x}_1=0} = \sum_{m=0}^{3}\sum_{l=0}^{3}\sum_{k=0}^{3}\sum_{j=0}^{3} a_{m,l,k,j,1}\, \tilde{x}_2^{\,j}\, \tilde{x}_3^{\,k}\, \tilde{x}_4^{\,l}\, \tilde{x}_5^{\,m}. \tag{4.24}$$

The quint-cubic spline parameters $a_{m,l,k,j,i}$ with $2 \leq i, j, k, l, m \leq 3$ cannot be determined by this approach. For these parameters, a separate system of equations per segment is

required. Therefore, the equations for all constraints of the diagonal vertex V_{Diag} with the coordinates $\left(x_1^H,\ldots,x_n^H\right)$ have to be set up.

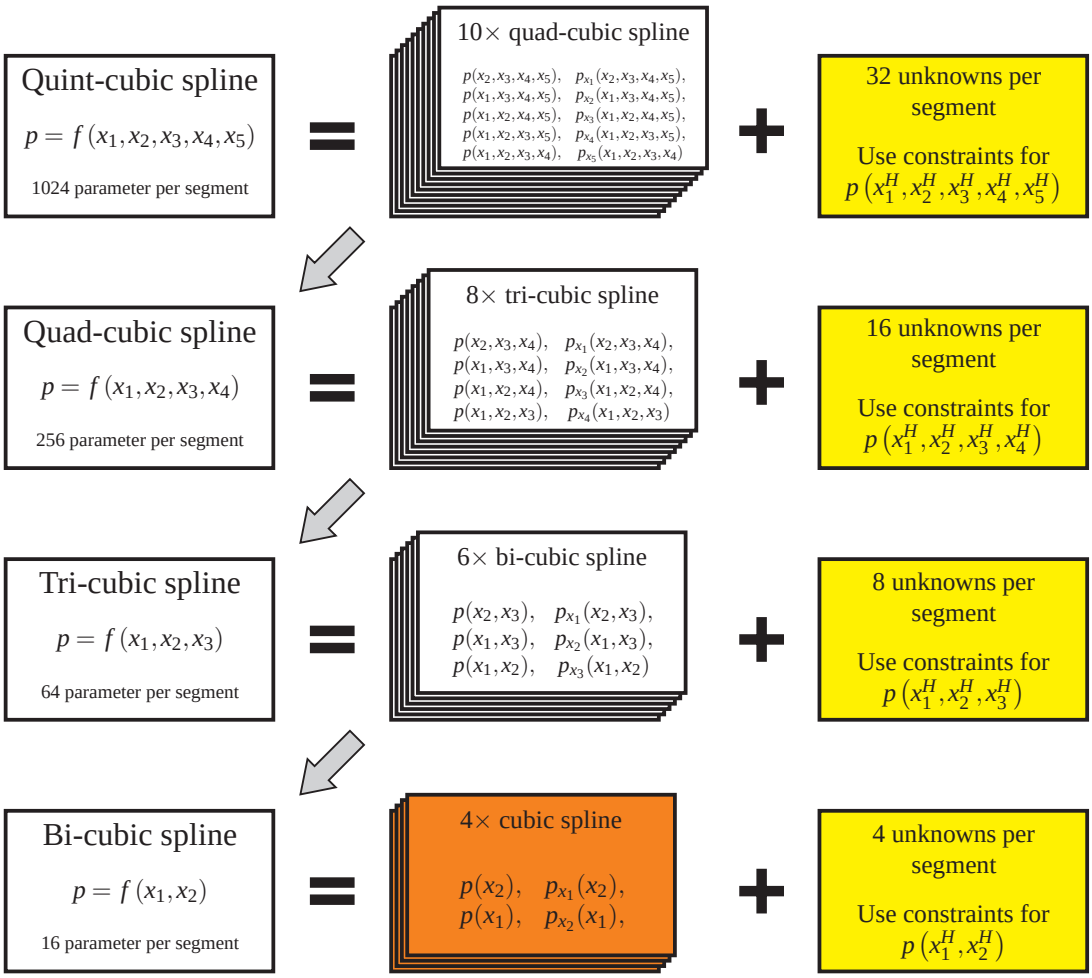

Figure 4.10: Recursive cubic spline parameter determination for an orthogonal sampling grid. Floating point operations are only required in the red block (cubic spline parameter determination) and the yellow blocks (small and independent systems of equations per segment).

However, each $(n-1)$-dimensional spline can be further degraded into $(n-2)$-dimensional splines and so on. This leads finally to the conclusion that only cubic splines along the sampling grid in every dimension for F and all required partial derivatives have to be determined, as shown in Fig. 4.10. It should be mentioned that by this spline dimension reduction the parameter space is sliced. Therefore, the $n-1$ dimensional splines have to be evaluated N_i-1 times, N_i being the number of sampling points for the coordinate x_i kept constant. Furthermore, it is mentioned that the system matrix for the cubic spline parameter determination (2.114) is constant for all grid lines in one direction. Thus, (2.114)

becomes a system of equations with many right hand sides. The same applies also for the equation systems for V_{Diag}. These systems are solved very effectively by LU-factorization.

Finally, note that all $(n-1)$-dimensional segments are adjacent. Thus, it is not necessary to determine all $(n-2)$-dimensional splines for every $(n-1)$-dimensional spline. For instance, the two quad-cubic splines $p(x_1,x_3,x_4,x_5)$ and $p(x_2,x_3,x_4,x_5)$ collapse for $x_1 = 0$ and $x_2 = 0$ respectively to the same tri-cubic spline $p(x_3,x_4,x_5)$. An analysis of this behavior leads to

$$N_{sub} = \binom{n}{n_{sub}} 2^{n-n_{sub}}, \tag{4.25}$$

with the number of n_{sub}-dimensional spline evaluations N_{sub}. The required evaluations up to quint-cubic splines are shown in table 4.1.

Table 4.1: Dimensional recursive function calls up to quint-cubic splines.

quint-cubic	quad-cubic	tri-cubic	bi-cubic	cubic
1	10	40	80	80
-	1	8	24	32
-	-	1	6	12
-	-	-	1	4

Table 4.2: Overview dimensional recursive spline parameter determination.

Interpolation	(N_1,N_2,N_3,N_4,N_5) $(-)$	N_{Sample} (10^3)	N_{Seg} (10^3)	N_{para} (10^6)	time (s)	memory (MiB)
tri-cubic	$(18,18,18,-,-)$	5.832	4.913	0.314	0.084	2.40
	$(36,36,36,-,-)$	46.65	42.87	2.744	0.887	20.9
	$(54,54,54,-,-)$	157.4	148.8	9.528	3.171	72.6
quad-cubic	$(7,7,7,7,-)$	2.401	1.296	0.332	0.168	2.53
	$(14,14,14,14,-)$	38.41	28.56	7.312	3.609	55.7
	$(21,21,21,21,-)$	194.4	160.0	40.96	20.57	312
quint-cubic	$(4,4,4,4,4)$	1.024	0.243	0.248	0.257	1.90
	$(8,8,8,8,8)$	32.76	16.80	17.21	15.42	131
	$(16,8,8,8,8)$	65.53	36.01	36.88	34.21	281
	$(32,8,8,8,8)$	131.0	74.43	76.21	71.99	581
	$(12,12,12,12,12)$	248.8	161.0	164.9	135.2	1258

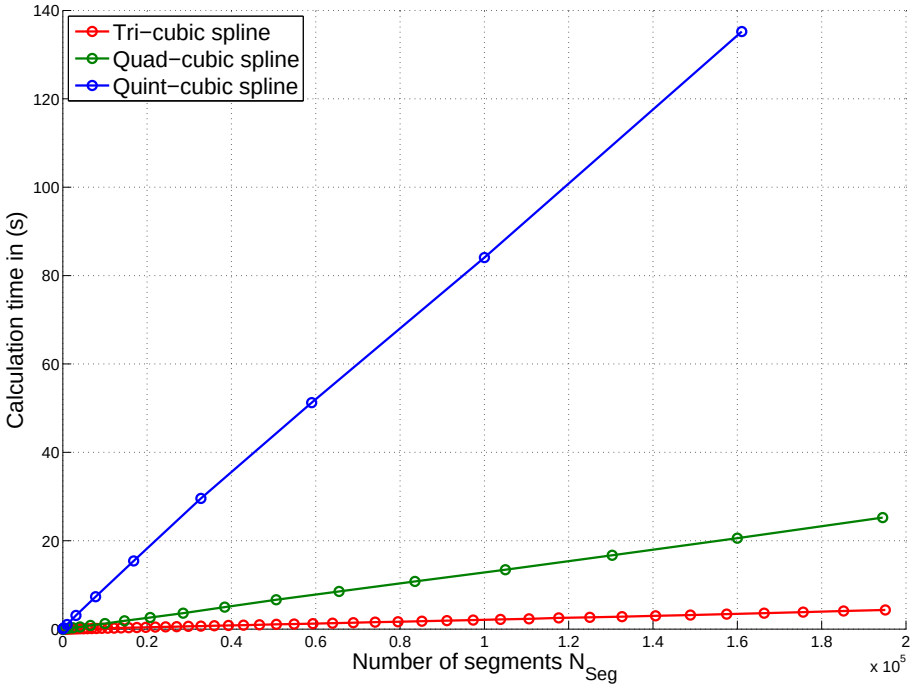

Figure 4.11: Calculation cost of dimensional recursive spline parameter determination algorithm for tri-cubic splines (red), quad-cubic splines (green) and quint-cubic splines (blue). Each spline type scales linearly with the number of segments.

The presented algorithm has been implemented up to quint-cubic splines in *Fortran 95*. Table 4.2 shows an overview for several test cases. All calculations have been carried out on the same computer (Intel Core2 Duo CPU, 8GiB RAM) without parallelization, thus the calculation times are directly comparable. The calculation cost scales linearly with the number of segments for each spline type as shown in Fig. 4.11. The memory demand for storing the resulting look-up table increases exponentially with the dimension. The resulting memory demand is in the range of several megabytes to a gigabyte as shown in Table 4.2. It is mentioned that such a memory demand is no problem for modern computers. Furthermore, note that it is typically not necessary to load the whole look-up tables into the memory. Depending on the trajectory of the state variables only a small section of the table is sufficient.

4.3.4 Look-up table evaluation

All spline parameters can be pre-calculated to minimize the calculation cost during the transient simulation. Note that this speed up is bought by a higher memory demand for the look-up tables. The look-up table size increases by a factor approximately equal to the number of spline parameters per segment. However, for state of the art computers

the required memory demand is still in an applicable size as shown in chapter 5. For the cubic spline evaluation the cascaded Horner scheme as described in subsection 2.3.3 can be used. This method can be also applied to the evaluation of the partial derivatives. Depending on the order in which the summations are evaluated the implementation is not unique, thus, in the n-dimensional case n implementations are possible. However, in total all implementations require the same number of floating point operations (FLOPs). For instance the two possible implementations for a bi-cubic spline are:

$$\frac{\partial}{\partial x_1} p(x_1,x_2) = \underbrace{\sum_{i=1}^{3} i \left(\sum_{j=0}^{3} a_{j,i} \tilde{x}_2^{\,j} \right) \tilde{x}_1^{\,i-1}}_{\text{Implementation A}} = \underbrace{\sum_{j=0}^{3} \left(\sum_{i=1}^{3} i\, a_{j,i} \tilde{x}_1^{\,i-1} \right) \tilde{x}_2^{\,j}}_{\text{Implementation B}}. \tag{4.26}$$

Both implementations require 30 FLOPs, in which implementation A requires 14 real-real multiplications, 14 real-real additions and 2 integer-real multiplications and implementation B requires 11 real-real multiplications, 11 real-real additions and 8 integer-real multiplications. Any difference regarding speed of implementation depends on the hardware used.

For the typical system of equations (4.3) to be solved for FE based models, all partial derivatives have to be evaluated. This feature can be utilized for a fast implementation as shown for a 5D spline

$$\frac{\partial}{\partial x_1} p(x_1,x_2,x_3,x_4,x_5) = \sum_{i=1}^{3} e_i\, i\, \tilde{x}_1^{\,i-1}, \tag{4.27}$$

$$\frac{\partial}{\partial x_2} p(x_1,x_2,x_3,x_4,x_5) = \sum_{i=0}^{3} \sum_{j=1}^{3} d_{j,i}\, j\, \tilde{x}_2^{\,j-1} \tilde{x}_1^{\,i}, \tag{4.28}$$

$$\frac{\partial}{\partial x_3} p(x_1,x_2,x_3,x_4,x_5) = \sum_{i=0}^{3} \sum_{j=0}^{3} \sum_{k=1}^{3} c_{k,j,i}\, k\, \tilde{x}_3^{\,k-1} \tilde{x}_2^{\,j} \tilde{x}_1^{\,i}, \tag{4.29}$$

$$\frac{\partial}{\partial x_4} p(x_1,x_2,x_3,x_4,x_5) = \sum_{i=0}^{3} \sum_{j=0}^{3} \sum_{k=0}^{3} \sum_{l=1}^{3} b_{l,k,j,i}\, l\, \tilde{x}_4^{\,l-1} \tilde{x}_3^{\,k} \tilde{x}_2^{\,j} \tilde{x}_1^{\,i}, \tag{4.30}$$

$$\frac{\partial}{\partial x_5} p(x_1,x_2,x_3,x_4,x_5) = \sum_{i=0}^{3} \sum_{j=0}^{3} \sum_{k=0}^{3} \sum_{l=0}^{3} \sum_{m=1}^{3} a_{m,l,k,j,i}\, m\, \tilde{x}_5^{\,m-1} \tilde{x}_4^{\,l} \tilde{x}_3^{\,k} \tilde{x}_2^{\,j} \tilde{x}_1^{\,i} \tag{4.31}$$

with the auxiliary variables evaluated by the Horner scheme

$$b_{l,k,j,i} := \sum_{m=0}^{3} a_{m,l,k,j,i}\, \tilde{x}_5^m, \tag{4.32}$$

$$c_{k,j,i} := \sum_{l=0}^{3} b_{l,k,j,i}\, \tilde{x}_4^l, \tag{4.33}$$

$$d_{j,i} := \sum_{k=0}^{3} c_{k,j,i}\, \tilde{x}_3^k, \tag{4.34}$$

$$e_i := \sum_{j=0}^{3} d_{j,i}\, \tilde{x}_2^j. \tag{4.35}$$

This ansatz finally leads to 2038 real-real multiplications, 2038 real-real additions and 682 integer-real multiplications or in sum 4758 FLOPs. In contrast, an independent evaluation of all partial derivatives requires 10240 FLOPs. The additional memory demand for the helping variables is 2720 bytes for double precision values.

4.4 Multi body dynamics and electrical machines

The behavior of electrical machines is mainly influenced by the drive controller. Thus, embedding electrical machines into an MBD-simulation environment requires the modeling of the complete electrical powertrain. This leads to a nonlinear electrical circuit and thus a system of nonlinear ordinary differential equations (ODE). This ODE system has to be solved additionally to the mechanical ODE system. Due to typically different time scales between mechanical and electrical systems and the time discrete behavior of digital drive controllers, an independent solver for the electrical circuit is recommended. Furthermore, the interaction of more than one solver requires the definition of a master solver. The MBD-solver used in this work can only act as master, thus, the electrical solver must be the slave. Hence, it becomes part of the nonlinear iteration loop of the master. This leads to a basic solver structure as sketched in Fig. 4.12a.

The time steps of the master solver are indexed with I. The input for the electrical solver are the new simulation time $t^{[I+1]}$, the position vector $\mathbf{x}^{[I+1]}$ and velocity vector $\dot{\mathbf{x}}^{[I+1]}$ for the bodies (rotor and stator) used for the mechanical model of the electrical machine. The output are in general the resulting forces $\mathbf{F}^{[I+1]}$ and torques $\boldsymbol{\tau}^{[I+1]}$ acting on these bodies. Furthermore, control signals to the master simulation control and a data bus for the electrical output quantities to the result logger are required. The control signals allow an intervention to the master simulation control and the time step calculation. Error handling (for example convergence problems of the electrical circuit) or the handling of special state events that necessitate the evaluation of the mechanical system at specific simulation times can be realized by this mechanism.

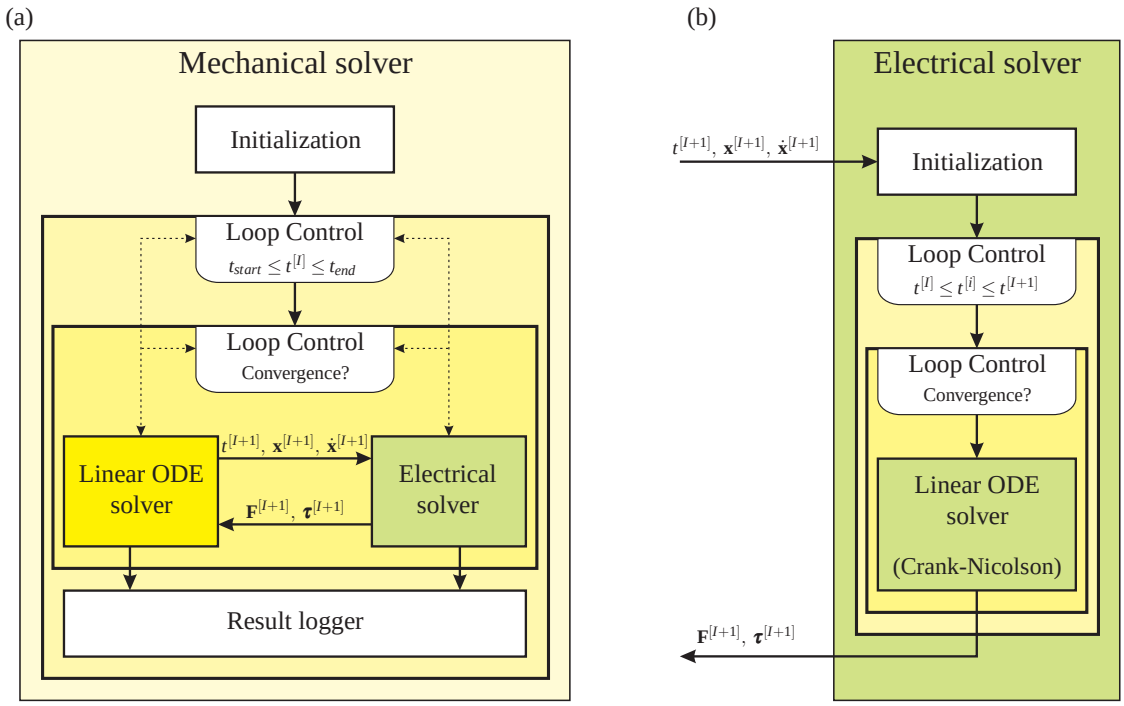

Figure 4.12: Solver topology: (a) Overview of the mechanical solver for the MBD system. It consists of a time loop with a time step control mechanism and a nonlinear iteration loop with a convergence test. The solver for the electrical network is embedded in the nonlinear iteration loop. Thus the mechanical solver becomes the master of this system of coupled solvers. (b) Overview of the electrical circuit solver. It also consists of an individual time loop with a sub-time step control mechanism and a nonlinear iteration loop. The ODE system of the electrical circuit is solved using the Crank-Nicolson method, see [41].

The electrical solver itself consists of an independent time loop and a nonlinear iteration loop as shown in Fig. 4.12b. The independent time loop is indexed with i and allows intermediate sub-time steps for the electrical network. Additional intermediate position and velocity vectors are required for this oversampling. A constant acceleration in the actual time interval $t^{[I]}$ to $t^{[I+1]}$ is assumed for its calculation:

$$\ddot{\mathbf{x}}^{[I]} := \frac{1}{t^{[I+1]} - t^{[I]}} \left(\dot{\mathbf{x}}^{[I+1]} - \dot{\mathbf{x}}^{[I]} \right). \tag{4.36}$$

This assumption is valid under the prerequisite of the mechanical solution being accurate.

For intermediate position and velocity vectors at the time $t^{[i]}$ this leads to

$$\Delta t := t^{[i]} - t^{[I]}, \tag{4.37}$$

$$\dot{\mathbf{x}}^{[i]} = \dot{\mathbf{x}}^{[I]} + \ddot{\mathbf{x}}^{[I]}\Delta t, \tag{4.38}$$

$$\mathbf{x}^{[i]} = \mathbf{x}^{[I]} + \dot{\mathbf{x}}^{[I]}\Delta t + \ddot{\mathbf{x}}^{[I]}\frac{\Delta t^2}{2}, \tag{4.39}$$

with $t^{[I]} \leq t^{[i]} \leq t^{[I+1]}$. For every sub-time step, nonlinearity is considered by the iteration loop. In case of convergence, the next sub-time step $t^{[i+1]}$ is evaluated until the end time $t^{[I+1]}$ is reached.

The ODE system in (4.3) is solved using a generalized Euler method. This method belongs to the family of finite difference methods and is a semi-implicit Euler method. It has been chosen because the FEM tool used applies the same time integration method and thus a direct comparison between FE and FE-based simulations is possible. However, in general any other Runge-Kutta method or linear multistep method can be used instead.

For the initial value problem

$$\dot{y}(t) = f(t, y(t)) \text{ with } y(t_0) = y_0, \tag{4.40}$$

the generalized Euler method can be written as

$$\dot{y}(t) \approx \frac{y(t+\Delta t) - y(t)}{\Delta t} = \Theta f(t+\Delta t, y(t+\Delta t)) + (1-\Theta) f(t, y(t)), \tag{4.41}$$

with the weight Θ and $0 \leq \Theta \leq 1$. For $\Theta = 0$ this method is the explicit forward Euler method and for $\Theta = 1$ this ansatz coincides with the implicit backward Euler method. Any intermediate value leads to a semi-implicit ansatz as for example the Crank-Nicolson method with $\Theta = 0.5$.

The ODE system (4.3) can be rewritten in vectorial notation as

$$\mathbf{v} = \mathbf{v}_{Cu} + \partial_{\alpha_{Rot}} \boldsymbol{\psi} \frac{d\alpha_{Rot}}{dt} + \mathrm{J}_{\boldsymbol{\psi}}(\mathbf{i}) \frac{d\mathbf{i}}{dt}, \tag{4.42}$$

with the input voltages $\mathbf{v}$, the resistive voltage drop $\mathbf{v}_{Cu}$, the current feed state vector $\mathbf{i}$, the vector for all coil flux linkages $\boldsymbol{\psi} = f(\alpha_{Rot}, \mathbf{i})$ and the Jacobian matrix $\mathrm{J}_{\boldsymbol{\psi}}(\mathbf{i})$ for $\boldsymbol{\psi}$ with respect to $\mathbf{i}$. Note that the mechanical position α_{Rot} and velocity $\omega = \frac{d\alpha_{Rot}}{dt}$ in (4.42) are input quantities from the mechanical solver. Thus, the ODE system has to be solved only for the current feed state variables and the generalized Euler method for (4.42) can be written as

$$\begin{aligned} \mathrm{J}_{\boldsymbol{\psi}}(\mathbf{i})^{[i+\Theta]} \frac{\mathbf{i}^{[i+1]} - \mathbf{i}^{[i]}}{t^{[i+1]} - t^{[i]}} = \Theta \left(\mathbf{v}^{[i+1]} - \mathbf{v}_{Cu}^{[i+1]} - \partial_{\alpha_{Rot}} \boldsymbol{\psi}^{[i+1]} \omega^{[i+1]} \right) + \\ (1-\Theta) \left(\mathbf{v}^{[i]} - \mathbf{v}_{Cu}^{[i]} - \partial_{\alpha_{Rot}} \boldsymbol{\psi}^{[i]} \omega^{[i]} \right). \end{aligned} \tag{4.43}$$

This equation can be rewritten as

$$\mathrm{J}_{\boldsymbol{\psi}}(\mathbf{i})^{[i+\Theta]} \frac{\mathbf{i}^{[i+1]} - \mathbf{i}^{[i]}}{t^{[i+1]} - t^{[i]}} = \mathbf{v}^{[i+\Theta]} - \mathbf{v}_{Cu}^{[i+\Theta]} - \partial_{\alpha_{Rot}} \boldsymbol{\psi}^{[i+\Theta]} \omega^{[i+\Theta]}, \tag{4.44}$$

with the weighted rotor position $\alpha_{Rot}^{[i+\Theta]}$ defined as

$$\alpha_{Rot}^{[i+\Theta]} := \Theta \alpha_{Rot}^{[i+1]} + (1-\Theta)\, \alpha_{Rot}^{[i]}. \tag{4.45}$$

The weighted quantities for $\mathbf{i}$, $\mathbf{v}$ and $\mathbf{v}_{Cu}$ in (4.44) are defined in a similar way. It is mentioned that all look-up tables for the flux linkages can be directly evaluated at the weighted parameters $\alpha_{Rot}^{[i+\Theta]}$ and $\mathbf{i}^{[i+\Theta]}$. Thus, a weighting as defined in (4.45) is not necessary for the flux linkages.

4.5 Workflow for validation

In this subsection, the validation workflow for the FE-based model is discussed. Note that no comparison with measurements is required for this purpose. The validation shall only show the equivalence between the FE model and the FE based circuit model. Therefore, the FE based circuit model is compared with a corresponding FE machine model (reference model). Transient FEM simulations with motion are carried out for this purpose. To simplify the FE model, the rotor position and the phase voltages or currents are used as input for the FEM simulation. Thereby, the extensive modeling and simulation of the complete system including the electrical power train, drive controller and mechanical system is avoided. The selected validation flow using the example of a permanent magnet synchronous machine is shown in Fig. 4.13.

For validation, an MBD-model (test bed) including the FE based machine model is set up. This model includes the mechanical system as well as the electrical power train. Several simulations with different configurations are carried out. All input and output quantities of the FE based model are logged during these simulations. The input quantities of the FE-based model (rotor position and terminal voltages or currents) are also used as input for the reference FEM simulations.

Depending on the FEM simulation setup, three different investigations can be done:

- Simulation without time integration: Rotor position and machine currents from the MBD simulation are used as input for the FEM simulation. Hereby, the interpolation error can be investigated.

- Simulation with time integration but without eddy current domains: Rotor position and terminal voltages from the MBD simulation are used as input for the FEM simulation, as shown in Fig. 4.13. Furthermore, the FE model is initialized with the machine currents by a magnetostatic simulation. Thus, any transient effects are prevented during start up. Under the assumption of a correct implementation of the FE

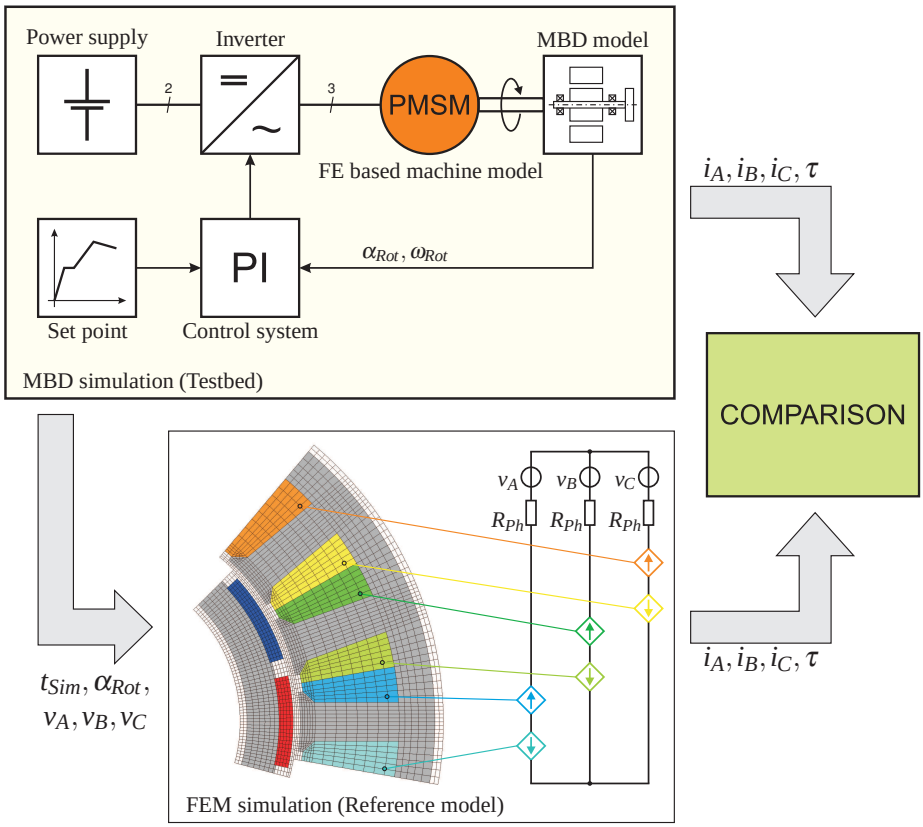

Figure 4.13: Workflow for validation of the FE based circuit model (orange). A FEM reference simulation with t_{Sim}, α_{Rot}, v_A, v_B, v_C as input is carried out. The validation is done by comparison of the machine currents i_A, i_B, i_C and the machine torque τ.

based circuit model, any variations of the simulation output are caused by the interpolation error and different time integration schemes. Thus, a direct comparison of the output quantities can be done. This simulation setup is used for the validation of the FE based model.

- Simulation with eddy current domains: Rotor position and machine terminal voltages are used as input. This FE model corresponds best to a real machine, thus any measurements should be compared with this setup. However, due to the fact that eddy currents are not covered by the FE-based circuit model approach, a direct comparison is not meaningful. However, this approach can be used for error estimation purposes.

Examples for the validation using this workflow will be presented in the chapter 5.

5 BASIC MODELS FOR VARIOUS MACHINES

In the previous chapter, the FE-based circuit model approach was presented, several design decisions were discussed and the validation workflow was described. In this chapter the application of the FE based circuit model approach to the basic machine types is presented. These machine types are the permanent magnet synchronous machine (PMSM), the reluctance machine (RM), the electrically excited synchronous machine (EESM) and the wound rotor induction machine (WRIM). With respect to the FE based modeling technique, all these machine types differ only in the number of required variables for parameterizing the characteristic curves.

The results of this chapter have been published in [61] and [62].

5.1 Permanent magnet synchronous machines

Permanent magnet synchronous machines are widely used in electrical drives. They have typically a high torque density and high power efficiency. Both are mainly due to the use

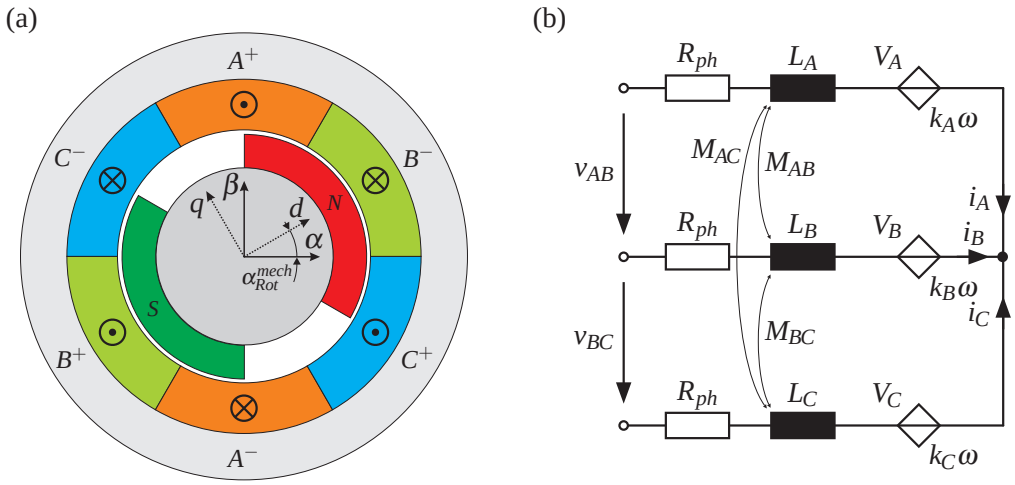

Figure 5.1: Permanent magnet synchronous machine. (a) Topology: Stator with the coil system and rotor with the permanent magnets. (b) Circuit of the stator coil system in Y-connection with isolated star point. The influence of the permanent magnets is considered by the additional rotational speed dependent voltage sources V_A, V_B and V_C. All inductances L_A, L_B, L_C, M_{AB}, M_{AC}, M_{BC} and the parameters k_A, k_B, k_C are functions of the rotor position α_{Rot} and the current feed state vector $\mathbf{i} := (i_d, i_q)$.

of permanent magnets for the main flux generation. Thus, no excitation coil and hence no excitation power is required. Moreover, the use of neodymium magnets results in very high main fluxes in relation to the construction volume of the machine. However, due to the use of rare earth metals, these machines are typically expensive. Besides, they are more damageable than electrically excited machines because the magnets easily demagnetize at higher temperatures or wrong stator current feed.

The topology of such machines is shown in Fig. 5.1.a. The stator carries a three-phase coil system that is typically in Y-connection with isolated star point. This is due to the fact that this machine type is mainly inverter fed. Thus, the star point is not required for stabilizing phase symmetry as typically used in generator applications with unbalanced load. Furthermore, an isolated star point prevents any zero-current i_0 in the $dq0$-system. Thus, the power efficiency is increased because the losses produced by this current are avoided. The particular design of the stator and the coils (distributed windings versus tooth coils) has no effect on the implementation of the FE based circuit model. Due to symmetry of all magnetic pole pairs, the circuitry of the coils per phase (serial and parallel branches) does not influence the FE based circuit model. All effects are fully covered by the look-up tables.

The rotor holds the permanent magnets. Depending on the location of the magnets two rotor designs can be distinguished. These are the design with surface mounted magnets as shown in Fig. 5.2.a and the design with interior magnets as shown in Fig. 5.2.b. Basically, both designs have slightly different operating characteristics. Machines with surface mounted magnets have approximately similar magnetic reluctances in d-axis and q-axis whereas machines with interior magnets have different magnetic reluctances in these two directions. However, the particular rotor design has again no influence on the FE based circuit model. The magnetic reluctances for both axes as well as any saturation effects are covered by the look-up tables.

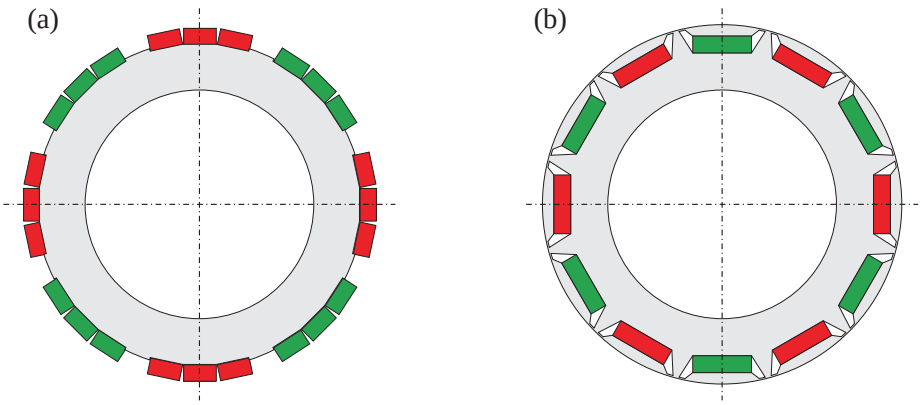

Figure 5.2: Rotor design overview. (a) Rotor with surface mounted permanent magnets and four magnetic pole pairs. (b) Rotor with interior permanent magnets and six magnetic pole pairs

5.1.1 Implementation of the FE based circuit model

Although the equivalent circuit for this machine, as shown in Fig. 5.1.b, includes additional voltage sources for modeling the effect of the permanent magnets, this machine is described by the same equation (4.6) as the hypothetical machine in chapter 4.

The scalar parameters of the model are the phase resistance R_{ph} and the number of magnetic pole pairs n_{mp}. The model parameters defined by look-up tables are the phase to phase flux linkage ψ_{AB} and the machine torque τ. The input of the model are the mechanical rotor position α_{Rot}^{mech}, the mechanical angular velocity ω_{mech} and the machine phase to phase voltages v_{AB}, v_{BC}. The parameter variables are the electrical rotor position $\alpha_{Rot} = n_{mp}\alpha_{Rot}^{mech}$, the direct current i_d and the quadrature current i_q. The output of the model are the torque τ and the machine phase currents $\mathbf{i}_{ABC}$.

Thus, the complete model can be written as

$$\begin{bmatrix} \partial_{i_d}\psi_{AB} & \partial_{i_q}\psi_{AB} \\ \partial_{i_d}\psi_{BC} & \partial_{i_q}\psi_{BC} \end{bmatrix} \begin{pmatrix} \frac{di_d}{dt} \\ \frac{di_q}{dt} \end{pmatrix} = \begin{pmatrix} v_{AB} \\ v_{BC} \end{pmatrix} - R_{ph} \begin{pmatrix} i_{AB} \\ i_{BC} \end{pmatrix} - \begin{pmatrix} \partial_{\alpha_{Rot}}\psi_{AB} \\ \partial_{\alpha_{Rot}}\psi_{BC} \end{pmatrix} n_{mp}\omega_{mech}, \tag{5.1}$$

$$\mathbf{i}_{ABC} = \mathbf{C}^{-1}\mathbf{P}\left(\alpha_{Rot}\right)^{-1} \begin{pmatrix} i_d \\ i_q \end{pmatrix}, \tag{5.2}$$

$$\tau = \tau\left(\alpha_{Rot}, i_d, i_q\right) \tag{5.3}$$

where ψ_{BC} is the evaluation of the look-up table for ψ_{AB} at the rotor position $\alpha_{Rot} - \frac{2\pi}{3}$. The ODE system is solved using the generalized Euler method as shown in (4.44).

Note that the interconnection of the coils belonging to one phase for machines with $n_{mp} > 1$ has no influence on the model. For a series connection, the same current in all coils is enforced by default. Due to the assumed symmetry, the same current flows in all branches in case of a parallel connection. The higher losses of a machine design with unbalanced parallel coils makes this practically irrelevant. Eccentricity effects are not considered by this model.

Furthermore, it should be mentioned that in case of a connected star point, the additional current feed state variable i_0 and a third voltage equation are required as presented for the switched reluctance machine in (5.5) in the section 5.2.

5.1.2 Validation of the machine model

The validation of the machine model was carried out according to the workflow described in section 4.5. The model parameters ψ_{AB} and τ were sampled using magnetostatic FEM simulations. Several application cases have been investigated employing the machine model in transient MBD simulations. The results have been compared with those of transient FEM simulations. In this subsection, the machine used for the comparison, the FE model and some results of the comparisons are presented.

The FE model used for the validation of the PMSM is shown in Fig. 5.3. This machine has six magnetic pole pairs and buried magnets on the rotor. Its nominal power is 15 kW,

the nominal speed is 5000 rpm. The corresponding look-up table parameters ψ_{AB} and τ are shown in Fig. 5.4 and Fig. 5.5. These parameters were sampled with various sampling rates N_α for rotor position, N_{id} for direct current and N_{iq} for quadrature current to investigate the influence of these sampling rates. A comparison is shown in table 5.1 including the number of FEM simulations N_{FEM}, the required calculation cost t_{FEM} without parallelization and the required memory demand MD for both look-up tables.

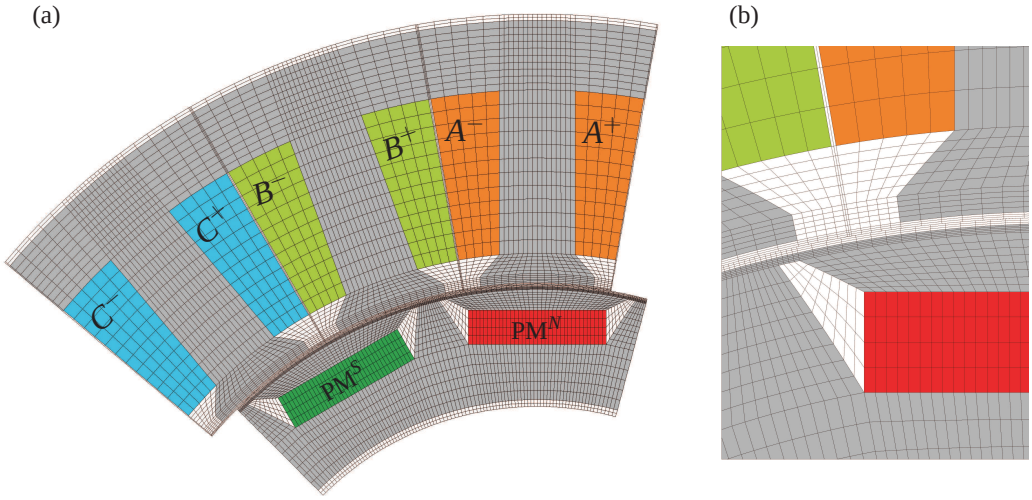

Figure 5.3: FE model of the PMSM under investigation. (a) The PMSM has six symmetric magnetic pole pairs. For the FE model only one magnetic pole pair (segment of 60°) was modeled. Periodic boundary conditions have been used at the cutting planes. (b) Special attention was paid to the mesh of the air gap to prevent numerical errors caused by the mesh and the constraint equations for coupling rotor and stator.

It should be mentioned that for this machine only an interval of $60^{\circ\mathrm{E}}$ was sampled. This is sufficient to sample a full period of the first harmonic of the (cogging-) torque. Furthermore, this interval is sufficient to reconstruct a full electric period of the flux linkage by concatenating the flux linkages sampled for the three phases. Without down sampling this approach leads to a six times higher memory demand for the flux linkage dataset than for the torque dataset.

Note that due to symmetry between positive and negative half-wave of the flux linkage

$$\psi\left(\alpha_{Rot}\right) = -\psi\left(\alpha_{Rot} + 180^{\circ\mathrm{E}}\right), \tag{5.4}$$

the required interval for the flux linkage dataset is only $180^{\circ\mathrm{E}}$. Notice further that a similar reduction of the rotor position interval for the torque dataset is not possible. However, for the torque dataset, its symmetry with respect to the torque generating current i_q can be utilized. Nevertheless, within this work neither the symmetry of the flux linkage dataset

Table 5.1: Comparison between several sampling rate configurations.

Setup	N_α (-)	N_{id} (-)	N_{iq} (-)	N_{FEM} (-)	$\Delta\alpha_{Rot}$ (°E)	t_{FEM} (min)	MD (MByte)
SET-1	60	17	11	11200	1	1557	32.8
SET-2	15	17	11	2805	4	389	8.20
SET-3	15	9	11	1485	4	206	4.10
SET-4	10	17	11	1870	6	260	5.46
SET-5	10	9	11	990	6	137	2.73
SET-6	10	17	6	1020	6	141	2.73

nor the symmetry of torque dataset has been utilized to decrease the memory demand of the look-up tables.

Fig. 5.6 shows an overview of the transient simulation carried out using the FE-based circuit model. The three grey marked time windows (Detail-1, Detail-2 and Detail-3) define the simulation intervals that were also simulated using FEM. The figures Fig. 5.7 and Fig. 5.8 show a direct comparison of the machine currents and the machine torque between FE-model and FE-based circuit model. Obviously, all curves are in a very good agreement and the proper functioning of the model has been thus proved.

Note that, for each FE simulation, a proper initialization of the FE model is required. For Detail-1 this is easy to achieve because the machine starts from stop and without any current feed. For Detail-2 and Detail-3 the same current feed and rotor speed as calculated from the FE-based circuit model need to be impressed. However, slightly differences caused by the non-linear FE solver occur during the first 30 ms of the FE simulations for Detail-2 and Detail-3.

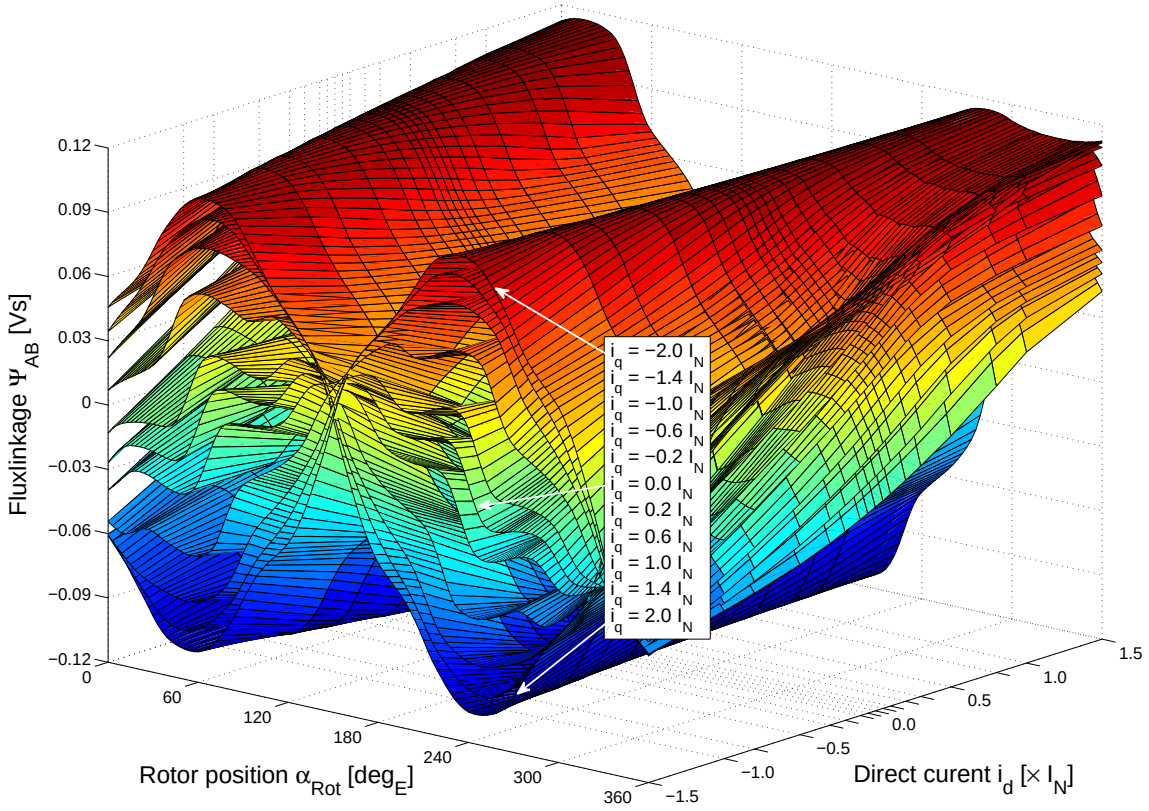

Figure 5.4: Set of characteristic curves for the phase to phase flux linkage ψ_{AB}. An intervall of 360°E for the rotor position is required to cover a full period of this quantity. Thus, this dataset was concatenated from the three phase flux linkages ψ_A, ψ_B and ψ_C sampled for an interval of 60°E. Direct and quadrature current are normalized with the nominal current I_N of the machine.

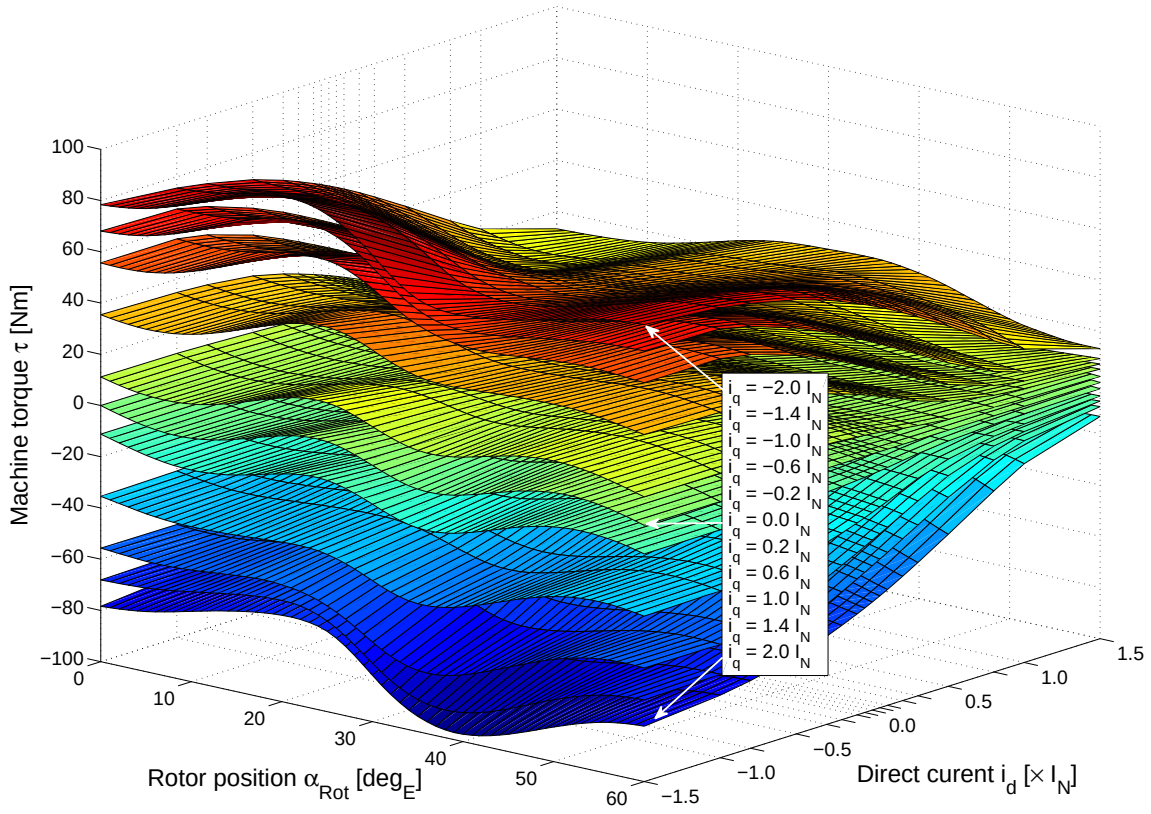

Figure 5.5: Set of characteristic curves for the machine torque τ. Due to the six magnetic pole pairs of the machine an interval of $60^{\circ\mathrm{E}}$ for the rotor position is sufficient to cover a full period of this quantity.

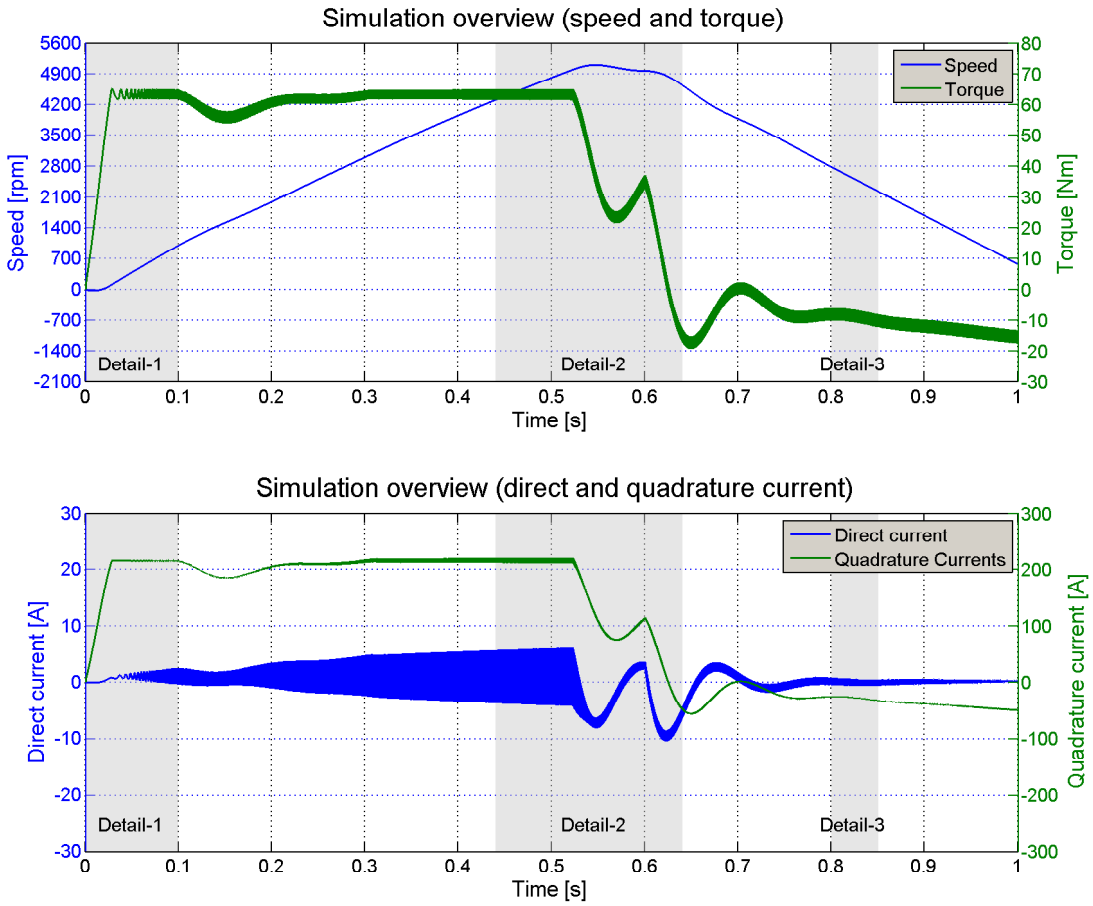

Figure 5.6: Overview of transient simulation. The upper diagram shows machine speed (blue) and the corresponding machine torque (green). The lower diagram shows direct (blue) and quadrature (green) current. Furthermore, the three time windows used for comparison with FEM are shown (grey).

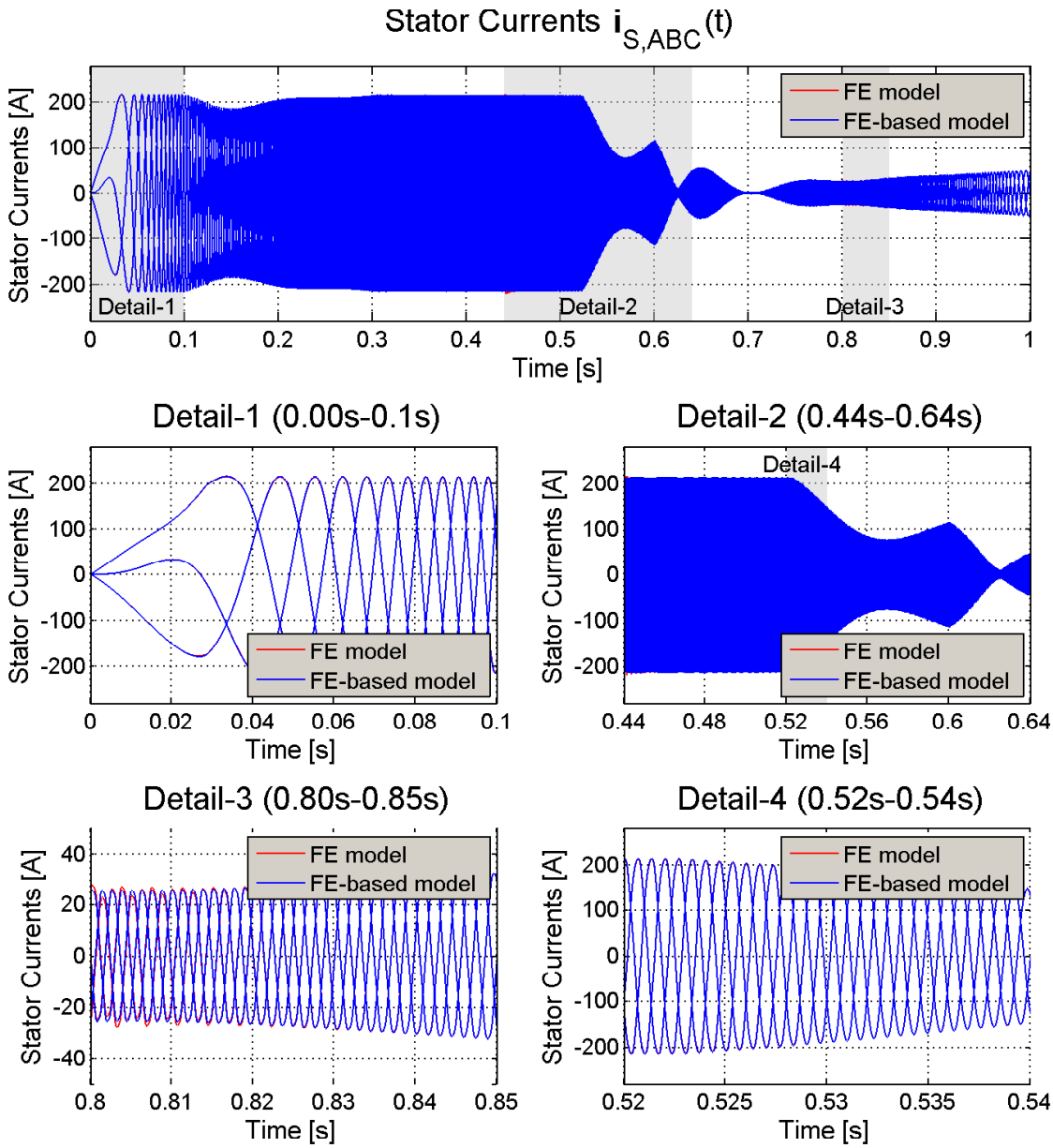

Figure 5.7: Comparison of the stator currents between FE model and FE-based circuit model for a transient simulation. The diagrams show a validation example. For all details, a separate FEM simulation has been carried out. All curves are in a very good agreement except small differences at the starting of Detail-2 and Detail-3. This error is caused by the initialization of the FEM model and vanishes after a short simulation period.

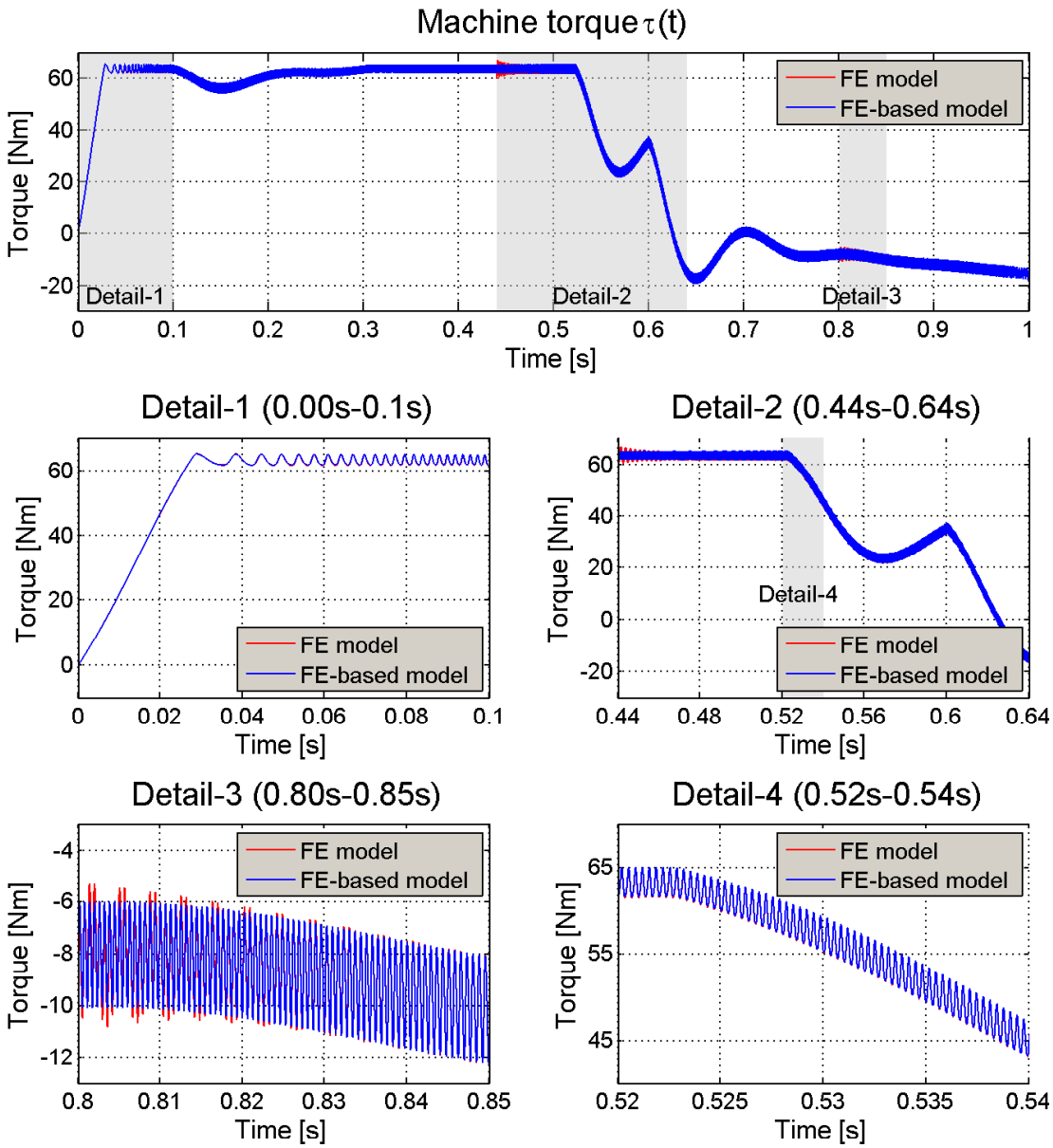

Figure 5.8: Comparison of the machine torque between FE model and FE-based circuit model for a transient simulation. The diagrams show a validation example. For all details, a separate FEM simulation has been carried out. All curves are in a very good agreement except small differences at the starting of Detail-2 and Detail-3. This error is caused by the initialization of the FEM model and vanishes after a short simulation period.

5.2 Reluctance machines

Reluctance machines can be categorized into synchronous reluctance machines and switched reluctance machines. From a machine design point of view, synchronous reluctance machines have the same number of magnetic pole pairs on rotor and stator whereas switched reluctance machines have a different number of magnetic poles on rotor and stator. This leads to a completely different control scheme for the two machine types.

5.2.1 Synchronous reluctance machines

Synchronous reluctance machines, as shown in Fig. 5.9, have typically a three-phase coil system in Y-connection with isolated star point on the stator. Compared with a PMSM, this machine has no permanent magnets for creating the magnetic main flux. Therefore, any magnetic flux in the machine must be generated by currents flowing in the stator coil system.

The FE based circuit model for this machine type is identical with the PMSM model of section 5.1. The same parameter variables and look-up table quantities are used and the same FE preprocessing workflow can be utilized.

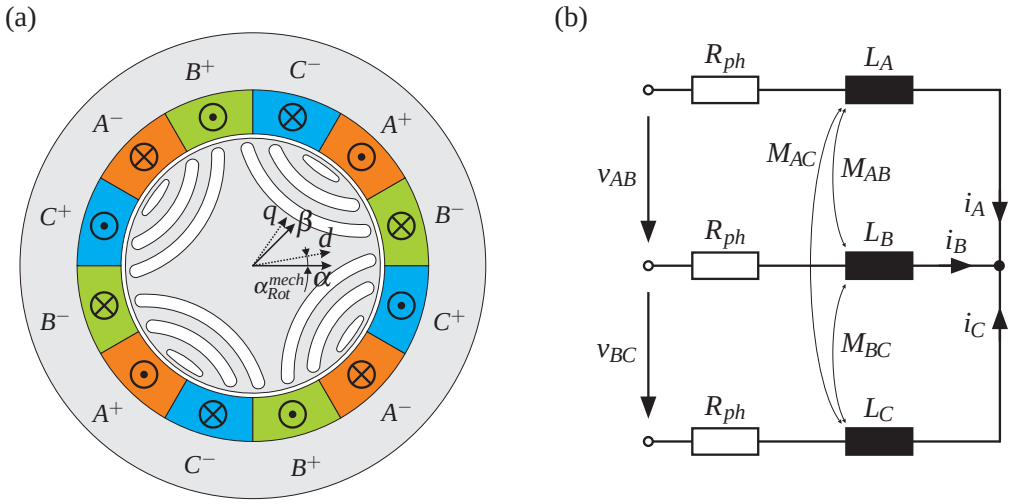

Figure 5.9: Synchronous reluctance machine. (a) Topology: Stator with the coil system and rotor for a machine with four magnetic poles. (b) Circuit of the stator coil system in Y-connection with isolated star point. All inductances L_A, L_B, L_C, M_{AB}, M_{AC}, M_{BC} are functions of the rotor position α_{Rot} and the current feed state vector $\mathbf{i} := (i_d, i_q)$.

Note: For direct operation at a power grid, synchronous reluctance machines with damper windings are used. These machines have an additional squirrel cage (similar to the induction machines) on the rotor allowing an asynchronous start up. However, this kind of reluctance machine is not in the focus of this work.

5.2.2 Switched reluctance machines

Switched reluctance machines, as exemplarily shown in Fig. 5.10 are used in electrical drives. They are very robust and cheap machines because their rotor carries no coil system. The stator typically has two or more coils that are controlled independently. This is equivalent to an unbalanced multi-phase system. For the FE based circuit model approach this leads to a phase voltage equation per coil. Furthermore, a current feed state variable for every coil is required. However, in many cases a switched reluctance machine consists

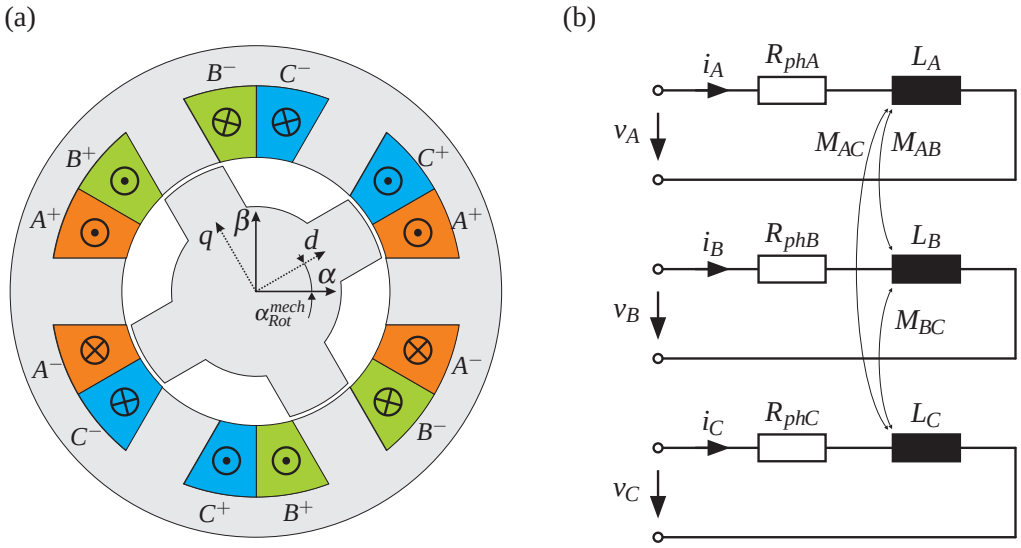

Figure 5.10: 6/4 pole switched reluctance machine. (a) Topology: Stator with one magnetic pole pair (six teeth coils) and rotor with two magnetic pole pairs (four teeth). (b) Circuit of the stator coil system. All inductances L_A, L_B, L_C, M_{AB}, M_{AC}, M_{BC} are functions of the rotor position α_{Rot} and the current feed state vector $\mathbf{i} := (i_d, i_q, i_0)$.

of two coils (e.g. stepper motors) or three coils (e.g. 6/4 pole switched reluctance machine in Fig. 5.10). Furthermore, typically the rotor of such machines has a higher number of poles and thus more symmetry planes. For example the rotor position for the machine shown in Fig. 5.10 has to be varied only in an interval of $30°^{\mathrm{E}}$, reducing the FE simulation effort during the look-up table creation.

Although the switched reluctance machine is not in the scope of this work, a FE-based circuit model for a machine with three symmetric coils is presented because this model is identical with the model for a PMSM with connected star point. This model is parameterized by the scalar parameters for the coil resistance per phase R_{ph} and the number of magnetic pole pairs n_{mp} of the stator. The model parameters defined by look-up tables are the phase flux linkage ψ_A and the machine torque τ. The input of the model are the rotor position α_{Rot}^{mech}, the rotor speed ω^{mech} and the phase voltages $\mathbf{v_{ABC}}$. The state of the machine is defined by the rotor position α_{Rot} and the currents i_d, i_q and i_0. The output of

the model are the machine torque τ and the phase currents $\mathbf{i}_{ABC}$.

Thus, the complete model can be described as:

$$\begin{bmatrix} \partial_{i_d}\psi_A & \partial_{i_q}\psi_A & \partial_{i_0}\psi_A \\ \partial_{i_d}\psi_B & \partial_{i_q}\psi_B & \partial_{i_0}\psi_B \\ \partial_{i_d}\psi_C & \partial_{i_q}\psi_C & \partial_{i_0}\psi_C \end{bmatrix} \begin{pmatrix} \frac{di_d}{dt} \\ \frac{di_q}{dt} \\ \frac{di_0}{dt} \end{pmatrix} = \begin{pmatrix} v_A \\ v_B \\ v_C \end{pmatrix} - R_{ph} \begin{pmatrix} i_A \\ i_B \\ i_C \end{pmatrix} - \begin{pmatrix} \partial_{\alpha_{Rot}}\psi_A \\ \partial_{\alpha_{Rot}}\psi_B \\ \partial_{\alpha_{Rot}}\psi_C \end{pmatrix} n_{mp}\omega_{mech}, \quad (5.5)$$

$$\mathbf{i}_{ABC} = \mathbf{C}^{-1}\mathbf{P}\left(\alpha_{Rot}\right)^{-1} \begin{pmatrix} i_d \\ i_q \\ i_0 \end{pmatrix}, \quad (5.6)$$

$$\tau = \tau\left(\alpha_{Rot}, i_d, i_q, i_0\right) \quad (5.7)$$

where ψ_B is the evaluation of the look-up table for ψ_A at the rotor position $\alpha_{Rot} - \frac{2\pi}{3}$ and ψ_C is the evaluation at $\alpha_{Rot} - \frac{4\pi}{3}$.

Notice that although all three phases of the switched reluctance machine are isolated from each other and controlled independently, the transformed currents i_d, i_q and i_0 are used as state variables for the model. Nevertheless, instead of $\mathbf{i}_{dq0}$ the phase currents $\mathbf{i}_{ABC}$ could be also used as state variables leading to

$$\begin{bmatrix} \partial_{i_A}\psi_A & \partial_{i_B}\psi_A & \partial_{i_C}\psi_A \\ \partial_{i_A}\psi_B & \partial_{i_B}\psi_B & \partial_{i_C}\psi_B \\ \partial_{i_A}\psi_C & \partial_{i_B}\psi_C & \partial_{i_C}\psi_C \end{bmatrix} \begin{pmatrix} \frac{di_A}{dt} \\ \frac{di_B}{dt} \\ \frac{di_C}{dt} \end{pmatrix} = \begin{pmatrix} v_A \\ v_B \\ v_C \end{pmatrix} - R_{ph} \begin{pmatrix} i_A \\ i_B \\ i_C \end{pmatrix} - \begin{pmatrix} \partial_{\alpha_{Rot}}\psi_A \\ \partial_{\alpha_{Rot}}\psi_B \\ \partial_{\alpha_{Rot}}\psi_C \end{pmatrix} n_{mp}\omega_{mech}, \quad (5.8)$$

$$\tau = \tau\left(\alpha_{Rot}, i_A, i_B, i_C\right). \quad (5.9)$$

However, the former choice using $\mathbf{i}_{dq0}$ has practical advantages because both the simulation control scheme for the preprocessing and all machine models use transformed currents. Thus, all macros and functions need to be extended only, and the basic structure stays the same.

5.3 Electrically excited synchronous machines

Within this work only inverter fed electrically excited synchronous machines (EESM) are considered. The topology of this machines type is shown in Fig. 5.11. These machines consist of a stator with a three phase coil system and a rotor with an excitation coil. They are mainly used in electric drives. In these applications, the stator coil system is typically in Y-connection with isolated star point. One can distinguish between salient pole (as shown in Fig. 5.11) and non-salient pole rotors. However, the FE based circuit model approach is the same for both rotor designs.

Notice that electrically excited synchronous machines with a damper coil system are not covered by this model approach. The damper coil system can be assumed as additional squirrel cage coil. Such a coil leads for the FE-based circuit model approach to several problems as discussed in sub-section 5.4.1.

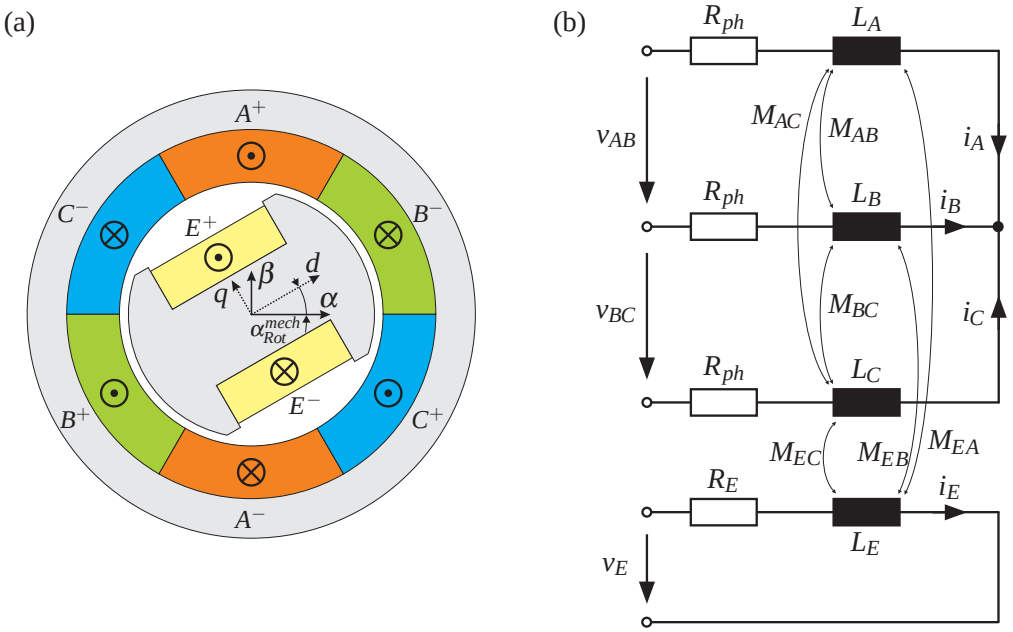

Figure 5.11: Electrically excited synchronous machine. (a) Topology: Stator with three-phase coil system in Y-connection with isolated star point and rotor with excitation coil system. (b) Circuit of the stator coil system and the isolated rotor coil system. All inductances L_A, L_B, L_C, L_E, M_{AB}, M_{AC}, M_{BC}, M_{EA}, M_{EB}, M_{EC} are functions of the rotor position α_{Rot} and the current feed state vector $\mathbf{i} := (i_d, i_q, i_E)$.

5.3.1 Implementation of the FE based circuit model

The model for an electrically excited synchronous machine as shown in Fig. 5.11 is parameterized by the scalar parameters for the stator phase resistance R_{ph}, the number of

magnetic pole pairs n_{mp} and the resistance of the excitation coil R_E. The look-up table parameters are the phase to phase flux linkage ψ_{AB}, the flux linkage of the excitation coil ψ_E and the machine torque τ. The mechanical input of the model are the rotor position α_{Rot}^{mech} and the rotor speed ω^{mech}. The electrical input are the phase to phase voltages v_{AB}, v_{BC} and the excitation voltage v_E. The state of the machine is defined by rotor position α_{Rot}, direct current i_d, quadrature current i_q and the excitation current i_E. The output of the model are the machine torqe τ, the phase currents $\mathbf{i}_{ABC}$ and the excitation current i_E.

The complete model can be described as:

$$\begin{bmatrix} \partial_{i_d}\psi_{AB} & \partial_{i_q}\psi_{AB} & \partial_{i_E}\psi_{AB} \\ \partial_{i_d}\psi_{BC} & \partial_{i_q}\psi_{BC} & \partial_{i_E}\psi_{BC} \\ \partial_{i_d}\psi_E & \partial_{i_q}\psi_E & \partial_{i_E}\psi_E \end{bmatrix} \begin{pmatrix} \frac{di_d}{dt} \\ \frac{di_q}{dt} \\ \frac{di_E}{dt} \end{pmatrix} = \begin{pmatrix} v_{AB} \\ v_{BC} \\ v_E \end{pmatrix} - \begin{pmatrix} R_{ph}(i_A - i_B) \\ R_{ph}(i_B - i_C) \\ R_E i_E \end{pmatrix} - \begin{pmatrix} \partial_{\alpha_{Rot}}\psi_{AB} \\ \partial_{\alpha_{Rot}}\psi_{BC} \\ \partial_{\alpha_{Rot}}\psi_E \end{pmatrix} n_{mp}\omega_{mech}, \quad (5.10)$$

$$\mathbf{i}_{ABC} = \mathbf{C}^{-1}\mathbf{P}(\alpha_{Rot})^{-1} \begin{pmatrix} i_d \\ i_q \end{pmatrix}, \quad (5.11)$$

$$\tau = \tau(\alpha_{Rot}, i_d, i_q, i_E) \quad (5.12)$$

where ψ_{BC} is the evaluation of the look-up table for ψ_{AB} at the rotor position $\alpha_{Rot} - \frac{2\pi}{3}$.

This model could be extended for machines with connected star point using the additional current feed state variable i_0 leading to

$$\begin{bmatrix} \partial_{i_d}\psi_A & \partial_{i_q}\psi_A & \partial_{i_0}\psi_A & \partial_{i_E}\psi_A \\ \partial_{i_d}\psi_B & \partial_{i_q}\psi_B & \partial_{i_0}\psi_B & \partial_{i_E}\psi_B \\ \partial_{i_d}\psi_C & \partial_{i_q}\psi_C & \partial_{i_0}\psi_C & \partial_{i_E}\psi_C \\ \partial_{i_d}\psi_E & \partial_{i_q}\psi_E & \partial_{i_0}\psi_E & \partial_{i_E}\psi_E \end{bmatrix} \begin{pmatrix} \frac{di_d}{dt} \\ \frac{di_q}{dt} \\ \frac{di_0}{dt} \\ \frac{di_E}{dt} \end{pmatrix} = \begin{pmatrix} v_A \\ v_B \\ v_C \\ v_E \end{pmatrix} - \begin{pmatrix} R_{ph} i_A \\ R_{ph} i_B \\ R_{ph} i_C \\ R_E i_E \end{pmatrix} - \begin{pmatrix} \partial_{\alpha_{Rot}}\psi_A \\ \partial_{\alpha_{Rot}}\psi_B \\ \partial_{\alpha_{Rot}}\psi_C \\ \partial_{\alpha_{Rot}}\psi_E \end{pmatrix} n_{mp}\omega_{mech}, \quad (5.13)$$

$$\mathbf{i}_{ABC} = \mathbf{C}^{-1}\mathbf{P}(\alpha_{Rot})^{-1} \begin{pmatrix} i_d \\ i_q \\ i_0 \end{pmatrix}, \quad (5.14)$$

$$\tau = \tau(\alpha_{Rot}, i_d, i_q, i_0, i_E) \quad (5.15)$$

where ψ_B is the evaluation of the look-up table for ψ_A at the rotor position $\alpha_{Rot} - \frac{2\pi}{3}$ and ψ_C is the evaluation at $\alpha_{Rot} - \frac{4\pi}{3}$.

5.4 Induction machines

5.4.1 Squirrel cage induction machines

Squirrel cage induction machines (SCIM) are widely used in electric drives. The rotor coil system is realized as squirrel cage coil that does not need any connections. Thus no brushes and slip rings are required. Due to their simple rotor design they are very robust. The topology of this machines type and a sketch of a squirrel cage coil are shown in Fig. 5.12.

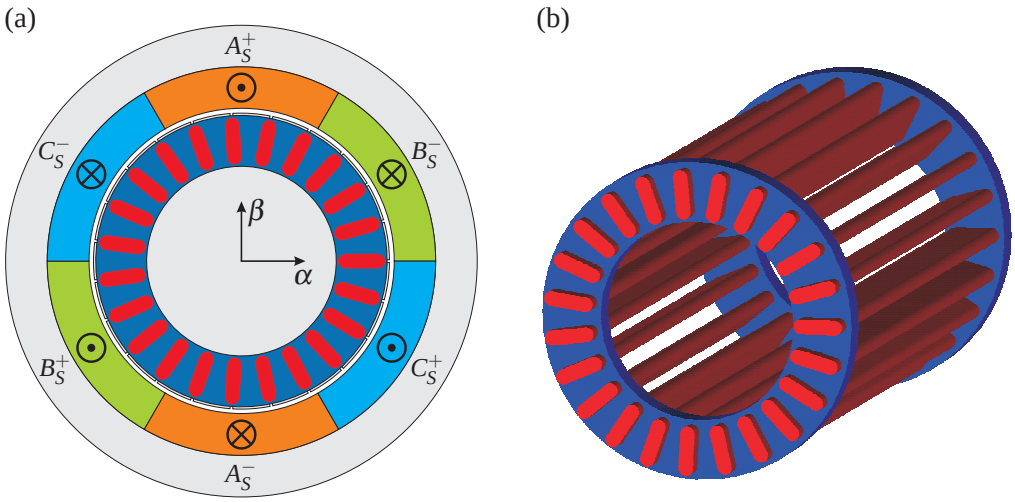

Figure 5.12: Squirrel cage induction machine (a) Topology: Stator with a three-phase coil system and rotor with squirrel cage coil. (b) Example of a squirrel cage coil.

Unfortunately, the FE-based circuit model approach presented in this work could not be applied to this machine type. This is caused by the properties of the squirrel cage coil:

- A squirrel cage coil with N bars can be regarded as an N-phase coil system whereas each bar corresponds to one phase. This leads in general to $N-1$ current feed state variables for modelling a squirrel cage with the FE-based circuit approach. This leads further to an unfeasibly high number of state variables.
- All bars of a squirrel cage coil are typically solid conductors, i.e. skin effect occurs. This influences the ohmic resistance of the bars and has an impact to the machine behavior. This effect is even utilized in machine design by shaping the bars and could not be neglected. However, eddy current effects could not be considered by magnetostatic simulations because the geometry of a corresponding equivalent conducting loop is indefinite.

This limitation of the FE-based circuit model applies to all machine types using a squirrel cage coil.

5.4.2 Wound rotor induction machines

In the past, wound rotor induction machines (WRIM) also known as rotating transformers were used for the coupling of power grids with different frequencies. Nowadays, this machine type can be found in wind power stations. In this application, the stator coil system is directly connected to the power grid, thus supplied with constant frequency. The rotor coil system is inverter fed, thus supplied with a variable frequency. By controlling the rotor supply frequency any speed changes of the rotor can be compensated. The main advantage of this system configuration is that a smaller inverter can be used compared with other system configurations. This is due to the fact that the main power flows directly from the stator the power grid and doesn't flow through the inverter.

The topology of a wound rotor induction machine is shown in Fig. 5.13.a. It has three phase coil systems on stator and rotor. Thus, additional slip rings are required to connect the rotor coil system.

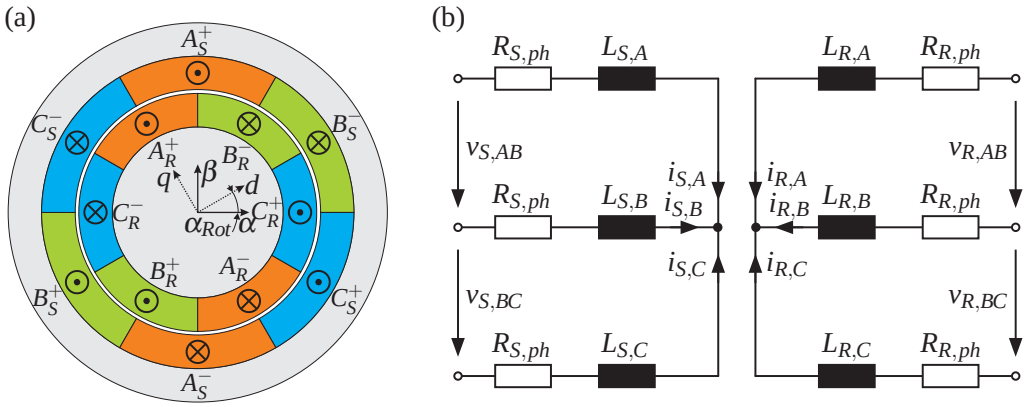

Figure 5.13: Wound rotor induction machine (a) Topology: Stator and rotor with a three-phase coil system in Y-connection and isolated star point. (b) Circuit of the stator and rotor coil system (not all 15 mutual inductances are shown to ensure clarity). All inductances are functions of the rotor position α_{Rot} and the current feed state vector $\mathbf{i} := \left(i_{S,\alpha}, i_{S,\beta}, i_{R,\alpha}, i_{R,\beta}\right)$.

Implementation of the FE based circuit model

The model for the wound rotor induction machine as shown in Fig. 5.11.b is parameterized by the scalar parameters for the phase resistance of the stator $R_{S,ph}$, the phase resistance of the rotor $R_{R,ph}$ and the number of magnetic pole pairs n_{mp}. The look-up table parameters are the stator phase to phase flux linkage $\psi_{S,AB}$, the rotor phase to phase flux linkages $\psi_{R,AB}$, $\psi_{R,BC}$ and the machine torque τ. The mechanical input of the model are rotor position α_{Rot}^{mech} and rotor speed ω_{mech}. The electrical input are the stator phase to phase voltages $v_{S,AB}$, $v_{S,BC}$ and the rotor phase to phase voltages $v_{R,AB}$, $v_{R,BC}$. The state of the machine is defined by the rotor position α_{Rot}, the transformed stator currents $i_{S,\alpha}$, $i_{S,\beta}$ and

the transformed rotor currents $i_{R,\alpha}$, $i_{R,\beta}$. A common reference system is required for all transformed quantities. Within this work, the rotor related reference system is used for this purpose. The output of the model are the machine torque τ, the stator phase currents $\mathbf{i}_{S,ABC}$ and the rotor phase currents $\mathbf{i}_{R,ABC}$.

Note that two flux linkages for the rotor coil system are required. This is a consequence of the chosen rotor related reference system where the rotor phase coils are geometrically shifted within the reference system itself. This geometrical shift could not be compensated by any rotational shift of the reference system. In other words, the flux linkages of the rotor coil system become DC-like quantities in the rotor related reference system whereby any rotor position dependency is only caused by slotting effects (see Fig. 5.19). The same situation would also occur using the stator related reference system. In that case two flux linkages for the stator coil system would become necessary.

The complete model for the WRIM can be described as:

$$\begin{bmatrix} \partial_{i_{S,\alpha}}\psi_{S,AB} & \partial_{i_{S,\beta}}\psi_{S,AB} & \partial_{i_{R,\alpha}}\psi_{S,AB} & \partial_{i_{R,\beta}}\psi_{S,AB} \\ \partial_{i_{S,\alpha}}\psi_{S,BC} & \partial_{i_{S,\beta}}\psi_{S,BC} & \partial_{i_{R,\alpha}}\psi_{S,BC} & \partial_{i_{R,\beta}}\psi_{S,BC} \\ \partial_{i_{S,\alpha}}\psi_{R,AB} & \partial_{i_{S,\beta}}\psi_{R,AB} & \partial_{i_{R,\alpha}}\psi_{R,AB} & \partial_{i_{R,\beta}}\psi_{R,AB} \\ \partial_{i_{S,\alpha}}\psi_{R,BC} & \partial_{i_{S,\beta}}\psi_{R,BC} & \partial_{i_{R,\alpha}}\psi_{R,BC} & \partial_{i_{R,\beta}}\psi_{R,BC} \end{bmatrix} \begin{pmatrix} \frac{di_{S,\alpha}}{dt} \\ \frac{di_{S,\beta}}{dt} \\ \frac{di_{R,\alpha}}{dt} \\ \frac{di_{R,\beta}}{dt} \end{pmatrix} = \begin{pmatrix} v_{S,AB} \\ v_{S,BC} \\ v_{R,AB} \\ v_{R,BC} \end{pmatrix} - \begin{pmatrix} R_{S,ph}i_{S,AB} \\ R_{S,ph}i_{S,BC} \\ R_{R,ph}i_{R,AB} \\ R_{R,ph}i_{R,BC} \end{pmatrix} - \begin{pmatrix} \partial_{\alpha_{Rot}}\psi_{S,AB} \\ \partial_{\alpha_{Rot}}\psi_{S,BC} \\ \partial_{\alpha_{Rot}}\psi_{R,AB} \\ \partial_{\alpha_{Rot}}\psi_{R,BC} \end{pmatrix} n_{mp}\omega_{mech}, \quad (5.16)$$

$$\mathbf{i}_{S,ABC} = \mathbf{C}^{-1}\mathbf{P}\left(\alpha_{Rot}\right)^{-1}\begin{pmatrix} i_{S,\alpha} \\ i_{S,\beta} \end{pmatrix}, \quad (5.17)$$

$$\mathbf{i}_{R,ABC} = \mathbf{C}^{-1}\begin{pmatrix} i_{R,\alpha} \\ i_{R,\beta} \end{pmatrix}, \quad (5.18)$$

$$\tau = \tau\left(\alpha_{Rot}, i_{S,\alpha}, i_{S,\beta}, i_{R,\alpha}, i_{R,\beta}\right) \quad (5.19)$$

where $\psi_{S,BC}$ is the evaluation of the look-up table for $\psi_{S,AB}$ at the rotor position $\alpha_{Rot} - \frac{2\pi}{3}$.

Validation of the machine model

In this subsection the FE model used for the validation and some details of the five-dimensional parameter sets are presented. Unfortunately, only design data for a squirrel cage induction machine were available. This machine has three magnetic pole pairs, a nominal power of 11 kW, a nominal voltage of 260 V and a nominal current of 47 A. Each phase consists of three coils connected in parallel. However, the design of the SCIM was adopted for the validation of the WRIM. The original stator design was taken but it was

assumed that the stator coils are connected in series. This leads to a nominal current of 15.7 A at a nominal voltage of 780 V without changing the number of windings per slot. Furthermore, the number of slots on the rotor has been increased from 44 to 48. This is necessary for keeping the symmetry of all three magnetic pole pairs for a three phase coil system. The resulting machine model is shown in Fig. 5.14.

Note, that the focus of this work is on modelling machines and not on machine design. Indeed, the machine design shown is probably not suitable for production. However, it fulfills all criteria for doing a validation of the model approach by the method described in section 4.5.

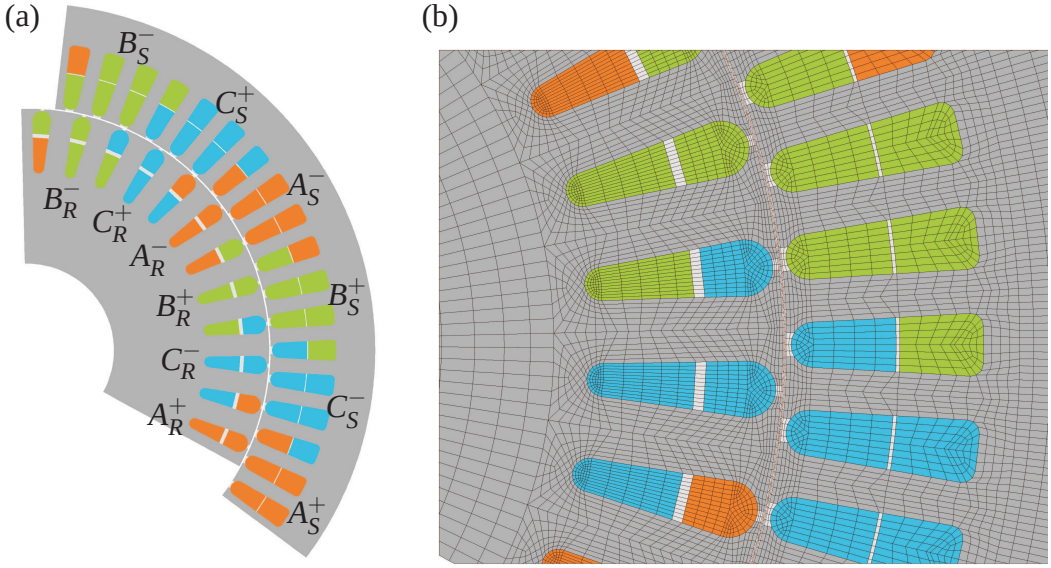

Figure 5.14: FE model of the WRIM under investigation. (a) The WRIM has three magnetic pole pairs and distributed coils on rotor and stator. One segment of 120° (one magnetic pole pair) was modeled. Periodic boundary conditions have been used at the cutting planes. (b) Detail of the model including the mesh.

The figures Fig. 5.15 to Fig. 5.20 show some details of the parameter set. The figure captions describe the curves shown. Notice that the parameter determination with FEM for this machine type is quite extensive because approximately 100.000 magnetostatic simulations are required. Depending on the FE model size and the degree of parallelization, the preprocessing needs several days or weeks. Nevertheless, this high simulation effort is more than compensated during the transient simulations with the resulting FE-based circuit model. The required simulation time for the current FE model is 12 s per time step, meanwhile the FE-based circuit model requires only 200 µs per time step. This is a speed up of approximately 60.000 for the transient simulations!

Furthermore, keep in mind that the number of time steps for typical transient system simulations is much higher than 100.000 and transient simulations can not be parallelized.

Indeed, the simulation effort for doing the transient FEM simulations required for the validation (weeks) was much higher than the effort for the preprocessing stage (days).

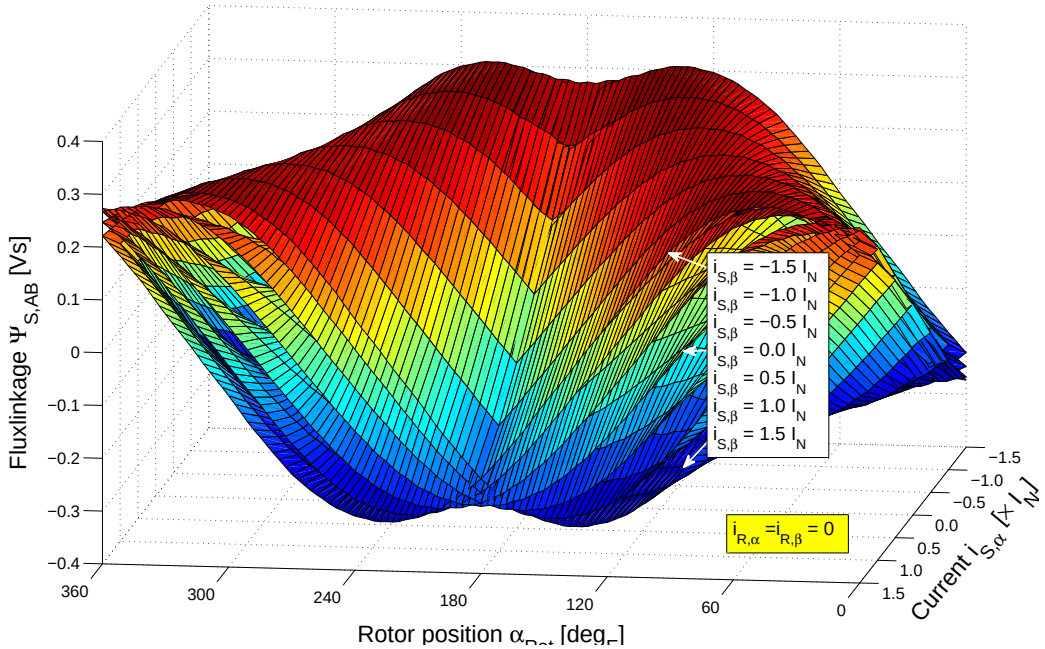

Figure 5.15: Detail of the characteristic curves for the stator phase to phase flux linkage $\Psi_{S,AB}$. Variation of the stator currents ($i_{S,\alpha}$, $i_{S,\beta}$). Both rotor currents ($i_{R,\alpha}$, $i_{R,\beta}$) are zero.

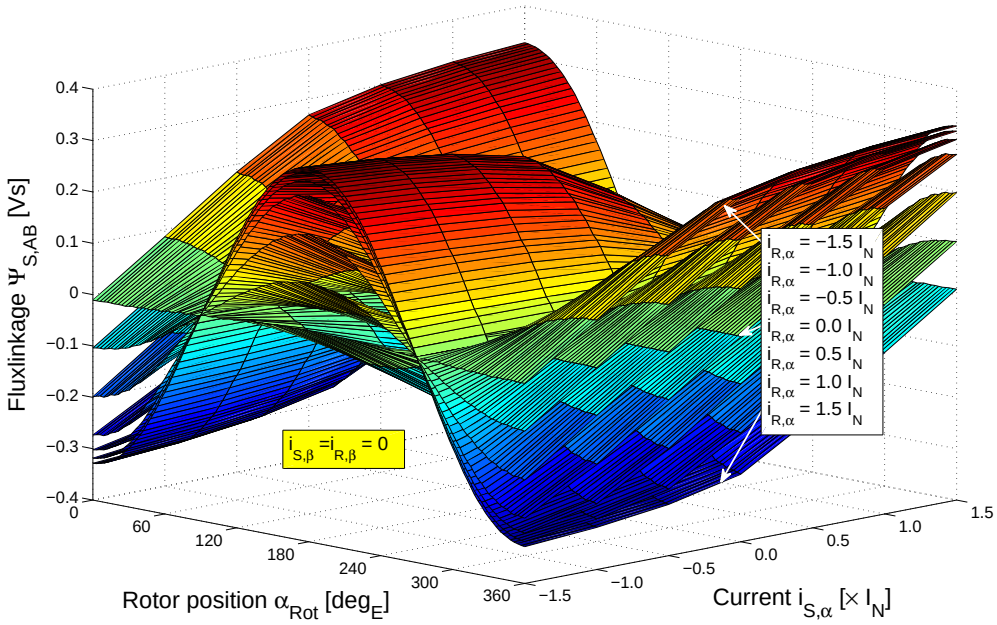

Figure 5.16: Detail of the characteristic curves for the stator phase to phase flux linkage $\Psi_{S,AB}$. Variation of the currents in α-direction ($i_{S,\alpha}$, $i_{R,\alpha}$). Both currents in β-direction ($i_{S,\beta}$, $i_{R,\beta}$) are zero.

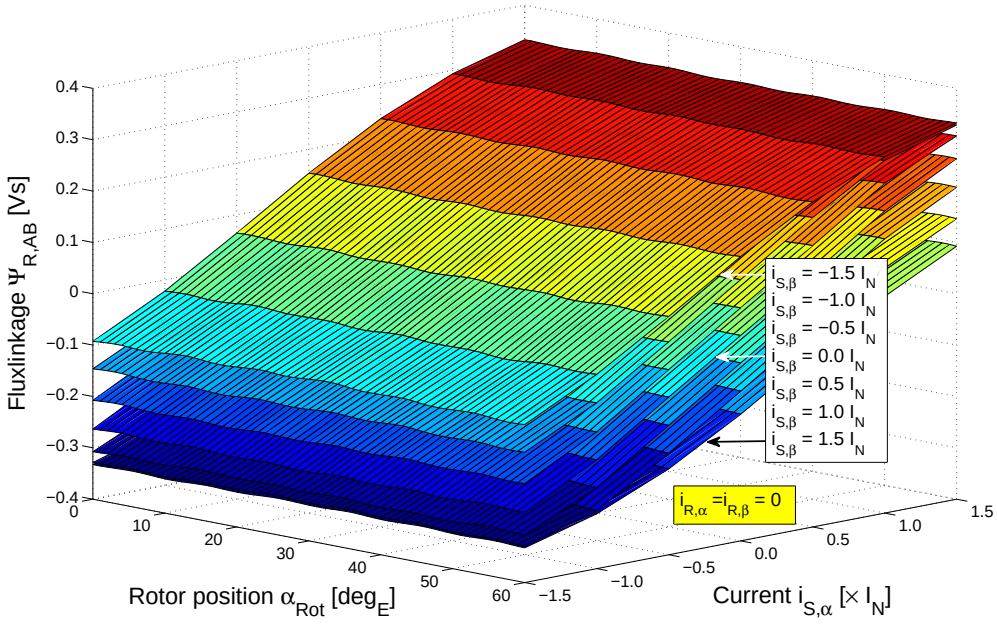

Figure 5.17: Detail of the characteristic curves for the rotor phase to phase flux linkage $\Psi_{R,AB}$. Variation of the stator currents ($i_{S,\alpha}$, $i_{S,\beta}$). Both rotor currents ($i_{R,\alpha}$, $i_{R,\beta}$) are zero.

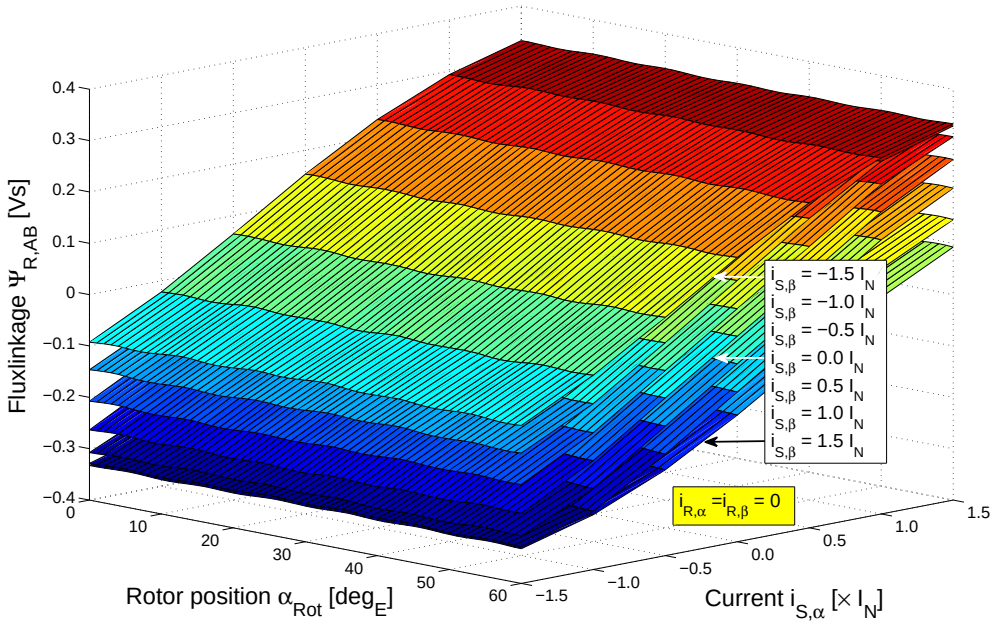

Figure 5.18: Detail of the characteristic curves for the rotor phase to phase flux linkage $\Psi_{R,AB}$. Variation of the currents in α-direction ($i_{S,\alpha}$, $i_{R,\alpha}$). Both currents in β-direction ($i_{S,\beta}$, $i_{R,\beta}$) are zero.

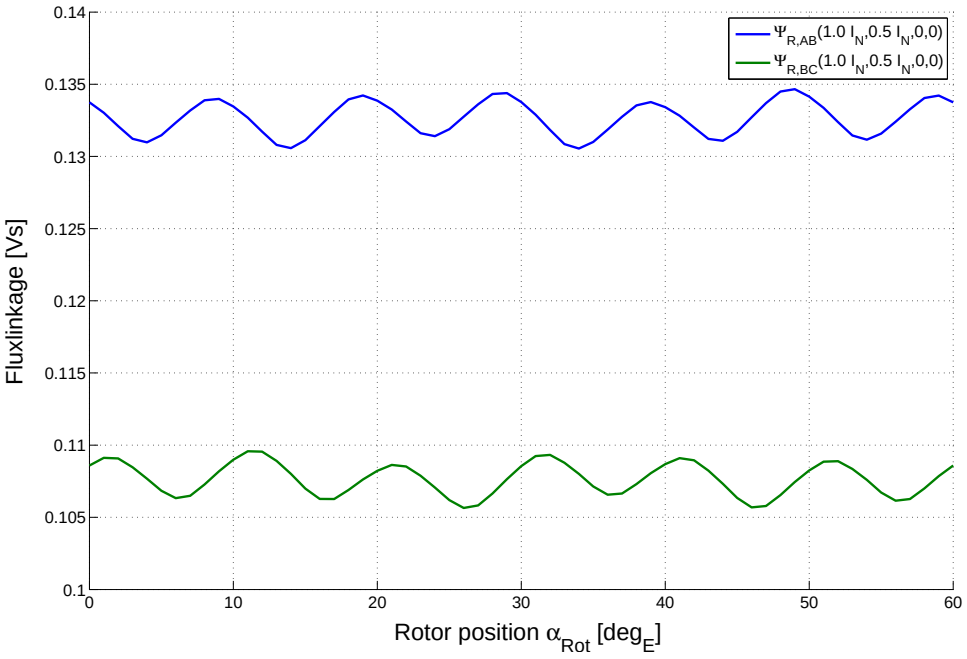

Figure 5.19: Detail of the characteristic curves for the rotor phase to phase flux linkages $\Psi_{R,AB}$ and $\Psi_{R,BC}$ for the stator currents $i_{S,\alpha} = i_N$, $i_{S,\beta} = 0.5 i_N$. Both rotor currents ($i_{R,\alpha}$, $i_{R,\beta}$) are zero.

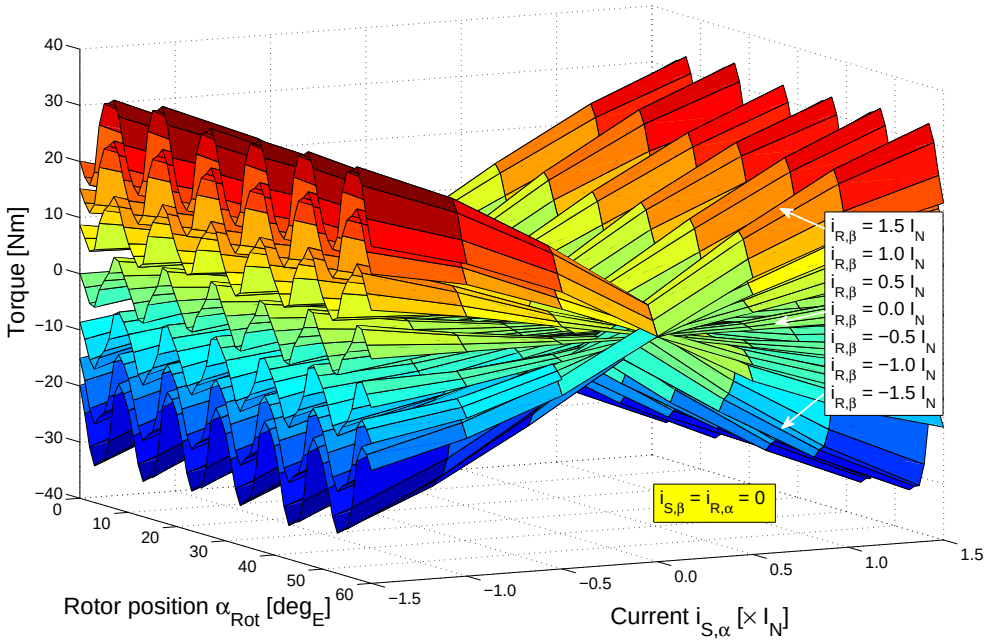

Figure 5.20: Detail of the characteristic curves for the machine torque τ. Variation of the currents $i_{S,\alpha}$ and $i_{R,\beta}$). The other two currents $i_{S,\beta}$ and $i_{R,\alpha}$) are zero.

The last figures in this subsection show some results of the validation simulations. The figures Fig. 5.21 to Fig. 5.23 show a comparison for a simulation at constant speed.

Although Detail-2 in these figures shows a very good agreement, small deviations in Detail-1 (start-up stage) are obvious. Further investigations had shown that these deviations are caused by a too large time step size (100 µs) for the transient FEM simulation. This time step size was originally chosen as tradeoff for the high simulation effort of the FEM simulation.

However, the FEM simulation has been repeated with a smaller time step size (10 µs). This leads to a very good agreement during the start-up stage as shown in Fig. 5.24. However, due to the high simulation effort of the FEM simulation, this second simulation has been only done for a simulation time of 10 ms. Nevertheless, the good agreement of all curves for the second simulation is obvious.

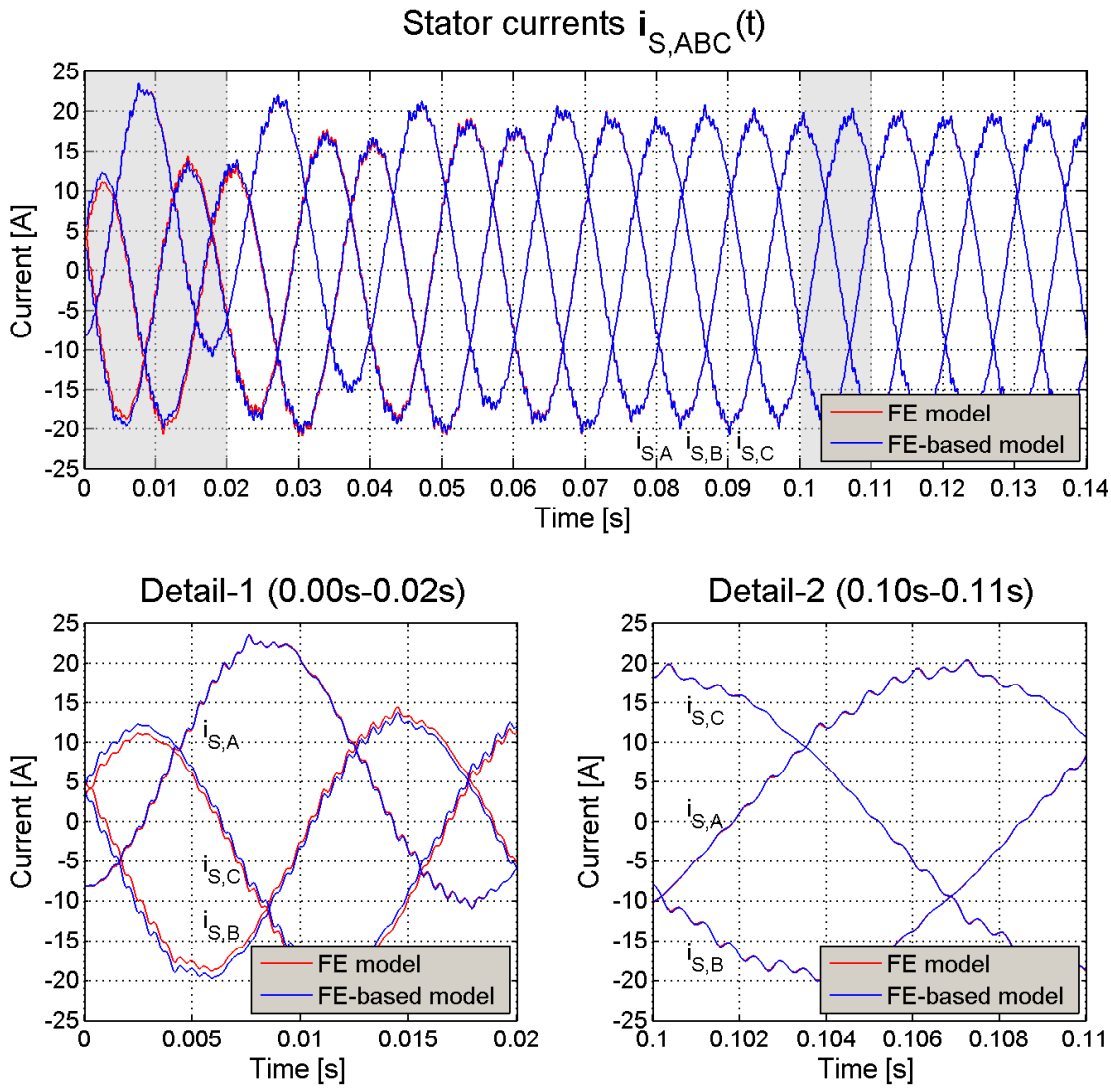

Figure 5.21: Comparison of the stator currents between FE model and FE-based circuit model for a transient simulation. The diagrams show a validation example at constant speed. Except the startup (Detail-1) all curves are in a very good agreement (see Detail-2).

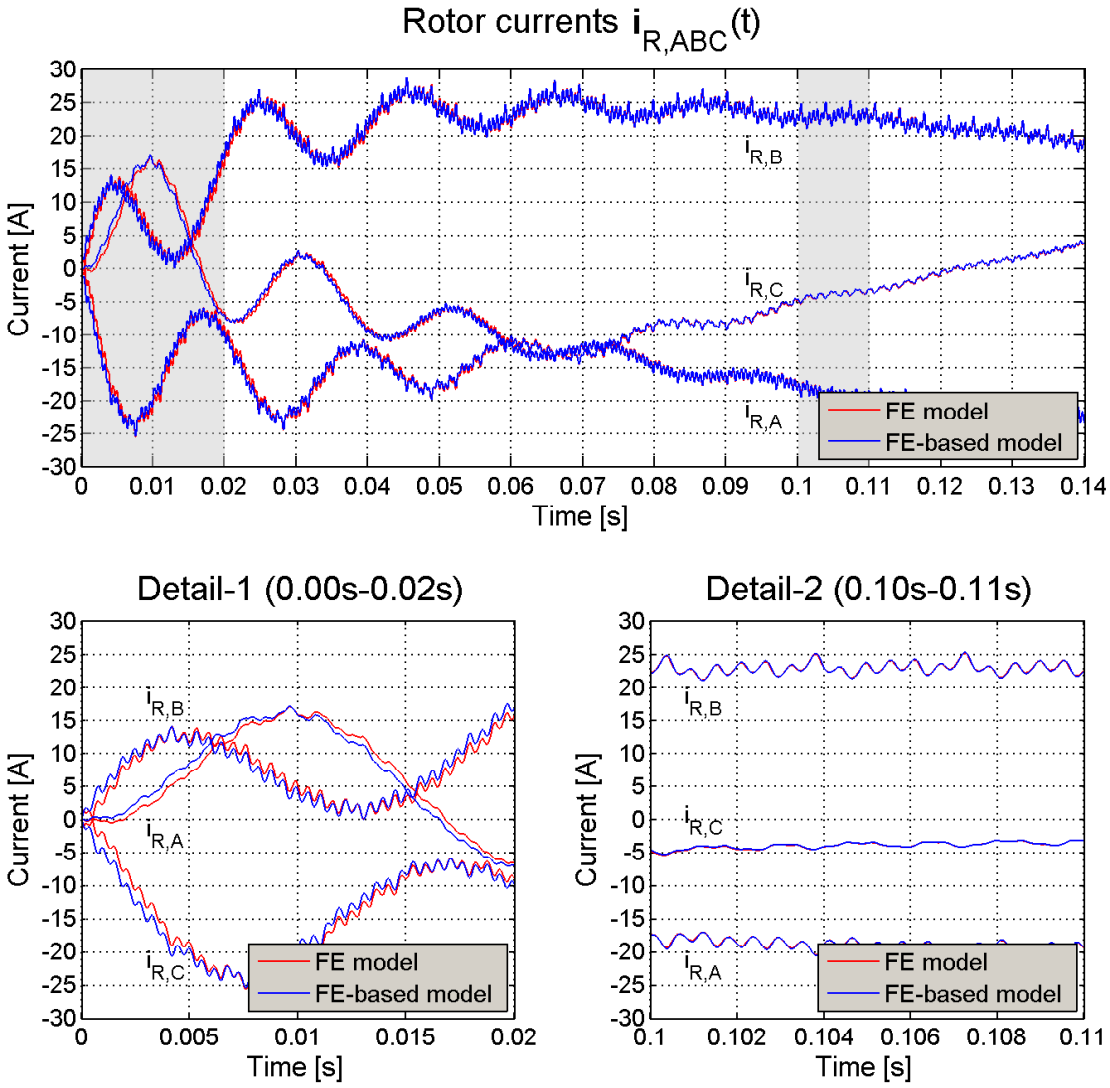

Figure 5.22: Comparison of the rotor currents between FE model and FE-based circuit model for a transient simulation. The diagrams show a validation example at constant speed. Except the startup (Detail-1) all curves are in a very good agreement (see Detail-2).

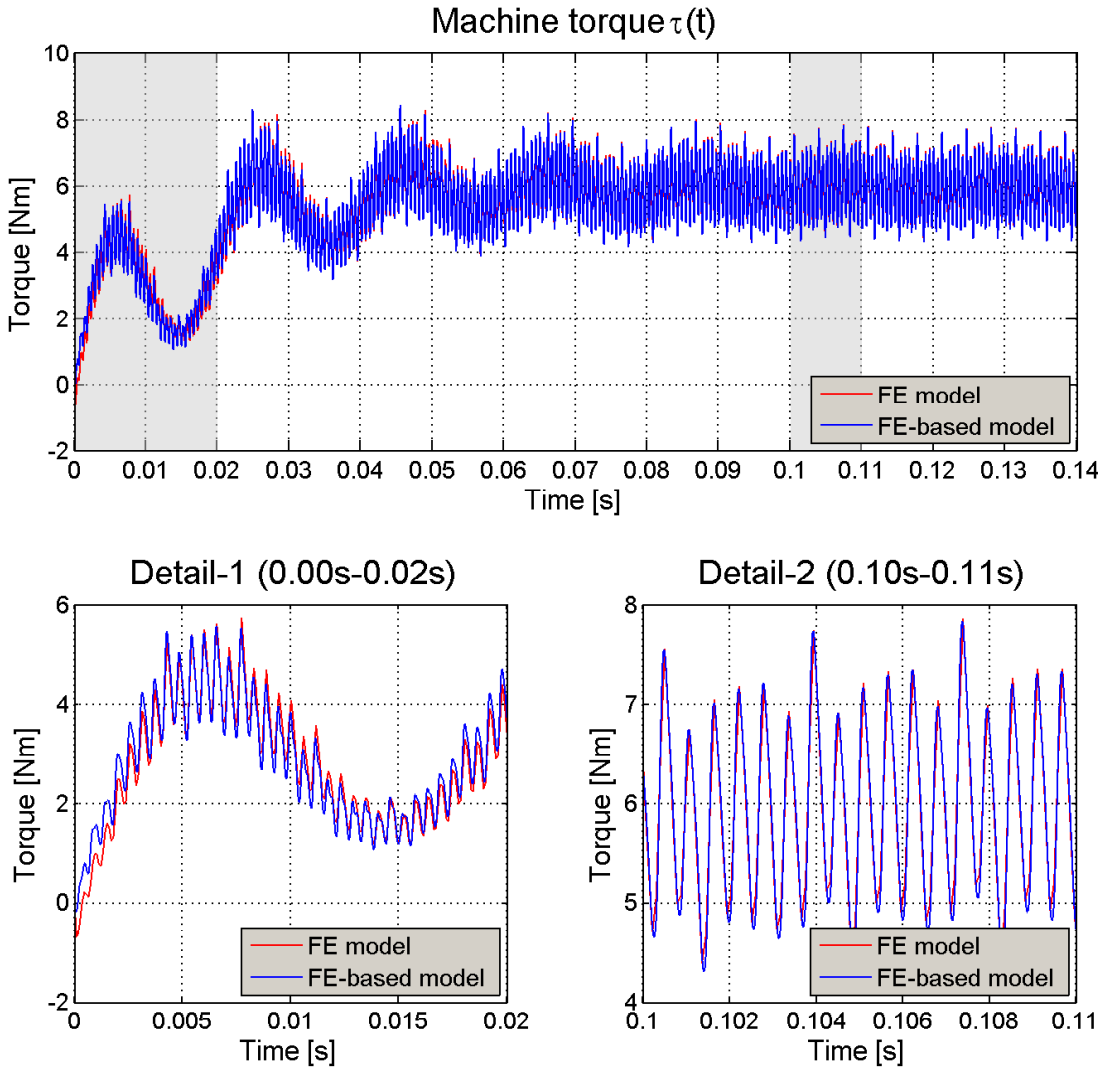

Figure 5.23: Comparison of the machine torque between FE model and FE-based circuit model for a transient simulation. The diagrams show a validation example at constant speed. Except the startup (Detail-1) all curves are in a very good agreement (see Detail-2).

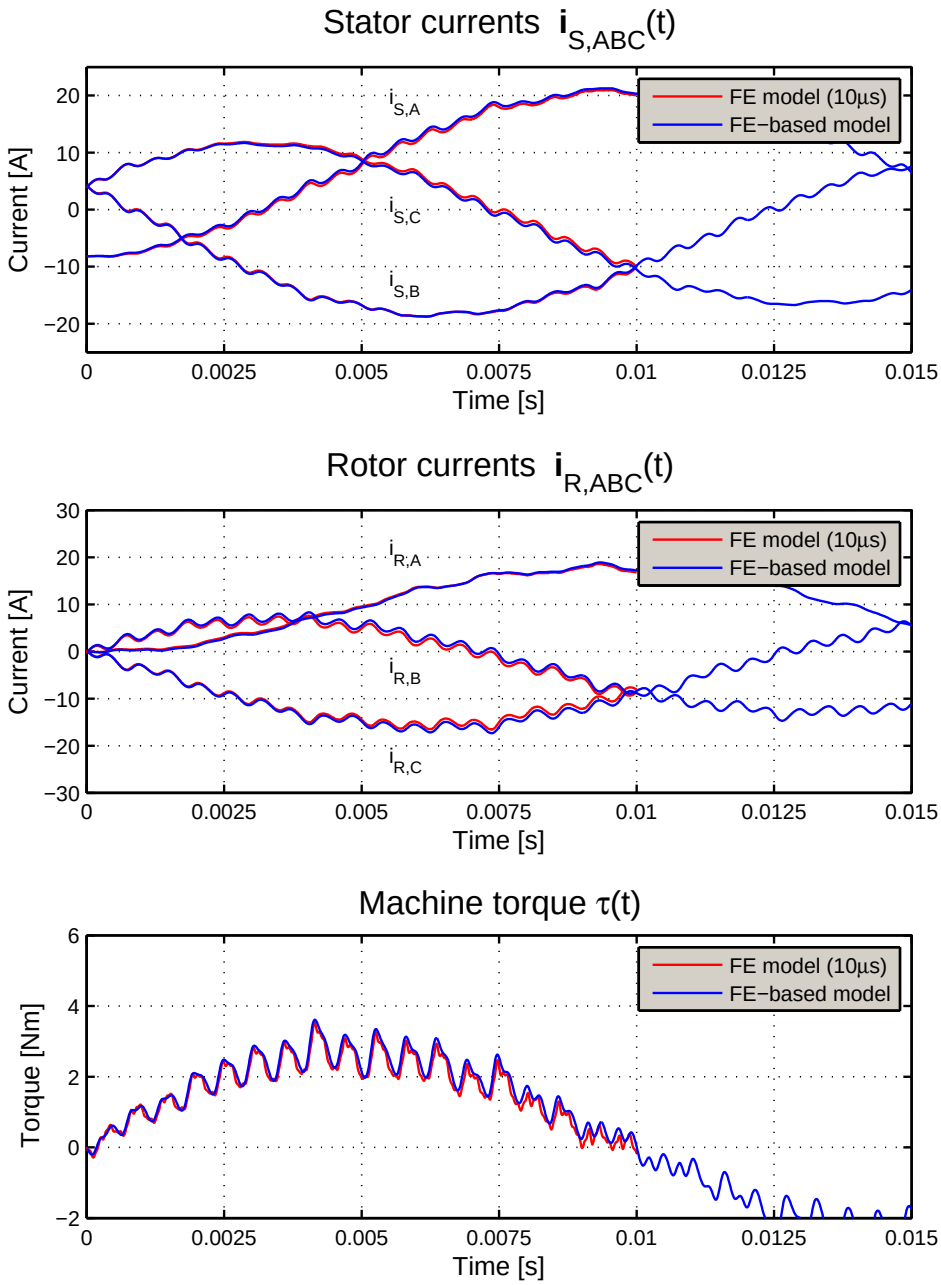

Figure 5.24: Comparison of the stator currents, rotor currents and the machine torque between FE model and FE-based circuit model during the startup. The same time step size has been used for the FEM simulation and the FE-based simulation. Obviously, all diagramms show a very good agreement of the presented curves.

6 EXTENSIONS OF THE FE BASED CIRCUIT MODEL APPROACH

In this chapter two extensions to the FE based circuit model approach are presented. These are:

- An emulation of a 2D-FEM multi-slice simulation for taking skewing into account
- The introduction of additional mechanical state variables for taking rotor eccentricity into account

The results of this chapter have been published in [60], [63] and [65].

6.1 Consideration of skewing

Skewing is a widely used design method for reducing slotting effects in electrical machines. Hereby, the rotor or the stator becomes skewed, as shown for a skewed rotor of a permanent magnet machine in Fig. 6.1. Skewing can be done continuously (Fig. 6.1.a) or in discrete steps (Fig. 6.1.b and Fig. 6.1.c). Continuous skewing is mainly used for induction machines and electrically excited synchronous machines. It is achieved by twisting the lamination stack of the rotor or the stator in axial direction. Staged skewing is mainly used for rotors of permanent magnet machines. This technique allows a simpler shape of the magnets and thus a cheaper production. However, staged skewing can be used for reluctance machines as well.

Modeling of skewing requires the consideration of the machine extending in the axial direction. Basically, this leads to a 3D model of the machine and requires, furthermore, a coupling surface between rotor and stator. However, such 3D-FE models have very high modelling and simulation cost, as already mentioned in section 3.5.

However, this time-consuming method can be avoided. Based on the fact that any variation of the machine geometry in axial direction is small, the 2D FE multi-slice technique (e.g. presented in [77] or [20]) can be used instead. Herewith, a continuously skewed machine is approximated as series of non-skewed "sub-machines", so called slices. This is similar to a staged skewed machine with a high number of rings. Each slice is modeled by a 2D FE model that differs from each other only in the rotor position for considering the different skewing angles of each slice. The same current has to be enforced in the corresponding coils of all slices. Thus all slices must be coupled. This is done by additional constraints, for example realized with circuit elements, as shown in Fig. 6.2.

It can be assumed that, for a sufficiently high number of slices, the effect of skewing to the harmonics of torque and flux as well as its effect to the saturation variation in axial

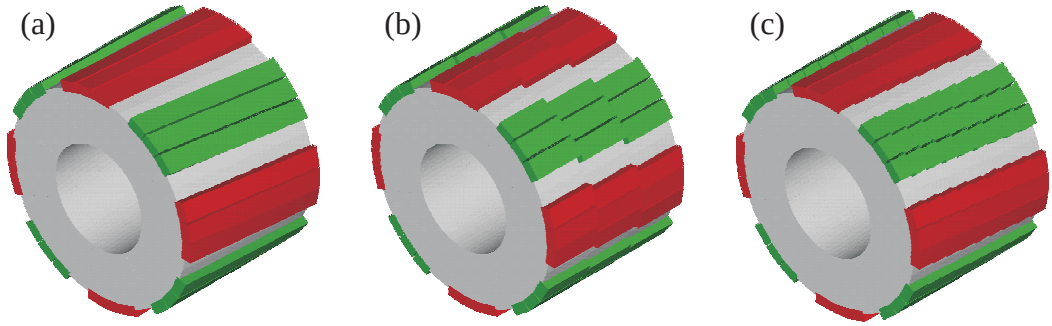

Figure 6.1: Skewing of the rotor of a permanent magnet machine. (a) Continuously skewed rotor with specially shaped magnets (3×3 segments per pole). (b) Staged skewed rotor with 3 rings and with box-shaped magnets (3 segments per ring). (c) Approximation of a continuously skewed rotor using the multi slice technique (e.g. staged skewed rotor with 9 rings (or slices).

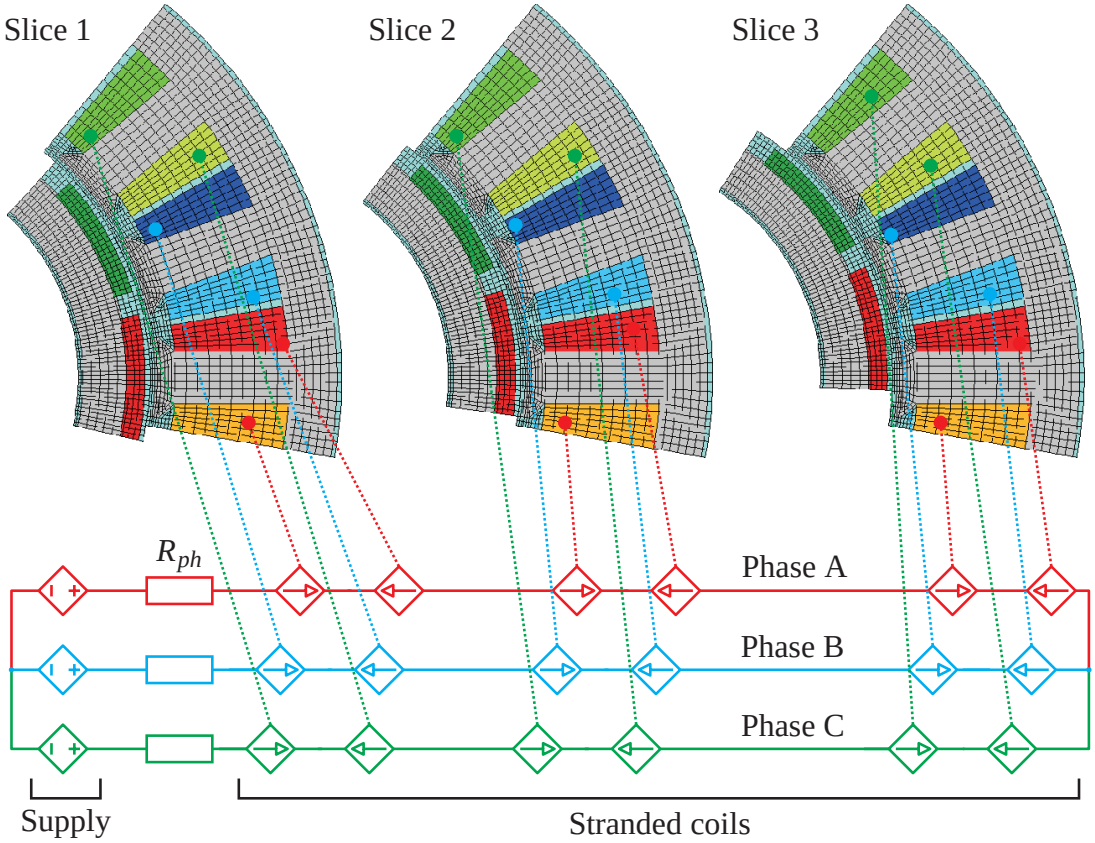

Figure 6.2: 2D FE multi slice model of a skewed permanent magnet machine with 3 slices and an additional coupling circuit in *ANSYS 14.5*.

direction are covered with good approximation. The 2D FE multi-slice technique neglects any radial component of the electric currents as well as any axial component of the magnetic flux. Both typically occur in continuously skewed machines leading to additional stray flux, losses and axial forces. Furthermore, the error of this technique increases for staged sliced machines. This is due to the fact that a non-continuous skewing angle variation in axial direction leads to a three dimensional field distribution that necessitates a 3D FE model. However, the accuracy of the 2D FE multi-slice technique is sufficient in most cases.

The proposed extension to the FE based model circuit approach in this section assumes that the 2D multi-slice technique can be applied to the given machine design. For all other cases where a 3D FEM model is required, all characteristic curves required by the FE-based machine model need also to be determined using 3D FEM simulations.

6.1.1 Multi slice emulation using the FE based circuit model approach

The FE based circuit model approach uses characteristic curves for all model parameters that depend on the rotor position and the current feed state. It can be assumed that all these parameters are sampled in an adequate manner for a proper FE based circuit model. Thus, the whole machine behavior covered by the 2D FE model is also stored in the corresponding look-up tables. This is especially fulfilled for the rotor position dependency of all sampled quantities. Therefore, the 2D FE multi-slice technique can be emulated by a multiple evaluation of the interpolation function at different rotor positions, as shown below.

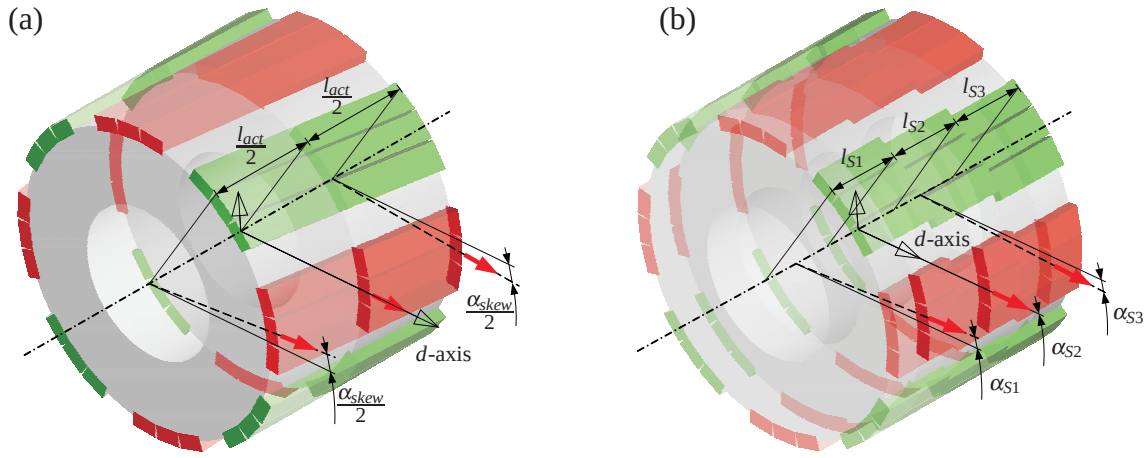

Figure 6.3: Multi slice emulation. (a) Continuously skewed rotor with the active machine length l_{act} and the skewing angle α_{skew}. (b) Multi slice approximation using 3 slices. The skewing angles α_{S1}, α_{S2} and α_{S3} of the slices are defined at the center of each slice. Due to symmetry reasons $\alpha_{S2} = 0$ and all slices have the same slice length $l_{S1} = l_{S2} = l_{S3}$, whereby $l_{S1} + l_{S2} + l_{S3} = l_{act}$.

Let us assume the FE based circuit model of an non-skewed PMSM as represented by (5.1)-(5.3). The look-up table parameters ψ_{AB} and τ are determined for the active length l_{act} of the machine. Furthermore, let us assume a continuously skewed version of this machine with the same active length and a skewing angle α_{skew} (Fig. 6.3.a). This machine should be modelled with N slices, whereas the i^{th}-slice has the length l_{Si}, as shown in Fig. 6.3.b for $N = 3$ slices.

The reference rotor position α_{Rot} is defined by the d-axis of the rotor. Due to symmetry reasons it is located at $\frac{l_{act}}{2}$, i.e. in the middle of the rotor. This leads to the shown skewing angles α_{S1} to α_{SN} for the corresponding slices as shown in the figure. These skewing angles are an additional offset for the rotor position of each slice. This leads for the i^{th}-slice to:

$$\alpha_{Rot}^{Si} = \alpha_{Rot} + \alpha_{Si}. \tag{6.1}$$

To enforce the same phase currents $\mathbf{i}_{ABC}$ in the corresponding phases of each slice, the parameter variables i_d and i_q have to be transformed for each slice too. This can be done by using the Park transformation $\mathbf{P}(.)$ and Clarke transformation $\mathbf{C}$, leading for the i^{th}-slice to

$$\begin{aligned} \begin{pmatrix} i_d^{Si} \\ i_q^{Si} \end{pmatrix} &= \mathbf{P}\left(\alpha_{Rot}^{Si}\right) \cdot \mathbf{C} \cdot \mathbf{i}_{ABC} = \mathbf{P}\left(\alpha_{Rot}^{Si}\right) \cdot \mathbf{C} \cdot \mathbf{C}^{-1} \cdot \mathbf{P}(\alpha_{Rot})^{-1} \cdot \begin{pmatrix} i_d \\ i_q \end{pmatrix} \\ &= \mathbf{P}(\alpha_{Si}) \cdot \begin{pmatrix} i_d \\ i_q \end{pmatrix}, \end{aligned} \tag{6.2}$$

with

$$\mathbf{P}\left(\alpha_{Rot}^{Si}\right) \cdot \mathbf{C} \cdot \mathbf{C}^{-1} \cdot \mathbf{P}(\alpha_{Rot})^{-1} = \mathbf{P}(\alpha_{Rot} + \alpha_{Si}) \cdot \mathbf{P}(\alpha_{Rot})^{-1} = \mathbf{P}(\alpha_{Si}), \tag{6.3}$$

using (3.11). Note that i_d and i_q of the whole machine are defined for the reference rotor position.

Using the slice dependent parameter variables α_{Rot}^{Si}, i_d^{Si}, i_q^{Si} in (6.1) and (6.2) for the evaluation of the interpolation function, the look-up table quantities for each slice can be determined. These values refer to the active length of the machine and thus they need to be scaled to the corresponding slice length l_{Si}. This leads e.g. for the flux linkage ψ_{AB}^{Si} of the i^{th}-slice to:

$$\psi_{AB}^{Si} = \frac{l_{Si}}{l_{act}} \, \psi_{AB}\left(\alpha_{Rot}^{Si}, i_d^{Si}, i_q^{Si}\right). \tag{6.4}$$

Finally, the quantity for the whole machine can be determined as the sum of the corresponding values of all slices. This leads for the total flux linkage ψ_{AB} to:

$$\psi_{AB} = \sum_{i=1}^{N} \frac{l_{Si}}{l_{act}} \, \psi_{AB}\left(\alpha_{Rot}^{Si}, i_d^{Si}, i_q^{Si}\right). \tag{6.5}$$

The second flux linkage ψ_{BC} and the machine torque τ are determined in a similar manner. Due to the linearity of the differential operator, the same approach can be also applied to

evaluate the partial derivatives of the flux linkages, e.g. :

$$\partial_{i_d} \psi_{AB} = \sum_{Si=1}^{N} \frac{l_{Si}}{l_{act}} \, \partial_{i_d} \psi_{AB} \left(\alpha_{Rot}^{Si}, i_d^{Si}, i_q^{Si} \right). \tag{6.6}$$

Note that this approach is an extension for the evaluation of the interpolation function. Therefore, it can be applied to all FE-based machine models presented in this work. The ODE system of the model itself is not affected by this approach. Furthermore, no additional FE simulations are necessary. Finally, and for the sake of completeness it should be mentioned that even dynamic twisting of the rotor could be considered by this approach using time dependent skewing angles. However for typical electric machines this effect is negligible.

6.1.2 Validation of the FE-based multi slice circuit model approach

The validation of the FE-based multi slice circuit model has been done in a similar manner as for the basic variant. Due to the fact that the same characteristic curves can be used, no additional preprocessing has been necessary. The only difference occurs for the transient FE simulation where a multi-slice model has been used, see Fig. 6.2. For the validation, a FE model with 3 slices has been chosen. A direct comparison of the machine currents and machine torque is shown in Fig. 6.4. All curves are in a very good agreement. Thus it can be assumed that the presented model works properly. A comparison of the simulation effort is given in Tab. 6.1. Note that the simulation cost for the FE-based model scales linearly with the number of slices. The evaluation effort per slice is approximately 165 µs.

Table 6.1: Comparison of simulation effort.

Model	Number of slices	Simulation time per time step
Finite element	3	6.53 s
FE-based	1	1.26 ms
FE-based	3	1.61 ms
FE-based	6	2.09 ms

Furthermore, the effect of skewing and the influence of the number of slices have been investigated. The skewing angle has been varied in $10^{\circ\mathrm{E}}$ steps between $0^{\circ\mathrm{E}}$ and $30^{\circ\mathrm{E}}$. A model with 3 slices and a model with 6 slices have been compared. The results for the machine currents are shown in Fig. 6.5, and those for the machine torque in Fig. 6.6. The machine currents increase slightly with increasing skewing angle. Furthermore, current and torque ripple are reduced. Note that for skewing angles of $\pm\ 5^{\circ\mathrm{E}}$ and $\pm\ 10^{\circ\mathrm{E}}$ the number of slices has almost no influence on the result. A variation can be only observed for the machine torque at a skewing angle of $\pm\ 30^{\circ\mathrm{E}}$. In such a case, the difference shown

can be seen as the difference between a staged and continuously skewed machine. In conclusion, all results are feasible and in agreement with the theoretical expectations.

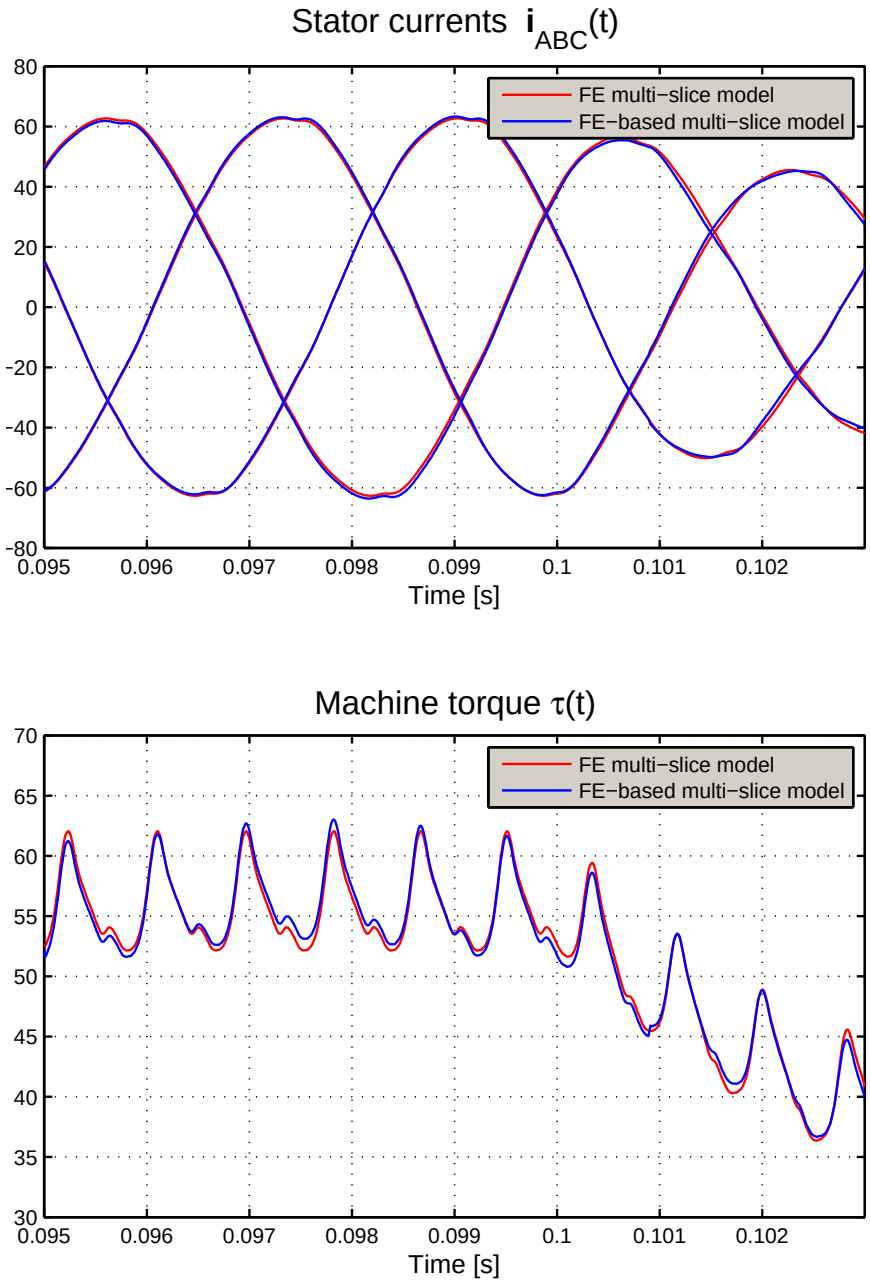

Figure 6.4: Validation of the FE-based multi-slice circuit model approach. A comparison between the multi-slice FEM simulation and the FE-based multi slice circuit model has been carried out. The curves for machine currents and torque show a very good agreement.

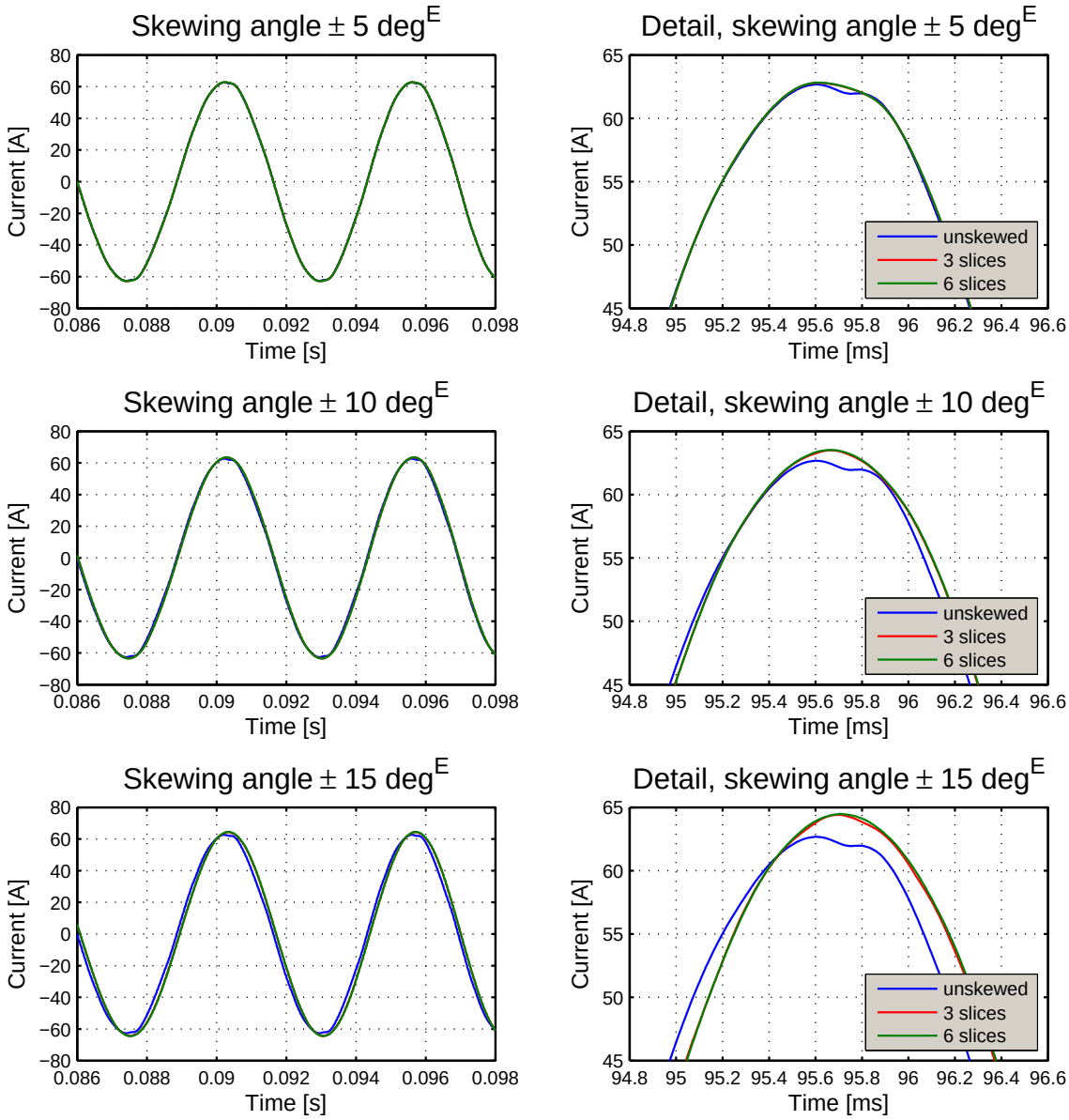

Figure 6.5: Investigation of the influence of the number of slices used. The curves show the machine currents for various skewing angles and for 3 and 6 slices. Furthermore, the machine currents of the non-skewed model are shown.

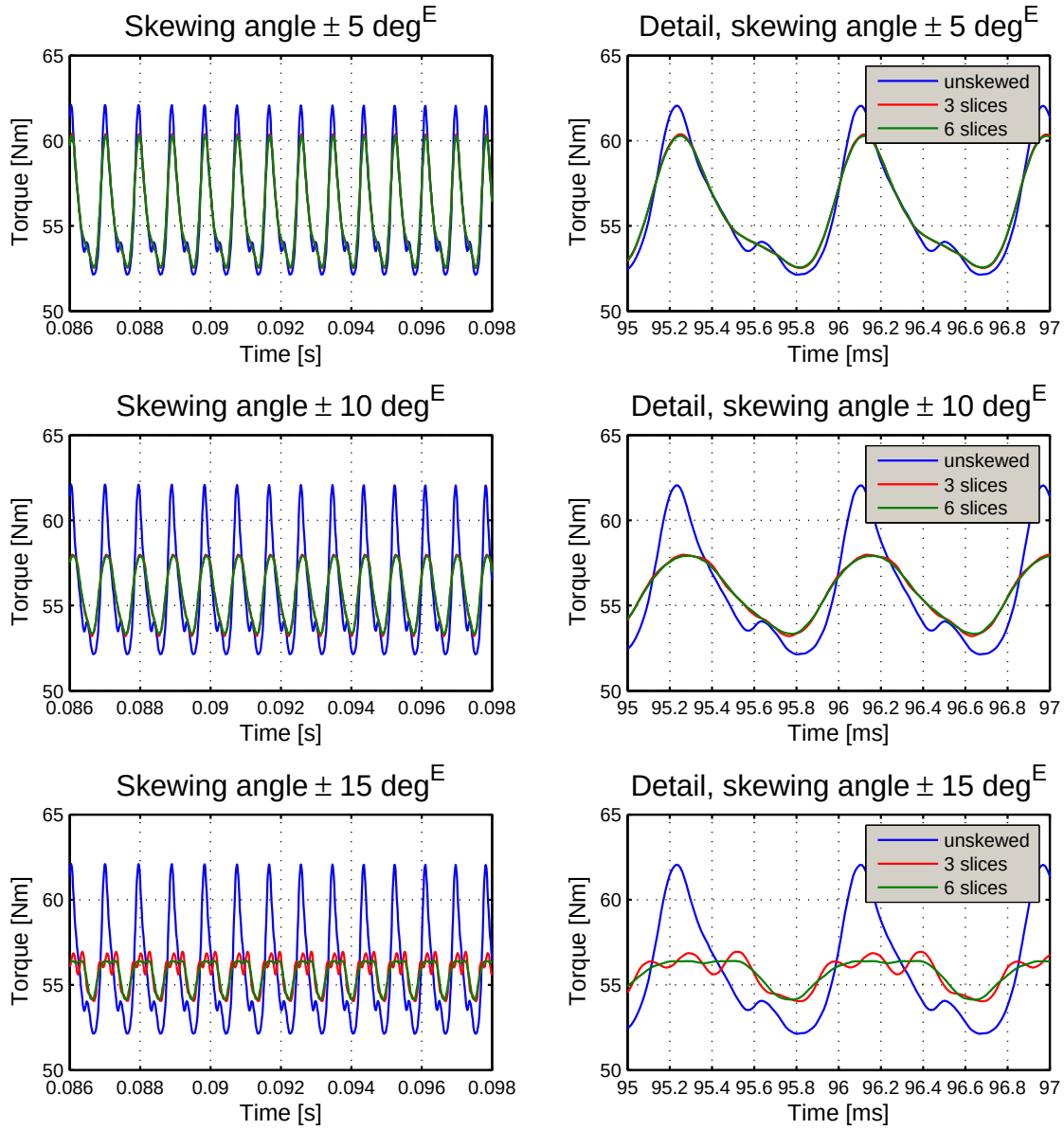

Figure 6.6: Investigation of the influence of the number of slices used. The curves show the machine torque for various skewing angles and for 3 and 6 slices. Furthermore, the machine torque of the non-skewed model is shown.

6.2 Modeling of rotor eccentricity

Any displacement of the rotor from its ideal position in the center of the stator hole is called rotor eccentricity. It occurs in almost all machines and is mainly caused by manufacturing tolerances and bearing clearances. However, dynamic deformations of the rotor could also lead to rotor eccentricity (especially for long machines). Eccentricity annihilates the magnetic symmetry in the machine. This leads, on the one hand, to a lower power factor due to higher iron losses, higher eddy currents (e.g. in permanent magnets) and circular currents in parallel branches of the coil systems. On the other hand, an additional magnetic drag occurs, leading to the generation of higher noise and vibrations.

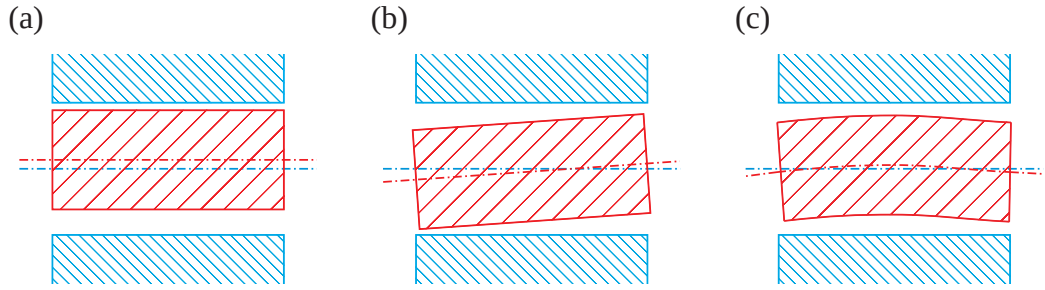

Figure 6.7: Types of eccentricity with stator (blue) and rotor (red). (a) Axis parallel rotor displacement. In this special case no variation of the geometry in axial direction occurs. (b) General displacement with rigid rotor. In this case the rotor can tilt in the air gap within the clearance of the bearings. (c) General displacement with flexible rotor. This is the most general case including bending and twisting of the rotor. From an electro-magnetic point of view any deformation of the rotor can be neglected. Nevertheless, for NVH investigations, a proper modelling of the mechanical excitation is required and thus magnetic forces need to be considered.

In case of axis parallel rotor displacement, as shown in Fig. 6.7.a, no variation in axial direction occurs and a 2D FEM model is sufficient. In all other cases a 3D model of the machine with morphing elements (at least in the air gap) is required in general - a very expensive simulation approach. However, it can usually be assumed that any geometric variation in axial direction is small. Thus, a good approximation can be achieved using the 2D FE multi-slice approach. This simulation technique can be also emulated using the FE-based circuit model approach as described in the last section.

For modelling axis parallel rotor eccentricity, two additional geometric parameters need to be introduced, as shown in Fig. 6.8. Thereby, any rotor displacement within the stator hole can be described. A general rotor displacement can be finally approximated using several slices in axial direction. Each slice is parameterized by rotor position, rotor displacement vector and the machine currents. Thus any rotor displacement in 3D space is approximated by slices with axis parallel rotor displacements. Due to symmetry reasons,

the rotor displacement is described in polar coordinates. This choice simplifies the FEM preprocessing and allows the utilization of symmetry planes. Furthermore, the two additional look-up table parameters $\mathbf{F}_r$ and $\mathbf{F}_\varphi$ for considering the magnetic drag $\mathbf{F}_d$ need to be introduced.

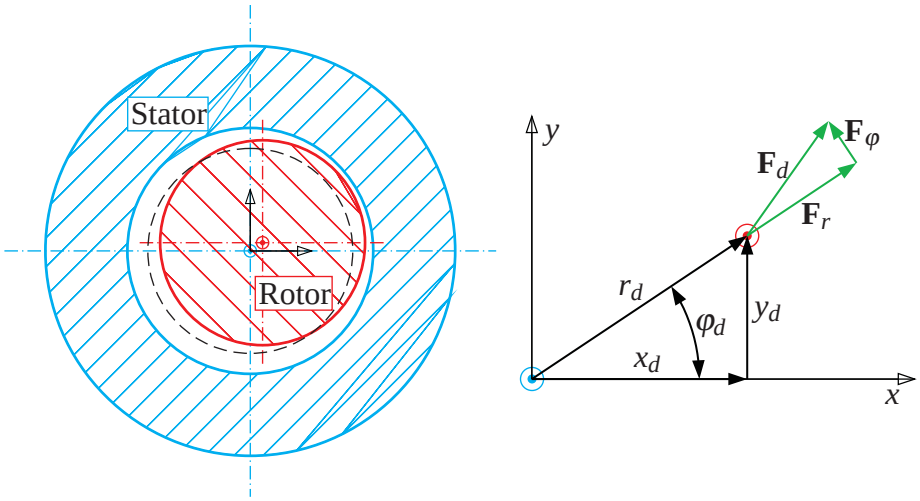

Figure 6.8: Introduction of new geometric parameters for modelling rotor eccentricity. Any rotor displacement in the xy-plane can be described with Cartesian coordinates (x_d, y_d) or with polar coordinates (r_d, φ_d). The magnetic drag $\mathbf{F}_d$ caused by the annihilated magnetic symmetry acts on the rotor and amplifies any displacement. $\mathbf{F}_r$ and $\mathbf{F}_\varphi$ are the components of $\mathbf{F}_d$ in the polar reference frame.

This extension can be basically applied to all FE-based machine models presented in this work. However, the new state variables r_d and φ_d for describing the displacement vector increase the dimension of the sampled state space by two. Although the effect of φ_d can be neglected in many cases, the FE simulation effort for creating the look-up tables as well as its memory demand is significantly higher than for the corresponding basic model. In this work, this extension has been applied to the FE-based circuit model for a PMSM as well as a SYRM.

6.2.1 FE-based multi-slice circuit model for a PMSM

The introduction of two new parameter variables for considering rotor displacement r_d and φ_d leads to the following voltage equation:

$$\begin{pmatrix} v_{AB} \\ v_{BC} \end{pmatrix} = R_{ph} \begin{pmatrix} i_{AB} \\ i_{BC} \end{pmatrix} + \begin{pmatrix} \partial_{\alpha_{Rot}} \psi_{AB} \\ \partial_{\alpha_{Rot}} \psi_{BC} \end{pmatrix} \frac{d\alpha_{Rot}}{dt} + \begin{bmatrix} \partial_{r_d} \psi_{AB} & \partial_{\varphi_d} \psi_{AB} \\ \partial_{r_d} \psi_{BC} & \partial_{\varphi_d} \psi_{BC} \end{bmatrix} \begin{pmatrix} \frac{dr_d}{dt} \\ \frac{d\varphi_d}{dt} \end{pmatrix} + \begin{bmatrix} \partial_{i_d} \psi_{AB} & \partial_{i_q} \psi_{AB} \\ \partial_{i_d} \psi_{BC} & \partial_{i_q} \psi_{BC} \end{bmatrix} \begin{pmatrix} \frac{di_d}{dt} \\ \frac{di_q}{dt} \end{pmatrix}. \quad (6.7)$$

Applying the multi-slice technique leads finally to

$$\sum_{i=1}^{N} \frac{l_{Si}}{l_{act}} \begin{bmatrix} \partial_{i_d} \psi_{AB}^{Si} & \partial_{i_q} \psi_{AB}^{Si} \\ \partial_{i_d} \psi_{BC}^{Si} & \partial_{i_q} \psi_{BC}^{Si} \end{bmatrix} \begin{pmatrix} \frac{di_d}{dt} \\ \frac{di_q}{dt} \end{pmatrix} = \begin{pmatrix} v_{AB} \\ v_{BC} \end{pmatrix} - R_{ph} \begin{pmatrix} i_{AB} \\ i_{BC} \end{pmatrix} - \sum_{i=1}^{N} \frac{l_{Si}}{l_{act}} \left[\begin{pmatrix} \partial_{\alpha_{Rot}} \psi_{AB}^{Si} \\ \partial_{\alpha_{Rot}} \psi_{BC}^{Si} \end{pmatrix} \frac{d\alpha_{Rot}^{Si}}{dt} + \begin{bmatrix} \partial_{r_d} \psi_{AB}^{Si} & \partial_{\varphi_d} \psi_{AB}^{Si} \\ \partial_{r_d} \psi_{BC}^{Si} & \partial_{\varphi_d} \psi_{BC}^{Si} \end{bmatrix} \begin{pmatrix} \frac{dr_d^{Si}}{dt} \\ \frac{d\varphi_d^{Si}}{dt} \end{pmatrix} \right]. \quad (6.8)$$

with the active length l_{act} used for the parameter determination as well as the slice length l_{Si}, the rotor position α_{Rot}^{Si} and the rotor displacement (r_d^{Si}, φ_d^{Si}) of the i^{th} slice *Si*. Notice that α_{Rot}^{Si}, r_d^{Si} and φ_d^{Si} are treated as mechanical inputs (e.g. from a multi body dynamics simulation) and thus are written on the right side of (6.8).

The machine torque τ and the components of the magnetic drag F_r, F_φ are determined using

$$\tau = \sum_{i=1}^{N} \frac{l_{Si}}{l_{act}} \tau \left(\alpha_{Rot}^{Si}, r_d^{Si}, \varphi_d^{Si}, i_d^{Si}, i_q^{Si} \right), \quad (6.9)$$

$$F_r = \sum_{i=1}^{N} \frac{l_{Si}}{l_{act}} F_r \left(\alpha_{Rot}^{Si}, r_d^{Si}, \varphi_d^{Si}, i_d^{Si}, i_q^{Si} \right), \quad (6.10)$$

$$F_\varphi = \sum_{i=1}^{N} \frac{l_{Si}}{l_{act}} F_\varphi \left(\alpha_{Rot}^{Si}, r_d^{Si}, \varphi_d^{Si}, i_d^{Si}, i_q^{Si} \right). \quad (6.11)$$

6.2.2 Preprocessing and data set

For the validation of the presented model approach, a PMSM with six magnetic pole pairs and surface mounted magnets have been used. All six coils per phase are connected in series. The three phase system is in Y-connection with isolated star point. The 2D FE model of the machine is shown in Fig. 6.9. Due to the fact that any magnetic symmetry is annihilated, a full model of the machine is necessary. For considering the deformation of the airgap (Fig. 6.9.b and Fig. 6.9.c) a re-mesh is required for each rotor displacement.

Nevertheless, since we have five independent parameters, a high number of magneto-static simulations is necessary. Due to the lack of magnetic symmetry, the rotor position needs to be varied in an interval of $0^{\circ E}$ to $180^{\circ E}$. Furthermore, the radial and azimuthal

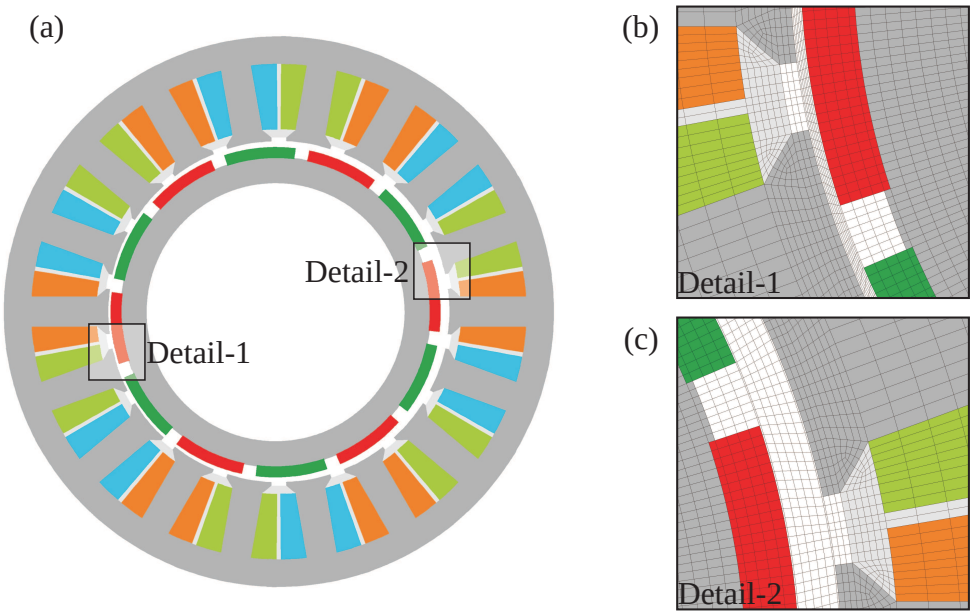

Figure 6.9: FEM model for parameter determination. (a) A full model of the machine is required because any magnetic symmetry is annihilated by the rotor displacement. The air gap is re-meshed for every rotor position and displacement. (b) Detail of the mesh for a compressed air gap. (c) Detail of the mesh for a stretched air gap.

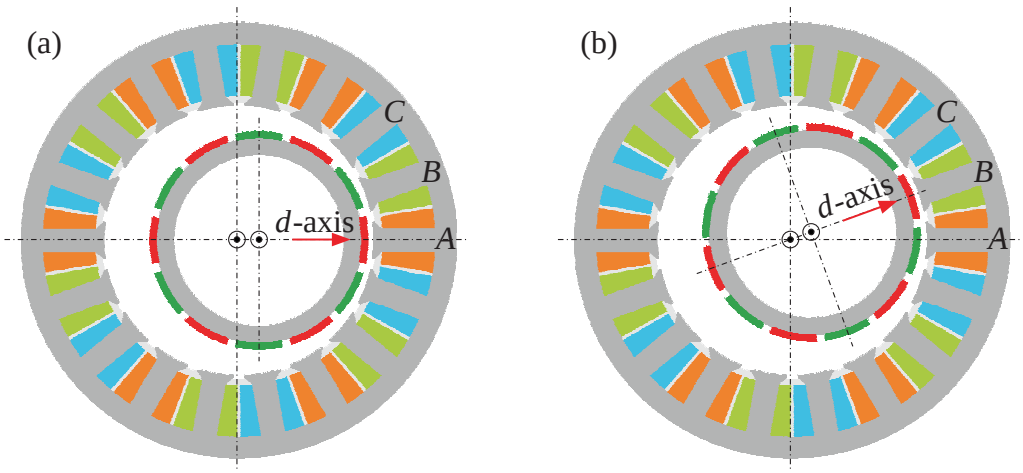

Figure 6.10: Symmetry of rotor displacement. The size of the air gap is shown augmented for increased clarity of the illustration. (a) Rotor displacement in direction of phase A. (b) Rotor displacement in direction of phase B. This state is identical to (a) and can be determined from the corresponding simulation data.

rotor displacements need to be sampled. Due to symmetry reasons, an interval of $0^{\circ\mathrm{E}}$ to $120^{\circ\mathrm{E}}$ is sufficient for φ_d^{Si}, as shown in Fig. 6.10. Thus a complete dataset can be built by concatenating the data for this interval.

In the remainder of this subsection, some conclusions about the influence of eccentricity for the machine model used will be drawn. The flux linkages for all three phases are shown in Fig. 6.11 for seven different current feed states and for all 16 rotor displacements (concentric case and three radial variations with five azimuthal variations). Obviously, only seven different curves (for the seven current feed states) per phase are observable. The influence of any rotor displacement to the flux linkage is negligible. This is due to the interconnection of the coils (series connection of all coils of a phase). Thus, the effect of eccentricity is mostly compensated for the flux linkages.

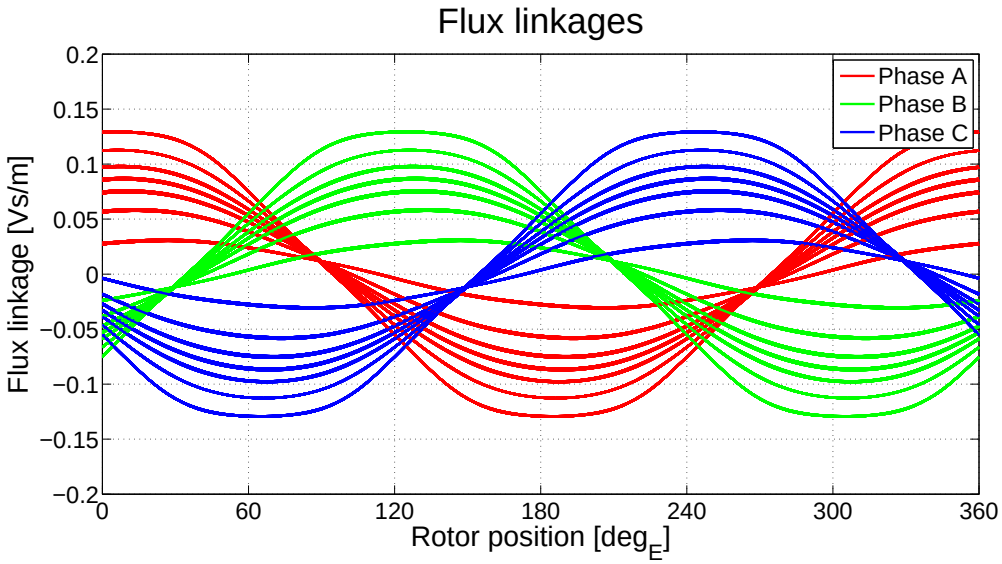

Figure 6.11: Flux linkages of all three phases. Although a set of curves covering all rotor displacements and seven different current feed states are shown, only seven curves per phase are observable. These seven curves correspond to the different current feed states and any effect of rotor displacement is negligible. This behavior is caused by the series connection of all teeth coils per phase. Thus any magnetic unbalance of the machine is compensated for the phase flux linkages.

A comparison of the flux linkages per coil for phase *A* and a radial rotor displacement of 1.2 mm is shown in Fig. 6.12. The influence of the rotor displacement is obvious. In case of an interconnection with parallel branches, these differences lead to different induced voltages and thus circulating currents. Higher losses and a stronger heating of the machine are the consequence.

The machine torque is almost unaffected by rotor displacements. Only the influence of a radial displacement can be observed in Fig. 6.13. The influence of an azimuthal rotor

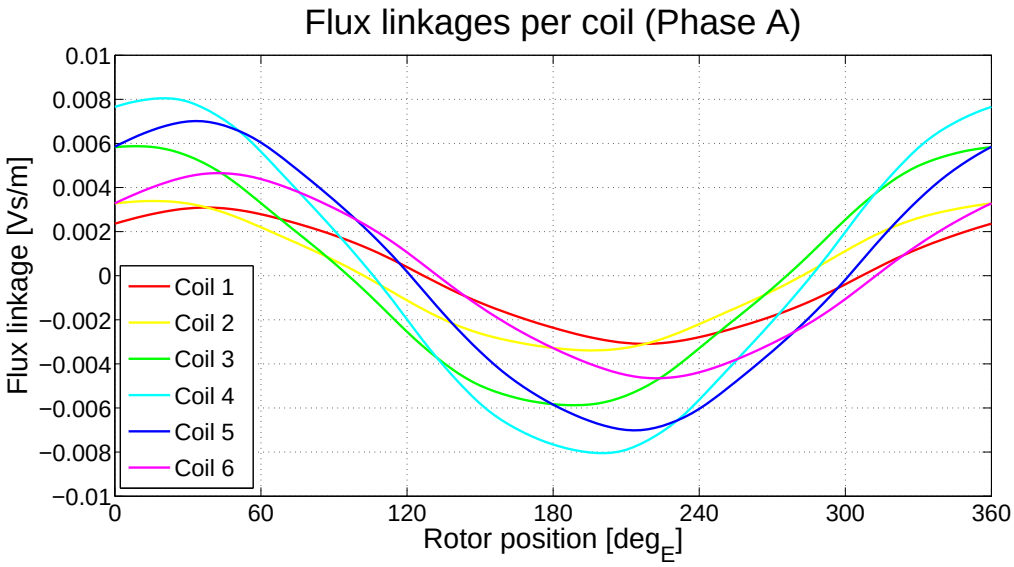

Figure 6.12: Flux linkages per coil for phase *A*. Any rotor displacement leads to different flux linkages in the coils of phase *A*.

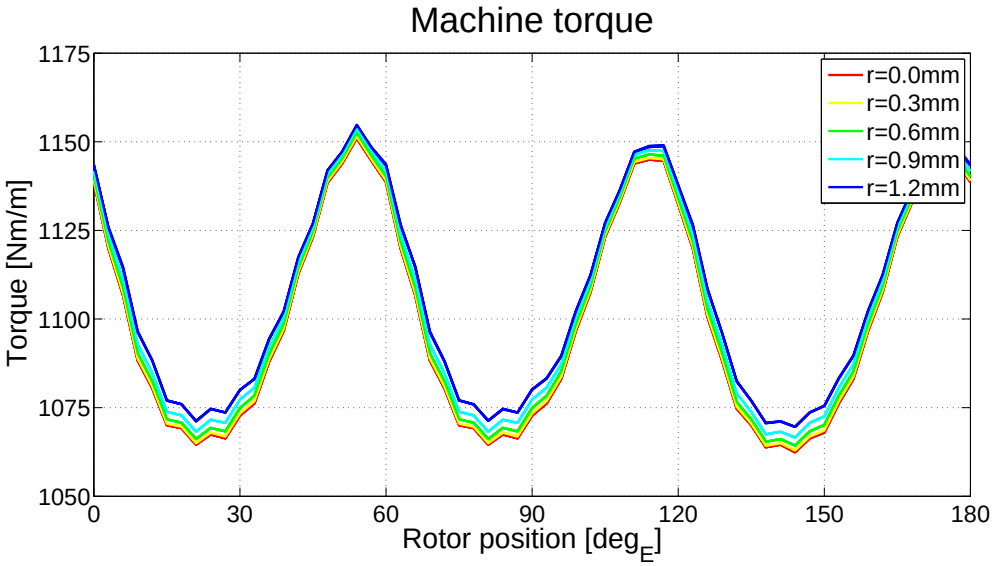

Figure 6.13: Machine torque. Although the set of curves shown consist of all displacements of the rotor, only the effect of the radial displacement is observable, any azimuthal displacement is negligible.

displacement is in a sub-percentage range for the whole dataset.

The magnetic drag for a single current feed state is shown in Fig. 6.14 for the radial component F_r and in Fig. 6.15 for the azimuthal component F_φ. Obviously, F_φ is very

small and can be neglected for the machine under investigation. This simplification would lead to a smaller memory demand for the FE-based circuit model.

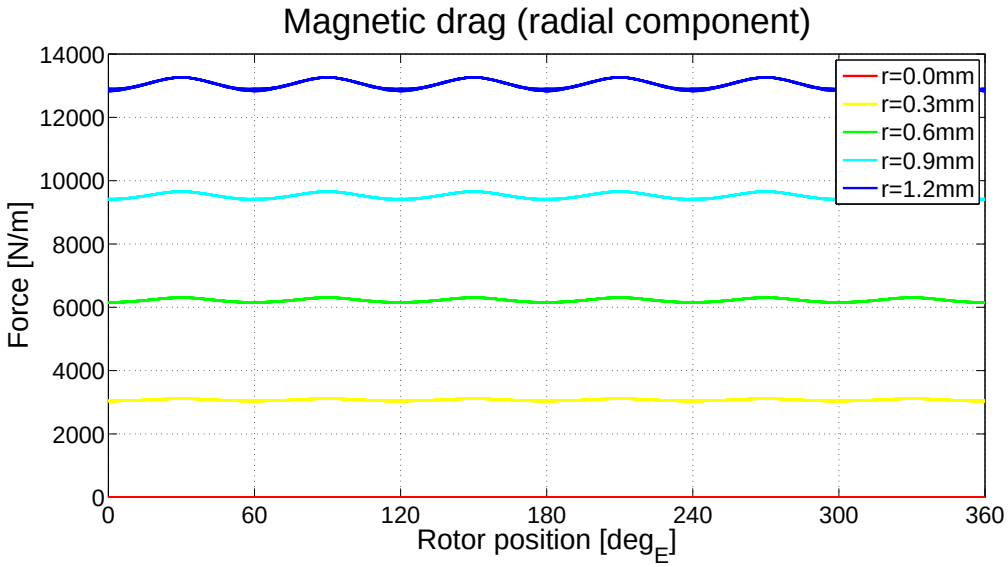

Figure 6.14: Magnetic drag in radial direction. Although the set of curves shown consist of all displacements of the rotor, only the effect of the radial displacement is observable, any azimuthal displacement is negligible. Furthermore, harmonics caused by slotting are apparent.

Finally, it should be also mentioned that even the state variable for the azimuthal rotor displacement can be neglected for the machine investigated. Thus the state space is only four-dimensional leading to a reduced preprocessing effort and memory demand for the FE-based circuit model. It is expected that this simplification can be done for almost all electrical machines with a common design. However, any further investigations of the above simplifications are not in the scope of this work and the full model was used for the validation.

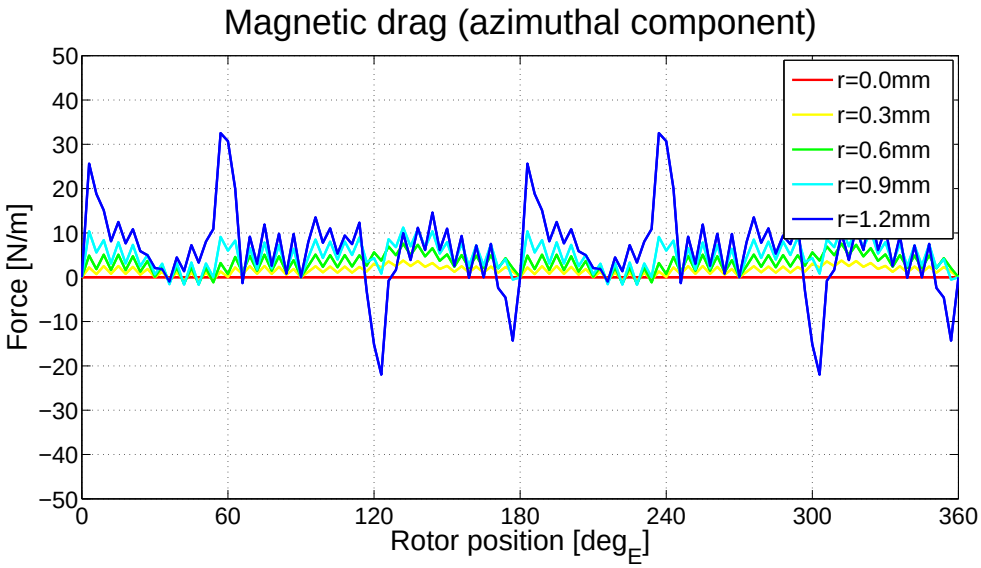

Figure 6.15: Magnetic drag in azimuthal direction. Although the set of curves shown consist of all displacements of the rotor, only the effect of the radial displacement is observable, any azimuthal displacement is negligible. Compared with the radial component of the magnetic drag, the azimuthal component is several orders of magnitude smaller. Furthermore, numerical errors caused by the mesh can be observed. For the machine under investigation, the azimuthal component of the magnetic drag can be neglected.

6.2.3 Validation of the FE-based model approach

The validation was done in a similar manner as described in section 4.5. However, the FEM model is in this case more complex because a full machine model is required, see Fig. 6.16.

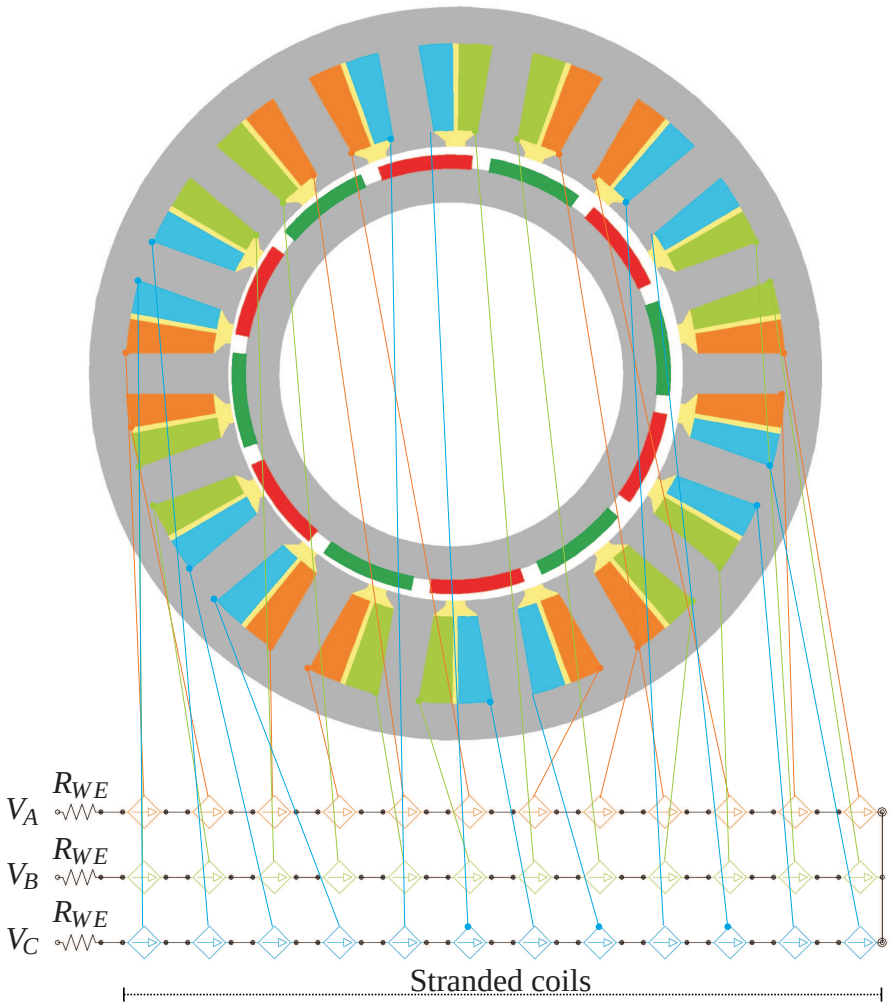

Figure 6.16: FE model for transient simulation with voltage fed coils. The figure shows the connection between all machine coils and the corresponding circuit elements for stranded coils. The additional resistance of the end windings is modelled by the resistor elements R_{WE}.

A re-mesh of the air gap during a transient simulation is not supported by the FEM tool. For this reason, another approach for modelling the air gap was required, as shown in Fig. 6.17. All air gap elements are divided into rotor and stator related elements. The concentric case defines the initial position of the rotor (Fig. 6.17.a). In this case the air gap elements

related to rotor and stator build two rings whereby all nodes related to these elements lie on concentric circles. Modelling of a random rotor position is done in four steps:

1. The rotor including the rotor related air gap elements is rotated into its required angular position (Fig. 6.17.b).

2. The rotor including the rotor related air gap elements is shifted to its required position (Fig. 6.17.c).

3. The deformation of the air gap elements is done by moving the corresponding element nodes (Fig. 6.17.d).

4. Coupling of rotor and stator using constraint equations (Fig. 6.17.e).

By this approach, strongly distorted elements in the air gap can be avoided and the coupling interface can be located in the center of the air gap. Thus numerical errors can be minimzed.

Additionally to the magnetostatic FE model, an MBD-model with rotor mass unbalance and a bearing model including stiffness and clearance were investigated. The MBD-model is shown in Fig. 6.18. The mass unbalance leads to a radial force acting on the rotor in rotational motion. Due to stiffness and clearance of the bearings, a rotor displacement occurs. The rotor displacement (Fig. 6.19) is used as additional mechanical input for the electric simulation of the machine (FE-based circuit model or FE model).

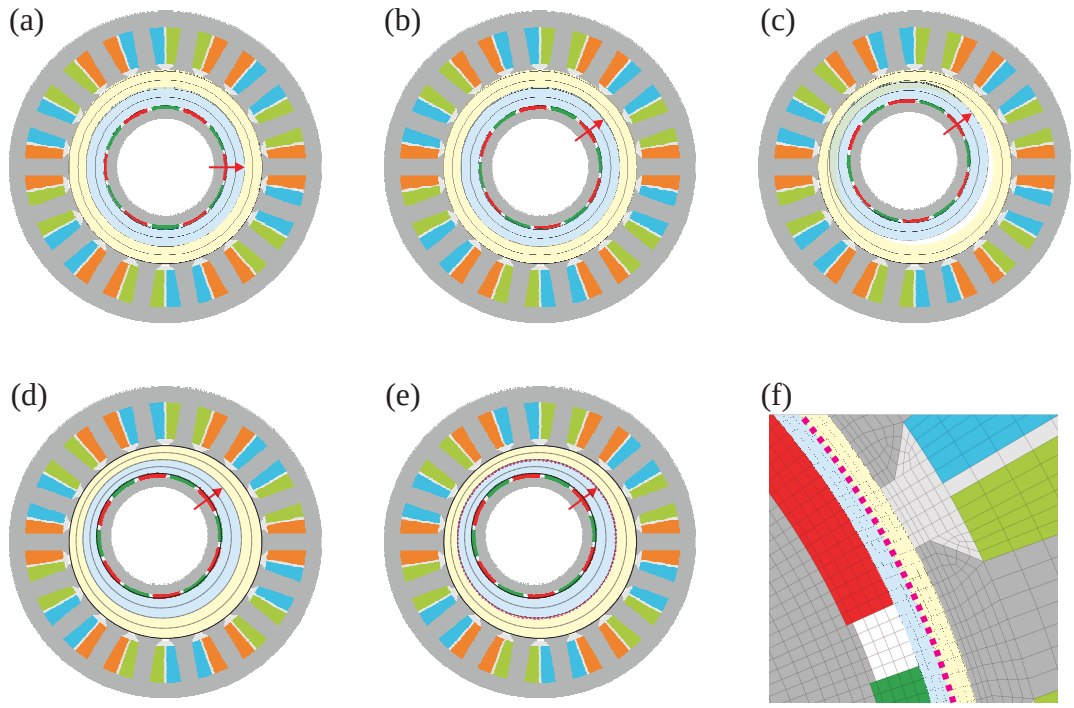

Figure 6.17: Modelling of the air gap for transient FEM simulations. The rotor related air gap elements (light blue) and the stator related air gap elements (light yellow) are coupled using constraint equations (magenta). The nodes of the air gap elements are illustrated by the dotted circles in the air gap. The air gap is shown enlarged for better clarity. (a) Concentric rotor position (initial position). (b) Rotation of the rotor including rotor related air gap elements to the required rotor position. (c) Shift of the rotor including rotor related air gap elements to the required rotor displacement. Overlapping air gap elements occur. (d) Deformation of the air gap elements by moving the element nodes, illustrated by the eccentric circles. (e) Coupling of rotor and stator related air gap elements in the center of the air gap. (f) Detail of the FEM model showing the final air gap.

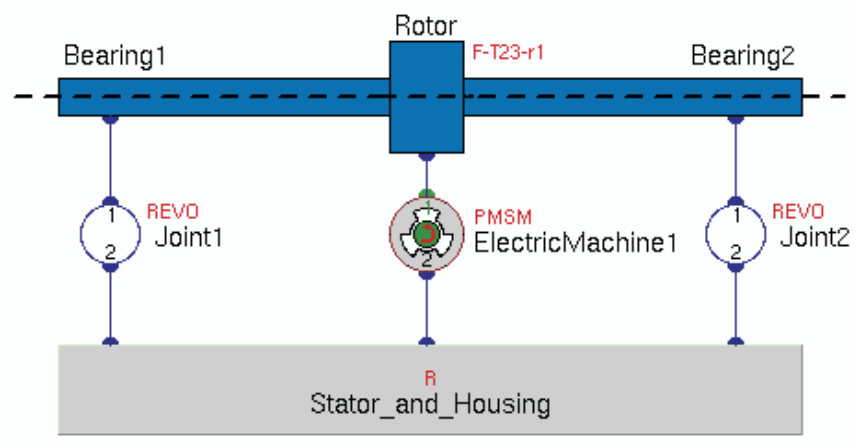

Figure 6.18: MBD Multi-body-dynamics model. Rotor and stator are modelled as rigid bodies whereby the rotor has a mass unbalance. Simple models of bearings including stiffness and clearance are modelled by the REVO-joints. The electrical machine is modelled with the EMC-joint in the center.

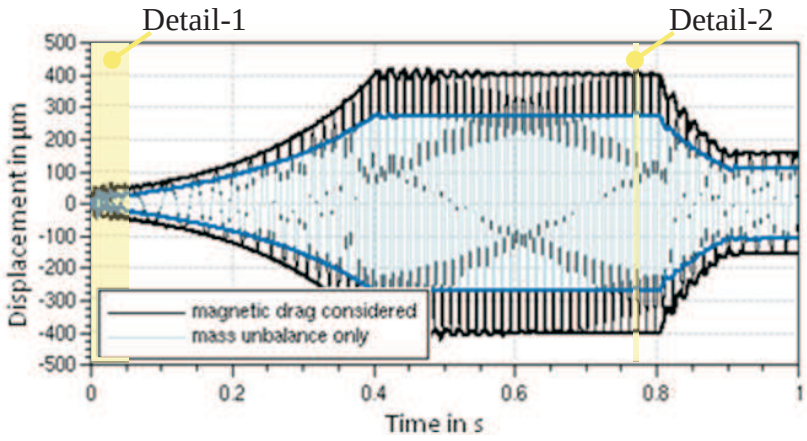

Figure 6.19: Rotor displacement in *x*-direction without consideration of magnetic drag (blue) and with magnetic drag (black). Time windows for detail plots are shown in yellow.

Fig. 6.20 to Fig. 6.22 show several comparisons between the FEM reference solution and the presented FE-based circuit model. All figures show a comparison for time window Detail-1 and Detail-2 as specified in Fig. 6.19. Detail-1 shows the comparison for the start-up stage where only small rotor displacement occurs. Detail-2 shows a steady state case with high rotor displacement. Obviously, all curves are in good agreement and the proper functioning of the presented model approach has been proved.

Note that even slotting effects for the magnetic drag are covered (see Fig. 6.22). In combination with the formerly presented multi-slice emulation, this model approach is well suited for noise and vibration harshness (NVH) investigations.

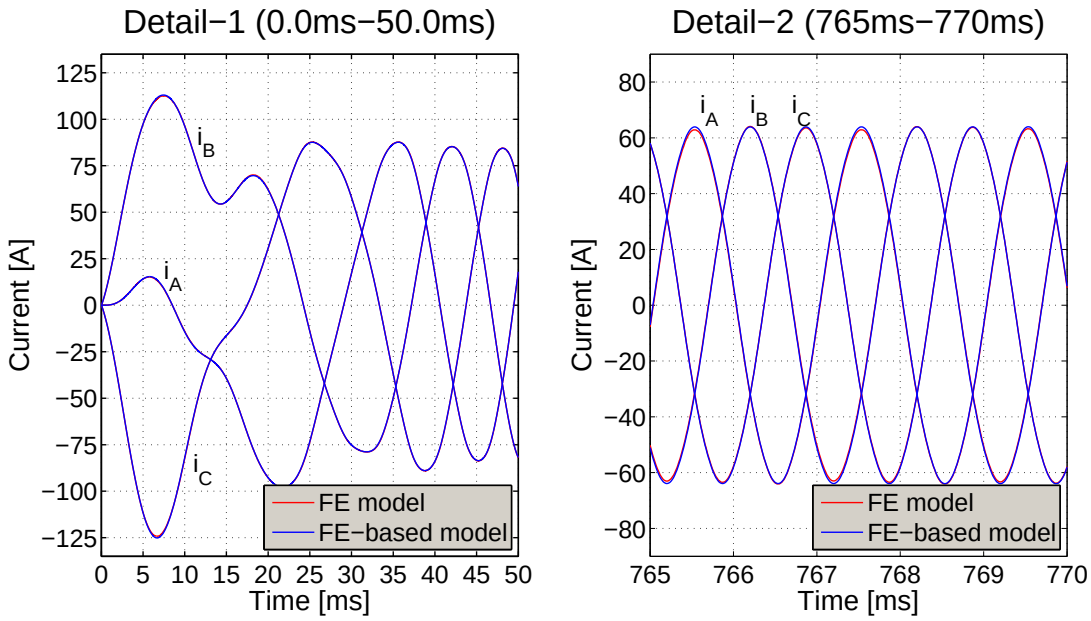

Figure 6.20: Comparison of phase currents i_A, i_B and i_C between FE model (reference solution) and the presented FE-based machine model.

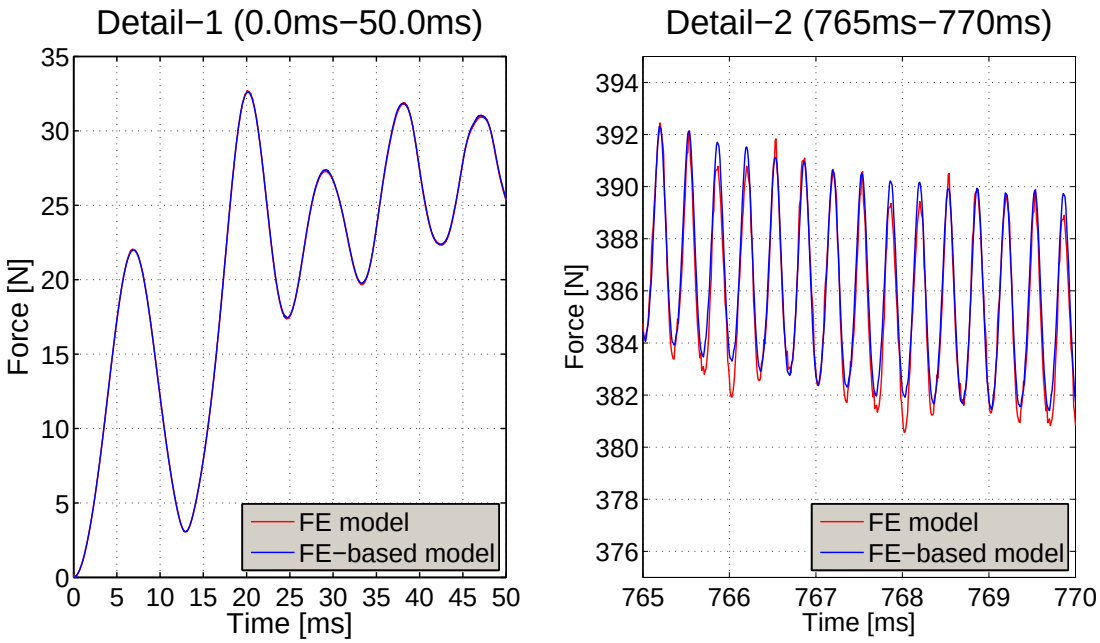

Figure 6.21: Comparison of the machine torque τ between FE model (reference solution) and the presented FE-based machine model.

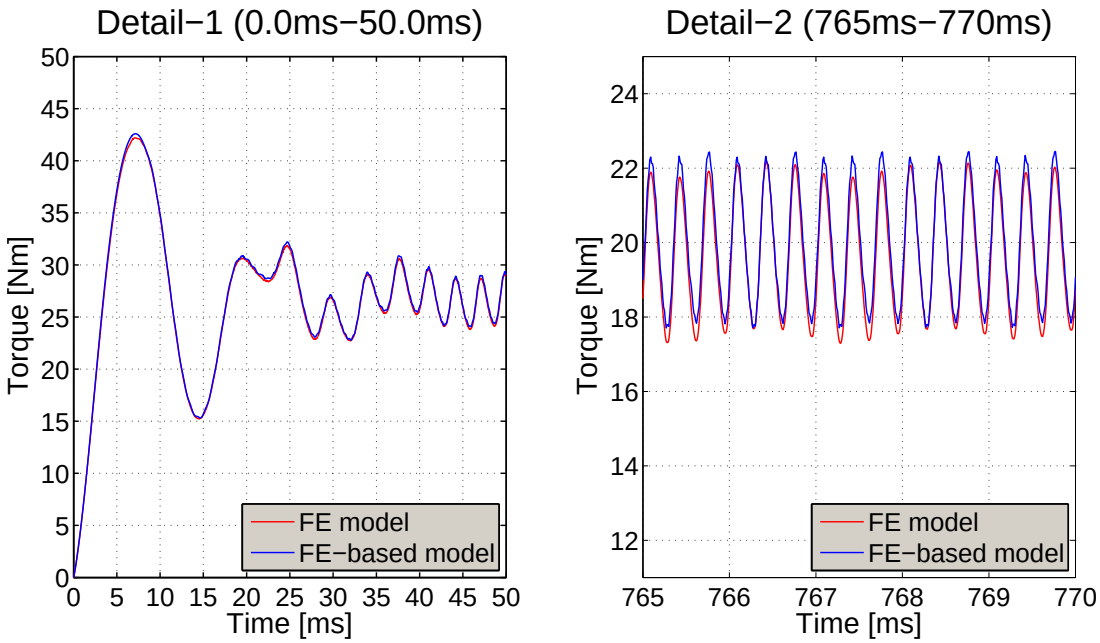

Figure 6.22: Comparison of magnetic drag in radial direction F_r between FE model (reference solution) and the presented FE-based machine model.

7 CONCLUSION AND OUTLOOK

The goal of this work was to find a suitable model approach for electrical machines used in multibody dynamics simulations. For this purpose, a comparison of various machine model approaches has been carried out. It has been shown that the FE-based circuit model approach is best suited for the required field of application. The simulation cost is low, the memory demand is in an acceptable range and the coverage of effects caused by slotting and saturation is high. Furthermore, the workflow for the model parametrization using FE analysis tools is well defined and the required data exchange between machine manufacturer and power train designer hides the complete machine design.

Therefore, the FE-based circuit model approach was investigated in detail and a comprehensive analysis of all model elements and workflow issues was carried out. Thus the FE-based circuit model approach was further developed and extended. This included the development of a very efficient algorithm for the FEM preprocessing as well as implementation of a multi variate cubic spline interpolation library for up to five parameter variables. Furthermore, a multi-slice emulation for considering skewing effects was developed and finally an extended model for considering eccentricity effects was presented.

In the last part of this work the FE-based circuit model approach was applied to various machine types. This included the determination of the state variables and look-up table quantities for all machine types and the derivation of the corresponding machine equations. These models were validated by comparison with magnetostatic FEM simulations with motion. For this validation, the mechanical input as well as the supply voltages for all coil systems was applied as input to the FEM simulation. Thus a direct comparison between the FE-based circuit models and the reference FE model could be achieved. Furthermore, the practicability of all presented models was shown. This included the required memory demand as well well the simulation effort of the preprocessing stage using magnetostatic FEM simulation. The numerical effort during of the FE-based circuit model simulation is very low and thus best suited for transient system simulations.

Concluding, the presented machine model approach is simple, well suited for an application within a multi-body dynamics simulation and easy to use. Thus, all goals defined for this work have been fulfilled.

7.1 Outlook

There is still potential for further improvements and extensions. Within this last section this potential should be coarsely sketched.

All models under investigation use integral quantities of the entire machine as model parameters. This leads to a center-center coupling between rotor and stator. This means

that any torque or magnetic drag acts on the whole machine and that these quantities are uniformly distributed on all coupled nodes on rotor or stator. A possible extension could be to use distributed quantities or density allocations for these quantities leading to center-surface- or surface-surface-coupling. For instance, the magnetic drag acting per tooth can be used leading to a more accurate force transmission into the structural mechanic models of stator and rotor. First investigations on this topic have been already done but are not in the scope of this work. Further activities on this extension are planned for the future.

An open issue is the consideration of eddy current effects in transient FE-based circuit models as presented in this work. The problem here occurs in the model approach itself and fails due to two reasons. The approach requires geometrically well-defined coils for the flux linkage determination with magnetostatic FEM simulations. This criterion is not fulfilled for eddy currents because the current path depends on history and thus varies with time. Furthermore, the number of state variables increases leading to a very high simulation effort for the FEM preprocessing and a huge memory demand for the look-up tables. Nevertheless, a solution for this problem would have high importance because it would allow FE-based circuit models for squirrel cage induction machines.

REFERENCES

[1] P.R. Adby. *Applied Circuit Theory*. Ellis Horwood Ltd, 1980.

[2] N.A. Al-Nuaim and H.A. Toliyat. A novel method for modeling dynamic air-gap eccentricity in synchronous machines based on modified winding function theory. *Energy Conversion, IEEE Transactions on*, 13(2):156–162, June 1998.

[3] P. Alotto, M. Guarnieri, and F. Moro. A mortar cell method for electro-thermal contact problems. *Magnetics, IEEE Transactions on*, 49(2):795–798, February 2013.

[4] ANSYS, Inc. *ANSYSő Academic Research, Release 14.5, Help System, ŞLow- Frequency Electromagnetic Analysis Guide*.

[5] M. Aubertin, T. Henneron, F. Piriou, and J.-C. Mipo. Mortar method using bi-orthogonal nodal functions applied to a-phi formulation. *Magnetics, IEEE Transactions on*, 48(2):491–494, February 2012.

[6] N. Bianchi and S. Bolognani. Magnetic models of saturated interior permanent magnet motors based on finite element analysis. *Industry Applications Conference, 1998. Thirty-Third IAS Annual Meeting. The 1998 IEEE*, 1:27–34, 1998.

[7] A. Binder. *Elektrische Maschinen und Antriebe*. Springer New York Heidelberg Dordrecht London, 2012.

[8] O. Bíró. Edge element formulations of eddy current problems. *Computer Methods in Applied Mechanics and Engineering*, 169:391–405, February 1999.

[9] M. Boesing, T. Schoenen, K.A. Kasper, and R.W. De Doncker. Vibration synthesis for electrical machines based on force response superposition. *Magnetics, IEEE Transactions on*, 46(8):2986–2989, August 2010.

[10] C.D. Boor. *A practical guide to splines*. Springer-Verlag New York, 1978.

[11] C. J. Carpenter. Magnetic equivalent circuits. *Electrical Engineers, Proceedings of the Institution of*, 115(10):1503–1511, October 1968.

[12] C. J. Carpenter. Finite-element network models and their application to eddy-current problems. *Electrical Engineers, Proceedings of the Institution of*, 122(4):455–462, April 1975.

[13] M.V.F. da Luz, P. Dular, N. Sadowski, C. Geuzaine, and J.P.A. Bastos. Analysis of a permanent magnet generator with dual formulations using periodicity conditions and moving band. *Magnetics, IEEE Transactions on*, 38(2):961–964, March 2002.

[14] A. Davoudi and P.L. Chapman. Eddy current modeling with order-reduction in magnetic equivalent circuits. *Power Electronics Specialists Conference, 2007. PESC 2007. IEEE*, pages 2069–2074, June 2007.

[15] A Davoudi, P.L. Chapman, J. Jatskevich, and A Khaligh. Reduced-order modeling of high-fidelity magnetic equivalent circuits. *Power Electronics, IEEE Transactions on*, 24(12):2847–2855, December 2009.

[16] C.A. Desoer and E.S. Kuh. *Basic Circuit Theory*. McGrawHill KogaKusha Ltd, 1969.

[17] R. L. Doeuff and M. E. H. Zaïm. *Rotating Electrical Machines*. John Wiley & Sons, 2010.

[18] D. Dolinar, R. de Weerdt, R. Belmans, and E.M. Freeman. Calculation of two-axis induction motor model parameters using finite elements. *Energy Conversion, IEEE Transactions on*, 12(2):133–142, June 1997.

[19] C. Dufour, J. Belanger, V. Lapointe, and S. Abourida. Real-time simulation on fpga of a permanent magnet synchronous machine drive using a finite-element based model. *Power Electronics, Electrical Drives, Automation and Motion, 2008. SPEEDAM 2008. International Symposium on*, pages 19–25, June 2008.

[20] P. Dziwniel, B. Boualem, F. Piriou, J.-P. Ducreux, and Thomas P. Comparison between two approaches to model induction machines with skewed slots. *IEEE Transactions on Magnetics*, 36(4):1453–1457, July 2000.

[21] H.R. Fudeh and C.M. Ong. Modeling and analysis of induction machines containing space harmonics part i: Modeling and transformation. *Power Apparatus and Systems, IEEE Transactions on*, PAS-102(8):2608–2615, August 1983.

[22] H.R. Fudeh and C.M. Ong. Modeling and analysis of induction machines containing space harmonics part ii: Analysis of asynchronous and synchronous actions. *Power Apparatus and Systems, IEEE Transactions on*, PAS-102(8):2616–2620, August 1983.

[23] H.R. Fudeh and C.M. Ong. Modeling and analysis of induction machines containing space harmonics part iii: Three-phase cage rotor induction machines. *Power Apparatus and Systems, IEEE Transactions on*, PAS-102(8):2621–2628, August 1983.

[24] J. Garcia de Jalon and E. Bayo. *Kinematic and Dynamic Simulation of Multibody Systems*. Mechanical Engineering Series. Springer-Verlag New York, 1994.

[25] J.M. Gojko, D.D. Momir, and O.B. Aleksandar. Skew and linear rise of mmf across slot modelling-winding function approach. *Energy Conversion, IEEE Transactions on*, 14(3):315–320, September 1999.

[26] C. Golovanov, J.-L. Coulomb, Y. Marechal, and G. Meunier. 3d mesh connection techniques applied to movement simulation. *Magnetics, IEEE Transactions on*, 34(5):3359–3362, September 1998.

[27] J.J.C. Gyselinck, L. Vandevelde, and J.A.A. Melkebeek. Multi-slice fe modeling of electrical machines with skewed slots-the skew discretization error. *Magnetics, IEEE Transactions on*, 37(5):3233–3237, September 2001.

[28] P. Handgruber. Vorausberechnung der oberschwingungsemissionen von windkraftanlagen mit doppelt gespeister asynchronmaschine. Master's thesis, Technische Universität Graz, 2010.

[29] H. Henke. *Elektromagnetische Felder - Theorie und Anwendung*. Springer Berlin Heidelberg, 4 edition, 2011.

[30] N.J. Higham. *Accuracy and Stability of Numerical Algorithms*. Society for Industrial and Applied Mathematics, 2002.

[31] T. Ilamparithi and S. Nandi. Comparison of results for eccentric cage induction motor using finite element method and modified winding function approach. *Power Electronics, Drives and Energy Systems (PEDES), 2010 Power India, 2010 Joint International Conference on*, December 2010.

[32] J.D. Jackson. *Classical Electrodynamics*. John Wiley & Sons, 1962.

[33] J.M. Jin. *The Finite Element Method in Electromagnetics*. John Wiley & Sons, Inc. New York, 2 edition, 2002.

[34] J.P. Johnson, A.V. Rajarathnam, H.A. Toliyat, S. Gopalakrishnan, and B. Fahimi. Torque optimization for a srm using winding function theory with a gap-dividing surface. *Industry Applications Conference, 1996. Thirty-First IAS Annual Meeting, IAS '96., Conference Record of the 1996 IEEE*, 2:753–760, October 1996.

[35] G.M. Joksimovic, M.D. Durovic, J. Penman, and N. Arthur. Dynamic simulation of dynamic eccentricity in induction machines-winding function approach. *Energy Conversion, IEEE Transactions on*, 15(2):143–158, June 2000.

[36] S. Kallio, J. Karttunen, M. Andriollo, P. Peltoniemi, and P. Silventoinen. Finite element based phase-variable model in the analysis of double-star permanent magnet synchronous machines. *Power Electronics, Electrical Drives, Automation and Motion (SPEEDAM), 2012 International Symposium on*, pages 1462–1467, 2012.

[37] H.M. Kelk, A Eghbali, and H.A Toliyat. Modeling and analysis of cage induction motors under rotor misalignment and air gap eccentricity. *Industry Applications Conference, 2005. Fourtieth IAS Annual Meeting. Conference Record of the 2005*, 2:1324–1328, October 2005.

[38] B. Klein. *FEM, Grundlagen und Anwendungen der Finite-Element-Methode im Maschinen- und Fahrzeugbau*. Friedr. Vieweg & Sohn Verlag, 7 edition, 2007.

[39] H. Klingbeil. *Elektromagnetische Feldtheorie*. B. G. Teubner Stuttgart, 2003.

[40] P. Koutsovasilis. *Model Order Reduction in Structural Mechanics: Coupling the Rigid and Elastic Multi Body Dynamics*. PhD thesis, Technische Universität Dresden, 2009.

[41] E. Kreyszig. *Advanced Engineering Mathematics*. John Wiley and Sons Inc., New York, 8 edition, 1999.

[42] R. Lach. *Magnetische Geräuschemission umrichtergespeister Käfigläufer- Asynchronmaschinen*. PhD thesis, Universität Dortmund, 2005.

[43] F. Lekien and J. Marsden. Tricubic interpolation in three dimensions. *INTERNATIONAL JOURNAL FOR NUMERICAL METHODS IN ENGINEERING*, 63(3):455–471, March 2005.

[44] Z. Liu, O.A. Mohammed, and S. Liu. An improved physics-based phase variable model of pm synchronous machines obtained through field computation. *Computation in Electromagnetics, 2008. CEM 2008. 2008 IET 7th International Conference on*, pages 166–167, April 2008.

[45] D.A. Lowther and P.P. Silverster. *Computer-Aided Design in Magnetics*. Springer-Verlag New York, 1986.

[46] X. Luo, Y. Liao, Hamid T., A. El-Antably, and T.A. Lipo. Multiple coupled circuit modeling of induction machines. *Industry Applications Society Annual Meeting, 1993., Conference Record of the 1993 IEEE*, 1:203–210, October 1993.

[47] H. Meshgin-Kelk, J. Milimonfared, and H.A Toliyat. A comprehensive method for the calculation of inductance coefficients of cage induction machines. *Energy Conversion, IEEE Transactions on*, 18(2):187–193, June 2003.

[48] O.A. Mohammed, S. Ganu, N. Abed, Z. Liu, and S. Liu. High frequency modeling of pm synchronous machine for use in integrated motor drive. *Electric Ship Technologies Symposium, 2007. ESTS '07. IEEE*, pages 245–249, May 2007.

[49] O.A. Mohammed, S. Liu, and Z. Liu. Phase-variable model of pm synchronous machines for integrated motor drives. *Science, Measurement and Technology, IEE Proceedings*, 151(6):423–429, November 2004.

[50] O.A. Mohammed, S. Liu, and Z. Liu. A phase variable pm machine model for integrated motor drive systems. *Power Electronics Specialists Conference, 2004. PESC 04. 2004 IEEE 35th Annual*, 6:4825–4831, June 2004.

[51] O.A. Mohammed, S. Liu, and Z. Liu. Physical modeling of electric machines for motor drive system simulation. *Power Systems Conference and Exposition, 2004. IEEE PES*, 2:781–786, October 2004.

[52] O.A. Mohammed, S. Liu, and Z Liu. A phase variable model of brushless dc motors based on finite element analysis and its coupling with external circuits. *Magnetics, IEEE Transactions on*, 41(5):1576–1579, May 2005.

[53] O.A. Mohammed, S. Liu, and Z. Liu. Physical modeling of pm synchronous motors for integrated coupling with machine drives. *Magnetics, IEEE Transactions on*, 41(5):1628–1631, May 2005.

[54] O.A. Mohammed, S. Liu, and Z. Liu. An fe-based physical phase variable model for pm synchronous machines including dynamic core losses. *Electromagnetic Field Computation, 2006 12th Biennial IEEE Conference on*, page 137, 2006.

[55] O.A. Mohammed, S. Liu, and Z. Liu. Fe-based physical phase variable models of electric machines and transformers for dynamic simulations. *Power Engineering Society General Meeting, 2006. IEEE*, page 7, 2006.

[56] O.A. Mohammed, S. Liu, and Z. Liu. Fe-based physical phase variable model of pm synchronous machines under stator winding short circuit faults. *Science, Measurement & Technology, IET*, 1(1):12–16, January 2007.

[57] O.A. Mohammed, S. Liu, Z. Liu, and N. Abed. Physical phase variable models of electrical equipments and their applications in integrated drive simulation for shipboard power system. *Electric Ship Technologies Symposium, 2005 IEEE*, pages 163–170, July 2005.

[58] O.A. Mohammed, Z. Liu, and S. Liu. A novel sensorless control strategy of doubly fed induction motor and its examination with the physical modeling of machines. *Magnetics, IEEE Transactions on*, 41(5):1852–1855, May 2005.

[59] O.A. Mohammed, Z. Liu, S. Liu, and N.Y. Abed. Finite-element-based nonlinear physical model of iron-core transformers for dynamic simulations. *Magnetics, IEEE Transactions on*, 42(4):1027–1030, April 2006.

[60] M. Mohr, O. Bíró, and F. Diwoky. Consideration of rotor eccentricity effects in a multi body dynamics simulation using a finite element based circuit model approach. In *Electrical Machines (ICEM), 2014 XXIth International Conference on*, 2014.

[61] M. Mohr, O. Bíró, A. Stermecki, and F. Diwoky. An improved physical phase variable model for permanent magnet machines. In *Electrical Machines (ICEM), 2012 XXth International Conference on*, pages 53–58, Marseille, 2012. IEEE.

[62] M. Mohr, O. Bíró, A. Stermecki, and F. Diwoky. An improved physical phase variable model for wound rotor induction machines. In *Biennial IEEE Conference on Electromagnetic Field Computation*, page 274, Oita, 2012.

[63] M. Mohr, O. Bíró, A. Stermecki, and F. Diwoky. An extended finite element based model approach for permanent magnet synchronous machines including rotor eccentricity. In *Industrial Electronics Society, IECON 2013 - 39th Annual Conference of the IEEE*, pages 2596–2601, Vienna, 2013. IEEE.

[64] M. Mohr, O. Bíró, A. Stermecki, and F. Diwoky. Parameter identification of a finite element based model of wound rotor induction machines. *Compel*, 32(5):1665–1678, 2013.

[65] M. Mohr, O. Bíró, A. Stermecki, and F. Diwoky. A finite element based circuit model approach for skewed electrical machines. *IEEE transactions on magnetics*, 50(2):837–840, 2014.

[66] J.C. Moreira and T.A. Lipo. Modeling of saturated ac machines including air gap flux harmonic components. *Industry Applications, IEEE Transactions on*, 28(2):343–349, March 1992.

[67] G. Müller and B. Ponick. *Grundlagen elektrischer Maschinen*. Number 1 in Elektrische Maschinen. Wiley-VCH, Berlin, 9 edition, November 2005.

[68] G. Müller and B. Ponick. *Theorie elektrischer Maschinen*. Number 3 in Elektrische Maschinen. Wiley-VCH, Berlin, 6 edition, January 2009.

[69] G. Müller, K. Vogt, and B. Ponick. *Berechnung elektrischer Maschinen*. Number 2 in Elektrische Maschinen. Wiley-VCH, Berlin, 6 edition, Oktober 2007.

[70] K. Oberretl. Die oberfeldtheorie des käfigmotors unter berücksichtigung der durch die ankerrückwirkung verursachten statoroberströme und der parallelen wicklungszweige. *Archiv für Elektrotechnik*, 49(6):343–364, November 1965.

[71] K. Oberretl. Magnetic fields, eddy currents, and losses, taking the variable permeability into account. *Power Apparatus and Systems, IEEE Transactions on*, PAS-88(11):1646–1657, November 1969.

[72] K. Oberretl. Field-harmonic theory of slip-ring motor taking multiple armature reaction into account. *Electrical Engineers, Proceedings of the Institution of*, 117(8):1667–1674, August 1970.

[73] K. Oberretl. Losses, torques and magnetic noise in induction motors with static converter supply, taking multiple armature reaction and slot openings into account. *Electric Power Applications, IET*, 1(4):517–531, July 2007.

[74] V. Ostović. A method for evaluation of transient and steady state performance in saturated squirrel cage induction machines. *Energy Conversion, IEEE Transactions on*, EC-1(3):190–197, September 1986.

[75] V. Ostović. *Dynamics of Saturated Electric Machines*. Springer-Verlag New York Inc., 1989.

[76] V. Ostović, J.M. Miller, V.K. Garg, R.D. Schultz, and S.H. Swales. A magnetic-equivalent-circuit-based performance computation of a lundell alternator. *Industry Applications, IEEE Transactions on*, 35(4):825–830, July/August 1999.

[77] F. Piriou and A. Razek. A model for coupled magnetic-electric circuits in electric machines with skewed slots. *IEEE Transactions on Magnetics*, 26(2):1096–1100, March 1990.

[78] N.Q. Quang and J.-A. Dittrich. *Praxis der feldorientierten Drehstromantriebsregelungen*. Expert-Verlag GmbH, January 1999.

[79] F. Rapetti, F. Bouillault, L. Santandrea, A. Buffa, Y. Maday, and A. Razek. Calculation of eddy currents with edge elements on non-matching grids in moving structures. *Magnetics, IEEE Transactions on*, 36(4):1351–1355, July 2000.

[80] P. Rasilo, M.-A. Lemesle, A. Belahcen, A. Arkkio, and M. Hinkkanen. Comparison of finite-element-based state-space models for pm synchronous machines. *Energy Conversion, IEEE Transactions on*, 29(2):535–543, June 2014.

[81] J. Reddy. *An Introduction to the Finite Element Method*. Engineering Series. McGraw-Hill Science/Engineering/Math, 3 edition, 2005.

[82] A. Sarikhani and O.A. Mohammed. Development of transient fe-physics-based model of induction for real time integrated drive simulations. *Electric Machines & Drives Conference (IEMDC), 2011 IEEE International*, pages 687–692, May 2011.

[83] A. Sarikhani and O.A. Mohammed. Multiobjective design optimization of coupled pm synchronous motor-drive using physics-based modeling approach. *Magnetics, IEEE Transactions on*, 47(5):1266–1269, May 2011.

[84] H.O. Seinsch. *Oberfelderscheinungen in Drehfeldmaschinen - Grundlagen zur analytischen Berechnung*. B. G. Teubner Stuttgart, 1992.

[85] A.A. Shabana. *Dynamics of Multibody Systems*. Cambridge University Press, 3 edition, 2005.

[86] A. Stermecki, O. Bíró, K. Preis, S. Rainer, and G. Ofner. Numerical analysis of steady-state operation of three-phase induction machines by an approximate frequency domain technique. *e & i Elektrotechnik und Informationstechnik*, 128(3):81–85, 2011.

[87] S.D. Sudhoff, B.T. Kuhn, K.A Corzine, and B.T. Branecky. Magnetic equivalent circuit modeling of induction motors. *Energy Conversion, IEEE Transactions on*, 22(2):259–270, June 2007.

[88] A.R. Tariq, C.E. Nino-Baron, and E.G. Strangas. Iron and magnet losses and torque calculation of interior permanent magnet synchronous machines using magnetic equivalent circuit. *Magnetics, IEEE Transactions on*, 46(12):4073–4080, December 2010.

[89] P. Tobin. *PSpice for Circuit Theory and Electronic Devices*. Morgan and Claypool Publishers, 1 edition, April 2007.

[90] S. N. Vukosavic. *Electrical Machines*. Power Electronics and Power Systems. Springer New York Heidelberg Dordrecht London, 2013.

[91] B. Weilharter, O. Biro, S. Rainer, and A. Stermecki. Computation of rotating force waves in skewed induction machines using multi-slice models. *Magnetics, IEEE Transactions on*, 47(5):1046–1049, May 2011.

[92] S. Williamson, T.J. Flack, and A.F. Volschenk. Representation of skew in time-stepped two-dimensional finite-element models of electrical machines. *Industry Applications, IEEE Transactions on*, 31(5):1009–1015, September 1995.

[93] C. Woernle. *Mehrkörpersysteme - Eine Einführung in die Kinematik und Dynamik von Systemen starrer Körper*. Springer Berlin Heidelberg, 2011.

[94] Mengqi Zhang, A. MacDonald, King-Jet Tseng, and G.M. Burt. Magnetic equivalent circuit modeling for interior permanent magnet synchronous machine under eccentricity fault. *Power Engineering Conference (UPEC), 2013 48th International Universities*, pages 1–6, September 2013.

[95] P. Zhou, D. Lin, G. Wimmer, N. Lambert, and Z.J. Cendes. Determination of d-q axis parameters of interior permanent magnet machine. *Magnetics, IEEE Transactions on*, 46(8):3125–3128, August 2010.

[96] L. Zhu, S.Z. Jiang, Z.Q. Zhu, and C.C. Chan. Analytical methods for minimizing cogging torque in permanent-magnet machines. *Magnetics, IEEE Transactions on*, 45(4):2023–2031, April 2009.

[97] Z.Q. Zhu and D. Howe. Instantaneous magnetic field distribution in brushless permanent magnet dc motors. ii. armature-reaction field. *Magnetics, IEEE Transactions on*, 29(1):136–142, January 1993.

[98] Z.Q. Zhu and D. Howe. Instantaneous magnetic field distribution in brushless permanent magnet dc motors. iii. effect of stator slotting. *Magnetics, IEEE Transactions on*, 29(1):143–151, January 1993.

[99] Z.Q. Zhu and D. Howe. Instantaneous magnetic field distribution in permanent magnet brushless dc motors. iv. magnetic field on load. *Magnetics, IEEE Transactions on*, 29(1):152–158, January 1993.

[100] Z.Q. Zhu, D. Howe, E. Bolte, and B. Ackermann. Instantaneous magnetic field distribution in brushless permanent magnet dc motors. i. open-circuit field. *Magnetics, IEEE Transactions on*, 29(1):124–135, January 1993.

[101] Z.Q. Zhu, K. Wang, and G. Ombach. Optimal magnet shaping with third order harmonic for maximum torque in brushless ac machines. *Power Electronics, Machines and Drives (PEMD 2012), 6th IET International Conference on*, March 2012.